# **Materials for High Temperature Electronic Packaging**

by

Jinzi Cui

A dissertation submitted to the Graduate Faculty of
Auburn University
in partial fulfillment of the
requirements for the Degree of
Doctor of Philosophy

Auburn, Alabama
December 10, 2016

Keyword: encapsulation, Ni finishing, die attach,
high temperature packaging

Copyright 2016 by Jinzi Cui

Approved by

R. Wayne Johnson, Chair, Visit Professor of Electrical & Computer Engineering
Michael C. Hamilton, Co-Chair, Associate Professor of Electrical & Computer Engineering
Robert N. Dean, Professor of Electrical & Computer Engineering
Dong-Joo Kim, Associate Professor of Materials Engineering

Abstract

Normally, the operating temperature of consumer electronic devices is from 0°C to 70°C. However, some industries are interested in electronics that can operate in extreme environments. The working environment temperature of power devices in hybrid electric vehicles is between 150°C and 200°C, while instruments for well drilling and exploration in the gas and oil industry demand more than 150°C operating temperature. As engineers seek to extend the benefits of electronics to more applications, the demand for high-temperature electronics is increasing.

Electronic coatings like conformal coating, potting and encapsulation are used widely to protect electronic modules. Acrylic resin, epoxy, silicones, and polyurethane are used as the coating materials. However, few of these materials can withstand high temperatures above 300°C. Parylene HT is a potential candidate for high temperature (short term up to 450°C) encapsulation. It can provide uniform, pin-hole free conformal coatings, which protect the circuit from moisture and other contamination. In this work, a test pattern was designed to evaluate Parylene HT as an insulation coating material for electronic devices during a 300°C storage test. In addition, some other coating materials that were advertised for use at 300°C were investigated.

Nickel/gold finishing is quite commonly used as a solderable and protective surface finishing for direct bonded copper (DBC) substrates used in high-temperature power applications. Many forms of Ni are available based on the plating process (electroless or electrolytic) and the plating chemistry ( phosphorus, boron, or cobalt). During soldering and high temperature aging, the formation of Ni intermetallics and voids occur that may impact reliability. Reactions between

different Ni plating and BiAgX® (Indium Corp.) and AuGe were investigated. The decrease in shear strength after formation of Ni-Ge and $NiBi_3$ intermetallics were specifically studied. The growth kinetics and activation energy of Ni-Ge intermetallic formation were calculated.

Acknowledgments

First of all, I would like to express my sincere gratitude to my advisor Professor Wayne Johnson for his continuous guiding and support of my Ph.D. study and research. His great patience and immense professional knowledge helped me in research and writing of this dissertation. I am also thankful to my co-advisor, Dr. Michael Hamilton who gave me continued help after Dr. Johnson left Auburn University. He supported not only my research but also provided great lab maintenance. I would like to thank Dr. Robert Dean, Dr. Dong-Joo Kim and Dr. Bart Prorok on my committee for their valuable time and suggestions.

I would also like to thank Dr. Charles D. Ellis, Michael J. Palmer and William Baugh for their great support in the laboratory through all these years. And my colleagues and friends Kun Fang, Zhenzhen Shen, Fang Yu and Zhangming Zhou for their insightful comments and continual assistance.

At last but not least, I want to thank my father Zheng Cui and my mother Hongxia Jin. Their persistent love and support encourage me to overcome the difficulties in my life.

Table of Contents

Abstract ........ ii

Acknowledgments ........ iv

Table of Contents ........ v

List of Tables ........ ix

List of Figures ........ xi

CHAPTER 1 INTRODUCTION ........ 1

1.1 High Temperature Electronics (HTE) ........ 1

1.2 Applications of High Temperature Electronics ........ 1

1.3 High Temperature Electronic Packaging ........ 4

1.3.1 SiC Devices ........ 6

1.3.2 Die Attach Solder Material ........ 9

1.3.3 Substrate Materials ........ 11

1.3.4 Surface Finishing ........ 12

1.3.4.1 Electroless & Electrolytic Nickel Plating ........ 14

1.3.5 Electronic Coating Technology ........ 16

1.4 Research Outline ........ 19

CHAPTER 2 HIGH TEMPERATURE ELECTRONIC COATING ........ 21

2.1 Introduction ........ 21

2.2 Test Vehicle ........ 24

2.2.1 Substrate ........ 24

2.2.2 Encapsulation....25
2.3 Breakdown Voltage Without Coating....26
2.4 Aging Test....28
2.5 Parylene HT Adhesion Test....29
2.6 FTIR Analysis for Parylene HT....32
2.7 AFM Analysis for Parylene HT....34
2.8 Summary....35
CHAPTER 3 BIAGX ON NI PLATING....36
3.1 Introduction of BiAgX....36
3.2 Potential Intermetallic Formation....37
3.3 Assembly....40
3.3.1 Die....40
3.3.2 Substrate....40
3.3.3 Finishes....40
3.3.4 Assembly Process....41
3.4 Initial Shear Data....41
3.4.1 Cross Section & Fracture Analysis....42
3.5 Aging Test....47
3.5.1 Cross Section and Fracture Analysis....49
3.5.1.1 Electroless Ni:P....52
3.5.1.2 Electrolytic Ni....56
3.5.1.3 Electrolytic Ni:P....60
3.5.1.4 Electrolytic Ni:Co....62

3.6 Thermal Cycling........................................................................................................ 65

3.6.1 Cross Section & Fracture Analysis...................................................................... 67

3.7 Summary........................................................................................................................ 76

CHAPTER 4 DIE ATTACH USING AUGE SOLDER PREFORM..........................................77

4.1 Introduction.....................................................................................................................77

4.2 Literature Review.............................................................................................................78

4.3 Potential Intermetallic Compounds...................................................................................79

4.4 Assembly.........................................................................................................................81

4.4.1 Die.............................................................................................................................81

4.4.2 Substrate......................................................................................................................82

4.4.3 Process........................................................................................................................ 82

4.5 Initial Shear Data.............................................................................................................. 84

4.5.1 Cross Section & Fracture Analysis...................................................................... 84

4.6 Aging Study........................................................................................................................ 92

4.6.1 Cross Section.............................................................................................................. 96

4.7 Thermal Cycling................................................................................................................ 106

4.7.1 Aging & Thermal Cycle Test.................................................................................107

4.7.2 Cross Section and Fracture Analysis.................................................................... 108

4.8 Growth Kinetic of Ni-Ge IMC..........................................................................................111

4.9 Nanoindentation................................................................................................................114

4.9.1 Results.........................................................................................................................117

4.10 Summary..........................................................................................................................123

CHAPTER 5 CONCLUSION AND FUTURE WORK RECOMMENDATION.......................125

5.1 High Temperature Electronic Coating........................................................................ 125

5.2 BiAgX on Nickel Plating.......................................................................................... 125

5.3 AuGe on Nickel Plating............................................................................................ 127

5.4 Future Work Recommendation.................................................................................127

REFERENCE.......................................................................................................................129

List of Tables

Table 1.1 Applications Area and Characteristics for High Temperature Electronics [8][9]........... 4

Table 1.2 Physical Characteristics of Si and Major WBG Semiconductors [12]........................... 6

Table 1.3 Package Substrate Material Parameters at 300K [24]................................................. 12

Table 1.4 Surface Finishing Types [26]..........................................................................13

Table 1.5 Electrical and Thermal Properties of Ag, Au, Ni and Pd [27].....................................13

Table 2.1 Electric Properties of Parylenes [48]............................................................... 22

Table 2.2  Thermal Properties of Parylenes [48]............................................................. 22

Table 2.3  Properties of Duraseal 1531 [51]................................................................... 23

Table 2.4 Initial Breakdown Data Without Coating.......................................................... 27

Table 2.5 Parylene HT Roughness.................................................................................34

Table 3.1 Nickel Composition as Provided by the Plating Suppliers.......................................... 40

Table 3.2 BiAgX Initial Average Shear Strength............................................................. 41

Table 3.3 Thermal Cycle Data for 5 mm × 5 mm SiC Die Attached to DBC Substrates in kg/mm$^2$

..........................................................................................................................66

Table 4.1 Physical Properties of AuGe12 [65]................................................................. 77

Table 4.2 Nickel Composition as Provided by the Plating Suppliers.......................................... 82

Table 4.3 AuGe Initial Average Shear Strength............................................................... 84

Table 4.4 Electrolytic Ni:P Shear Result of 3000 hours Aging at 300$^o$C  Plus 500 cycles 300$^o$C to -55$^o$C Compare with Electrolytic Ni:P Shear Result of 3000 hours at 300$^o$C............................ 108

Table 4.5 Ni-Ge IMC Growth Rate Constant................................................................. 112

Table 4.6 Ni Germanide Activation Energy Comparison............................................................114

Table 4.7 Average Hardness and Elastic Modulus of Cu in the Electroless Ni:P Sample.......... 117

Table 4.8 Average Hardness and Elastic Modulus of Ni:P Layer............................................... 119

Table 4.9 Average Hardness and Elastic Modulus of Ni-Ge IMC Layer...................................121

Table 4.10 Comparison of the Data Obtained in the Present Study............................................ 123

List of Figures

Figure 1.1 Typical Electronics Packaging Structure [11]............................................................5

Figure 1.2 Semiconductor Intrinsic Carrier Concentration (n) versus Temperature for Silicon, 6H-SiC, and 2H-GaN [13]............................................................................................................7

Figure 1.3 Melting Ranges for Typical High Temperature Solders and Applications [16]........... 9

Figure 1.4 Note the Uniformity of the Electroless Coating as Compared with that of Electrolytic Ni Deposit [35]........................................................................................................................ 16

Figure 1.5 Conformal Coating [44]........................................................................................ 18

Figure 1.6 Parylene Coating Process [43]...............................................................................18

Figure 1.7 Potting and Encapsulation [46]............................................................................. 19

Figure 2.1 Chemical Structure of Parylenes [47].....................................................................21

Figure 2.2 High Voltage Breakdown Test Vehicle...................................................................25

Figure 2.3 Apply Duraseal 1531 on Substrate.........................................................................26

Figure 2.4 Probe Station....................................................................................................... 26

Figure 2.5 High Voltage Breakdown Surface...........................................................................27

Figure 2.6 Leakage Current versus Aging Time at 300°C of Parylene HT (a) 5 mil (b) 10 mil... 28

Figure 2.7 Leakage Current Versus Aging Time at 300°C of Duraseal 1531 (a) 5 mil (b) 10 mil.... .......................................................................................................................................29

Figure 2.8 Parylene HT Peel Off after 2000 hours Aging at 300°C......................................... 29

Figure 2.9 Mask of Parylene HT on Electroplated Gold Test Vehicle......................................30

Figure 2.10 Parylene HT Adhesion Test Sample....31
Figure 2.11 Illustration of Pull Testing....31
Figure 2.12 Pull Strength of Parylene HT on Electroplated Gold and AlN as a Function of Aging hour at 300$^{o}$C (a) Electroplated Gold (b) AlN....32
Figure 2.13 FTIR Result of Parylene HT by SCS [48]....33
Figure 2.14 FTIR Result of Parylene HT....33
Figure 2.15 AFM 3-D Topography of Parylene HT on As-built Sample....34
Figure 2.16 AFM 3-D Topography of Parylene HT on 1000 hours Aged Sample.... 35
Figure 3.1 Ag-Bi Phase Diagram [57].... 37
Figure 3.2 Bi-Cu Phase Diagram [59].... 38
Figure 3.3 Bi-Sn Phase Diagram [60]....38
Figure 3.4 Bi-Ni Phase Diagram [63].... 39
Figure 3.5 Ni-Sn Phase Diagram [64]....39
Figure 3.6 Reflow Profile.... 41
Figure 3.7 As-built BiAgX on Electrolytic Ni:P Cross Section and Elemental Analysis (at.%).. 42
Figure 3.8 As-built BiAgX on Electrolytic Ni Cross Section and Elemental Anaylsis (at.%)......43
Figure 3.9 As-built BiAgX on Electrolytic Ni:P Cross Section and Elemental Analysis (at.%).. 44
Figure 3.10 As-built BiAgX on Electroless Ni:P Cross Section and Elemental Analysis (at.%)..44
Figure 3.11 As-built BiAgX on Electrolytic Ni:Co Cross Section and Elemental Analysis (at.%).. ....45
Figure 3.12. As-built BiAgX on Electrolytic Ni:P Fracture Surfaces after Die Shear (at.%)....... 46
Figure 3.13 Die Shear Data for BiAgX as a Function of Storage Time at 200$^{o}$C. (a) Electroless Ni:P, (b) Electroplated Ni, (c) Electroplated Ni:P, and (d) Electrolytic Ni:Co.... 49

Figure 3.14 Cross Section of BiAgX on Electrolytic Ni Aging after 16 hours at 200$^{o}$C............. 50

Figure 3.15 Cross Section and Element Analysis of the BiAgX Die Attach on Electrolytic Ni after 16 hours at 200$^{o}$C.......................................................................................................... 50

Figure 3.16 Cross Section of BiAgX on Electrolytic Ni Aging after 144 hours at 200$^{o}$C........... 51

Figure 3.17 Cross Section of BiAgX on Electrolytic Ni Aging after 500 hours at 200$^{o}$C........... 52

Figure 3.18 Cross Section of the BiAgX Die Attach on Electroless Ni:P after 500 hours at 200$^{o}$C ........................................................................................................................................53

Figure 3.19 Cross Section of the BiAgX Die Attach on Electroless Ni:P after 3000 hours at 200$^{o}$C..................................................................................................................................53

Figure 3.20 BiAgX on Electroless Ni:P Cross Section and Elemental Analysis after 3000 hours at 200$^{o}$C (at.%)......................................................................................................................54

Figure 3.21 Die Shear Fracture Surfaces of BiAgX on Electroless Ni:P Sample Aged for 3000 hours at 200$^{o}$C (at.%)...............................................................................................................55

Figure 3.22 Cross Section of BiAgX on Electrolytic Ni 3000 hours Aging at 200$^{o}$C (at.%)........56

Figure 3.23 Cross Section of BiAgX on Electrolytic Ni 3000 hours Aging at 200$^{o}$C in High Magnification Close to the Die Side (at.%)........................................................................ 57

Figure 3.24 Cross Section of BiAgX on Electrolytic Ni 3000 hours Aging at 200$^{o}$C in High Magnification Close to the Die Side (at.%)........................................................................ 58

Figure 3.25 Die Shear Fracture Surfaces of BiAgX on Electrolytic Ni Sample Aged for 3000 hours at 200$^{o}$C (at.%)............................................................................................................. 59

Figure 3.26 Cross Section of the BiAgX Die Attach on Electrolytic Ni:P after 3000 hours at 200$^{o}$C..................................................................................................................................60

Figure 3.27 Die Shear Fracture Surfaces of BiAgX on Electrolytic Ni:P Sample Aged for 3000 hours at 200°C (at.%)........61
Figure 3.28 Cross Section of the BiAgX Die Attach on Electrolytic Ni:Co after 500 hours at 200°C (at.%)........62
Figure 3.29 Cross Section of the BiAgX Die Attach on Electrolytic Ni:Co after 500 hours at 200°C (at.%)........63
Figure 3.30 Die Shear Fracture Surfaces of BiAgX on Electrolytic Ni:Co Sample Aged for 500 hours at 200°C (at.%)........64
Figure 3.31 Thermal Cycle Profile........65
Figure 3.32 Cross Section of the BiAgX Die Attach on Electroless Ni:P after 1500 Thermal Cycles........67
Figure 3.33 Die Shear Fracture Surfaces of BiAgX on Electroless Ni:P Sample after 1500 Thermal Cycles (at.%)........68
Figure 3.34 Cross Section of the BiAgX Die Attach on Electrolytic Ni:P after 1500 Thermal Cycles........69
Figure 3.35 Die Shear Fracture Surfaces of BiAgX on Electrolytic Ni:P Sample after 1500 Thermal Cycles (at.%)........70
Figure 3.36 Cross Section of the BiAgX Die Attach on Electrolytic Ni after 1500 Thermal Cycles........71
Figure 3.37 Die Shear Fracture Surfaces of BiAgX on Electrolytic Ni Sample after 1500 Thermal Cycles (at.%)........72
Figure 3.38 Die Shear Fracture Surfaces at Center of BiAgX on Electrolytic Ni Sample after 1500 Thermal Cycles (at.%)........73

Figure 3.39 Cross Section of the BiAgX Die Attach on Electrolytic Ni:Co after 1000 Thermal Cycles....74

Figure 3.40 Die Shear Fracture Surfaces of BiAgX on Electrolytic Ni:Co Sample after 1000 Thermal Cycles (at.%).... 75

Figure 4.1 Au-Ge Phase Diagram [66].... 78

Figure 4.2 Ni-Cu Phase diagram [72]....80

Figure 4.3 Ni-Au Phase diagram [73]....80

Figure 4.4 Ni-Ge Phase diagram [74]....81

Figure 4.5 AuGe Die Attach Configuration....83

Figure 4.6 AuGe Assembly Profile....83

Figure 4.7 As-built AuGe on Electrolytic Ni Cross Section....84

Figure 4.8 As-built AuGe on Electrolytic Ni Cross Section and Elemental Analysis (at.%)....85

Figure 4.9 High Magnification Image of $Ni_5Ge_3$-to-Ni Interface Showing Voiding....86

Figure 4.10 Die Shear Fracture Surfaces of As-built AuGe on Electrolytic Ni Sample (at.%)....87

Figure 4.11 As-built AuGe on Electroless Ni:B Cross Section and Elemental Analysis (at.%)... 88

Figure 4.12 Die Shear Fracture Surfaces of As-built AuGe on Electroless Ni:B Sample (at.%).. 89

Figure 4.13 As-built AuGe on Electroless Ni:P Cross Section and Elemental Analysis at Ni Interface (at.%).... 90

Figure 4.14 Die Shear Fracture Surfaces of As-built AuGe on Electroless Ni:P Sample (at.%).. 91

Figure 4.15 Die Shear Strength of AuGe as a Function of Storage Time at 300°C on....93

(a) Electroless Ni:P (b) Electrolytic Ni:P....93

Figure 4.16 Die Shear Strength of AuGe as a Function of Storage Time at 325°C on....95

(a) Electroless Ni:P (b) Electrolytic Ni:P....95

Figure 4.17 Electroless Ni:P 3000hr 300$^{o}$C Aging and Elemental Analysis (at.%).................... 97

Figure 4.18 Cross Section of the AuGe Die Attach on Electroless Ni:P after 1000 hours at 300$^{o}$C (at.%)........................................................................................................................98

Figure 4.19 Die Shear Fracture Surfaces of AuGe on Electroless Ni:P Sample Aged for 3000 hours at 300$^{o}$C (at.%)....................................................................................................99

Figure 4.20 Electrolytic Ni:P after 3000 hours of 300$^{o}$C Aging and Elemental Analysis (at.%) ........................................................................................................................100

Figure 4.21 Die Shear Fracture Surfaces of AuGe on Electrolytic Ni:P Sample Aged for 3000 hours at 300$^{o}$C(at.%)..................................................................................................... 101

Figure 4.22 Electroless Ni:P after 3000 hours of 325$^{o}$C Aging and Elemental Analysis (at.%) ........................................................................................................................102

Figure 4.23 Die Shear Fracture Surfaces of AuGe on Electroless Ni:P Sample Aged for 3000 hours at 325$^{o}$C(at.%)..................................................................................................... 103

Figure 4.24 Electrolytic Ni:P after 3000 hours of 325$^{o}$C Aging and Elemental Analysis (at.%) ........................................................................................................................104

Figure 4.25 Die Shear Fracture Surfaces of AuGe on Electrolytic Ni:P Sample Aged for 3000 hours at 325$^{o}$C(at.%)..................................................................................................... 105

Figure 4.26 Thermal Cycling Profile.......................................................................... 106

Figure 4.27 (a) DBC Substrate As-built, (b) after 500 Cycles, (c) after 1000 Cycles................ 107

Figure 4.28 Electrolytic Ni:P Cross Section after 3000 hours of 300$^{o}$C Aging Plus 500 cycles from 300$^{o}$C to -55$^{o}$C and Elemental Analysis (at.%)................................................................109

Figure 4.29 Die Shear Fracture Surfaces of AuGe on Electrolytic Ni:P Sample Aged for 3000 hours at 300$^{o}$C Plus 500 cycles 300$^{o}$C to -55$^{o}$C (at.%)..............................................................110

Figure 4.30 Thickness of the Ni-Ge IMC Layer Formed with Aging at 225$^{o}$C, 250$^{o}$C, 275$^{o}$C, 300$^{o}$C, and 325$^{o}$C for up to 900 hours........ 112

Figure 4.31 Arrhenius Plot of the Growth of Ni-Ge IMC Layers in AuGe Solder Joint on Electroless Ni:P Sample........ 113

Figure 4.32 Berkovich Tip [81]........ 115

Figure 4.33 Load-displacement Curve [83]........ 116

Figure 4.34 Hardness of Cu in the Electroless Ni:P Sample at Room Temperature........ 118

Figure 4.35 Reduced Modulus of Cu in the Electroless Ni:P Sample at Room Temperature.... 118

Figure 4.36 Hardness of Ni:P Layer at Room Temperature (a) AuGe on Electroless Ni:P (b) AuGe on Electrolytic Ni:P........ 120

Figure 4.37 Reduced Modulus of Ni:P Layer at Room Temperature (a) AuGe on Electroless Ni:P (b) AuGe on Electrolytic Ni:P........ 120

Figure 4.38 Hardness of Ni-Ge IMC at Room Temperature after 3000 hours Aging at 300$^{o}$C (a) AuGe on Electroless Ni:P (b) AuGe on Electrolytic Ni:P........ 122

Figure 4.39 Reduced Modulus of Ni-Ge IMC at Room Temperature after 3000 hours Aging at 300$^{o}$C (a) AuGe on Electroless Ni:P (b) AuGe on Electrolytic Ni:P........ 122

# CHAPTER 1 INTRODUCTION

## 1.1 High Temperature Electronics (HTE)

The operating temperature for commercial grade semiconductor parts is typically 0$^o$C to 70$^o$C. Even in industrial grade the range just extends from -40$^o$C to 85$^o$C [1]. However, there are applications for electronics in harsh operating environments that challenge traditional electronics. The precise definition of high temperature is elusive and varies depending on the application. The closest statement for high temperature may be taken as electronics operating at temperatures in excess of those normally encountered by conventional, silicon-based semiconductors or their auxiliary components [2]. In this work, all of the experiments were conducted at or above 200$^o$C in air.

## 1.2 Applications of High Temperature Electronics

The high operating temperature may be caused by the natural environment or high power dissipation by the component itself. High operating temperatures will effect component reliability and electronic performance. For example, the leakage current of a diode will increase in a high temperature environment; mechanical stress induced by a thermal expansion coefficient mismatch over a wide temperature range between different materials may cause cracking in solder joints.

In order to solve the problems caused by high temperature, many researchers have spent time on developing cooling systems. Cooling systems are primarily used when the high temperature is caused by power dissipation. In naturally high temperature environments, cooling systems can not provide a long-term working temperature for the electronics. Moreover, other

disadvantages of a cooling system are it creates additional failure modes; increases the volume and weight of the system; and increase cost and complexity. Electronics using high temperature durable components can work without a cooling system and provide high electrical and mechanical reliability.

There are some major industries that need high temperature electronics such as, oil and gas, space, aerospace and automotive.

Oil and gas industries: The demand for oil and gas increases every year. However, shallow nature resources that can be acquired easily are gradually being used up. Therefore, the drilling depth becomes deeper, which means higher operating temperature for drilling equipment. Measure-While-Drilling (MWD) is a type of well logging that is widely used today. It incorporates measurement tools into the drill string which can provide real time data such as position, temperature, strain, inclination, azimuth and fluid flow. With these data, engineers can control the system precisely to reach the oil reservoir [3]. Electronics used for MWD typically work in the temperature range of 150°C to 300°C. Besides oil and gas, this kind of equipment also can be used for drilling geothermal resources.

Space Exploration: A Venus mission as part of solar system exploration is a good example of a high temperature electronics application. The surface temperature of Venus is about 480°C. To land on the surface for collecting data, a Venus lander has to be capable of surviving at 480°C. NASA has already investigated high temperature electronics, communications and supporting technologies that can withstand 500°C for a Venus mission [4].

Aerospace applications: Aircraft for both commercial and military need high temperature electronics. The working temperature of an aircraft engine can reach 500°C. A full authority digital engine control (FADEC) is used to monitor and control the engine. It is hard-wired to

many sensors and actuators of the engine by a long, heavy harness. A FADEC needs to work closely enough to these sensors and actuators to maximize analog signal strength, and minimizing interference and noise [5]. The working temperature of electronics in an aircraft would be ranging from 150°C to 325°C [6].

Hybrid vehicle: The underhood temperature of traditional automotive electronics is around 125°C. A hybrid vehicle uses both an internal combustion engine and electric motors, which can increase the fuel efficiency and reduce air pollution. Hybrid vehicles will demand high power motor controls and drive electronics that can operate at higher temperatures than traditional automotive electronics. Integration of these power devices into electric motors may require an operating temperature ranging from 175°C to 200°C [7].

Table 1.1 summarizes major applications of high temperature electronics and their operational temperature, minimum duration and other environmental factors that may influence the devices.

Table 1.1 Applications Area and Characteristics for High Temperature Electronics [8][9]

| Application | Temperature(°C) | Minimum Duration | Duty | Other Environmental Factors |
|---|---|---|---|---|
| Well-logging Gas&Oil instrumentation | 150 to 300 | Few hours-years | Intermittent / cyclical or continuous | Temperature cycling, chemical, pressure, vibration |
| Geothermal | 150 to 400 | Few - 100 years | Intermittent cyclical | Temperature cycling, chemicals, pressure vibration |
| Aircraft systems on engine & smart transducers | 300 to 500 | 100 years | Intermittent cyclical | Temperature cycling, vibration, stress, fuel/ oil |
| Aircraft engine | 500 to 600 | 100 years | Intermittent cyclical | Temperature cycling, vibration/ shock |
| Automobiles | 150 to 250 | 8000 operating, 10 years shelf | Intermittent cyclical | Temperature cycling, fuel/oil, rough handling |
| Nuclear reactors | 200 to 450 | Months to years | Continuous | Radiation |
| Space exploration | 125 to 485 | Month to years | Intermittent / cyclical or continuous | Temperature cycling, chemical, pressure |

### 1.3 High Temperature Electronic Packaging

Electronic packaging is the process of assembling, interconnecting, embedding, or mounting electronic components, circuits or devices to substrates or boards [10]. Electronic packaging provides connectivity and proper protection for the electronics. Figure 1.1 shows a typical power electronics packaging structure. The main elements are [11]:

1. Semiconductor dies or chips: Electrical switches, such as IGBT, MOSFET, and rectifier.

2. Die attach: The attachment of the semiconductor devices' backside to the substrate.

3. Wire bond: Provides electrical interconnection between the top-side of the chip and the package terminals.

4. Substrate: It provides electrical routing between devices. Also, it needs to provide excellent thermal conductivity.

5. Encapsulant material: A conformal coating or potting applied on the whole component surface to provide environmental and in some cases mechanical protection. It may also provide high voltage insulation.

6. Base plate: It provides mechanical support, heat spreading and conducts the heat generated by the devices to the heat dissipation system.

7. Terminals and pins: They provide the electrical interface to the next level assembly.

8. Cover: The cover of the modules provides mechanical and environmental protection for the whole package.

The keys to successful high temperature electronic packaging include : die, die attach material, substrates, wire bond material, and encapsulant material that can provide excellent thermal, electrical performance and high reliability in high temperature operation. In the following sections, discussion is focusing on high temperature durable materials that can be used for die, die attach, substrate and encapsulant.

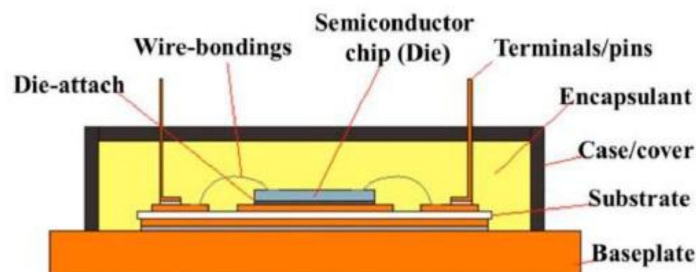


Figure 1.1 Typical Electronics Packaging Structure [11]

1.3.1 SiC Devices

Silicon-based semiconductor devices launched the revolution of electronics and computerization beginning in the1950s'. The number of transistor on one chip has grown from one to billions today. Silicon-based power devices are limited by a junction temperature at about 200$^oC$. Silicon-On-Insulator (SOI) integrated circuit (IC's) can be used at 300$^oC$ for low-power logic and signal processing. However, SOI is not suitable for high power devices, which typically need a vertical current flow structure. As a result, for power devices applications above 200$^oC$, people need to find better semicondutor materials that can replace Si.

In order to operate at higher temperatures and get better electrical performance, wide bandgap semiconductors (WBG) are a better choice than conventional semiconductor material like silicon and gallium arsenide. The electronic bandgap is the energy gap between the top of the valence band and the bottom of the conduction band. It represents the amount of energy required to promote a valence electron to become a conduction electron. The bandgap of Si and other common material are less than 1.5eV. WBG semiconductors, such as SiC, GaN and diamond have a bandgap of more than 3eV bandgap. Table 1.2 shown some physical characteristics of wide band gap semiconductors compared with Si and GaAs.

Table 1.2 Physical Characteristics of Si and Major WBG Semiconductors [12]

| Semiconductor material | Si | GaAs | 6H-SiC | 4H-SiC | GaN | Diamond |
|---|---|---|---|---|---|---|
| Bandgap (eV) | 1.12 | 1.43 | 3.03 | 3.26 | 3.45 | 5.45 |
| Dielectric constant, $\varepsilon_r$[1] | 11.9 | 12.1 | 9.66 | 10.1 | 9 | 5.5 |
| Electric breakdown field, $E_c$ (KV/cm) | 300 | 400 | 2500 | 2200 | 2000 | 10000 |
| Electron mobility, $\mu_n$($cm^2$/Vs) | 1500 | 8500 | 500-80 | 1000 | 1250 | 2200 |
| Thermal conductivity, $\lambda$ (W/cm-K) | 1.5 | 0.46 | 4.9 | 4.9 | 1.3 | 22 |

The reason why WBG materials can withstand higher temperature than others is that intrinsic carriers in WBG materials are much less than that in other semiconductor materials. The relationship between temperature and intrinsic carrier concentration can be expressed in the equation below.

$$n_i = \sqrt{N_c N_V} e^{-E_G/2KT}$$

In this equation, $N_C$ and $N_V$ are the effective electron and hole concentration in the semiconductor, $E_G$ is the energy bandgap in eV, $T$ is the temperature in Kelvin and $k$ is Boltzmann's constant. Figure 1.1 shows the intrinsic carrier concentration in silicon, 6H-SiC and 2H-GaN as a function of temperature.

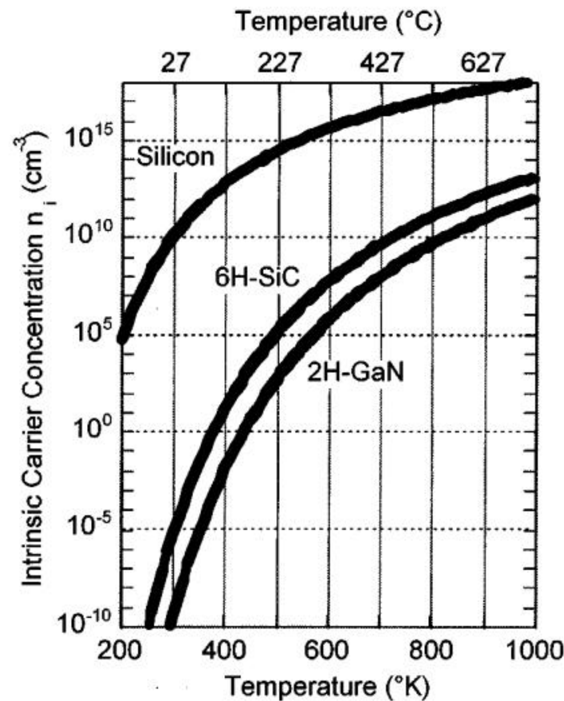


Figure 1.2 Semiconductor Intrinsic Carrier Concentration (n) versus Temperature for Silicon, 6H-SiC, and 2H-GaN [13]

When using a semiconductor material in micro-fabrication, an n-type or p-type doping around $10^{14}$ to $10^{17}$ $cm^{-3}$ concentration is created in the designed area to form p-n junctions. At room temperature, the intrinsic carrier concentration of silicon is around $10^{-10}$ $cm^{-3}$ which is negligible compare to the device doping concentration. However, at high temperature, there could be as many or more intrinsic carriers than doped carriers, which will influence the electrical characteristics of the device [13].

Besides low intrinsic carrier concentration, there are more characteristics that make SiC a very attractive candidate to replace conventional semiconductor material in high temperature applications [14][15].

High thermal conductivity: The thermal conductivity of SiC is about 4.9 W/cm-K which is more than three times higher than the 1.5 W/cm-K of Si. This means SiC devices can operate at extremely high power level. The heat generated by high power dissipation can be easily conducted out.

High breakdown voltages: With about 10 times higher electrical breakdown field strength than that of Si. SiC devices can be fabricated with a thinner drift layer and higher doping concentration than Si. This would dramatically reduce the device's volume in high voltage and high current applications. It can also reduce the on-state conduction losses.

High bonding energy: Large Si-C bonding energy makes SiC a thermally and chemically stable material with high hardness.

High saturation velocity: The saturation electron velocity of SiC is about $2\times10^{7}$ cm/sec, while, Si is $1\times10^{7}$ cm/sec. This property means SiC devices can work at high frequencies than Si.

With these properties, SiC is gradually replacing traditional semiconductor material in high temperature power electronics applications.

1.3.2 Die Attach Solder Material

Die attach is one of the most challenging aspects of high temperature packaging and was specially investigated in this work. A good die attachment needs to provide good mechanical strength, high thermal and electrical conduction. For example, according to MIL-STD-883 standard, a 5mm*5mm die must have a shear strength above 0.1kg/mm$^2$. The main categories of die attach materials are soft solder, epoxies, silver based die attaches (silver glass and silver nanoparticles), hard solders, and transient liquid phase.

Alloys that melt between 180°C and 190°C, such as, Sn60/Pb40 and Sn63/Pb37 were widely used in electronics assembly. With the ban on Pb in most electronics, Sn-Ag-Cu alloys with melting temperature from 217-227°C are more commonly used. Obviously, they can not be used in high temperature applications. Figure 1.3 summarized solder alloys that have a melting point above 200°C and their application possibilities.

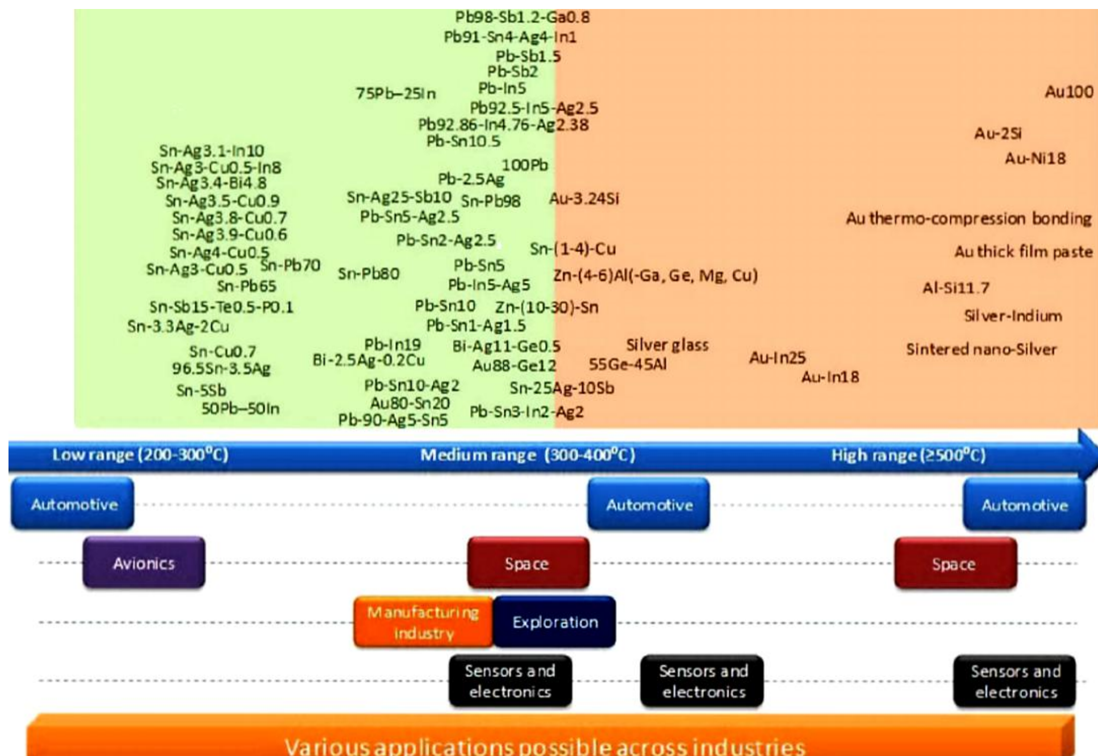


Figure 1.3 Melting Ranges for Typical High Temperature Solders and Applications [16]

Typically, the operating temperature of solder is lower than their melting temperature by 50°C to 100°C. For example, Sn-Ag-Cu alloys with melting temperatures from 217°C to 227°C can be used in 125°C to 150°C applications and Bi-Ag alloys with a melting temperature of approximately 260°C are suitable for 200°C. They are both very promising candidates to replace lead-based solder materials that are harmful to the environment and humans. BiAgX® from Indium Corporation was developed based on the Bi-Ag alloy, which has better wetting and solderability [17]. Zhang, et al. and Shen, et al. have shown that the reliability of BiAgX based on 200°C aging and thermal cycling test results are good enough for commercial applications [17][18].

Due to the excellent oxidation resistance, Au-based hard solder alloys are good choices for high temperature die attach application above 225°C. With high Au content, the solders have high melting point and high electrical and thermal conductivity. They can be processed into solder preforms, which can accurately control solder volume. Moreover, solder preforms are flux free. No cleaning process is needed after assembly. AuGe12, AuSi3, AuIn18, and AuSn20 are normally used gold-based solder alloys. Zheng, et al. has evaluated AuSi as a reliable die attach material with Mo:Mn/Pd/Au metallization on AlN substrate after 3000 hours aging at 325°C [19].

Unlike other Au-based solder alloys, Au-Sn20 can achieve a higher operating temperature than its eutectic temperature through a process called liquid phase transient bonding (LPT). LPT includes at least two kinds of metals. The one with the lower melting point is called the melting point depressant (MPD) element [20]. During the soaking stage, MPD element (Au-Sn20) forms a liquid phase interlayer, due to its low melting point. While the MDP moves to the interface between the substrate and the solder, it also diffuses into the metal bulk (Au) with high

melting temperature. The interdiffusion shifts the composition percentage. As a result, the melting point of the liquid is also changed. In summary, LPT bonding can achieve a higher operating temperature than the assembly temperature. Johnson, et al. [21] has shown with 20µm Au and 6.2µm Sn, the solder joint can endure 400°C aging for 2000 hours.

Recently, silver sintering paste has attracted attention as a Pb-free die attach material as well as a high temperature die attach. Interest in sintered silver pastes can be attributed to its low processing temperature, high melting temperature and high electrical and thermal conductivity. Silver powders at the nano or micron scale are mixed with additives (thinner, binder, dispersant) uniformly to form a paste. During the sintering, all organic materials evaporate and combust, leaving only silver particles. Necks grow between the silver particles during sintering, which bonds them together and forms the die attachment. The sintering temperature is usually between 200°C to 300°C and the process can be pressure or pressureless. Göbl, et al. [22] investigated a high-pressure silver particle sintering process which is commercially used for 175°C power modulus. Experimental results have revealed that metallization on both the die and the substrate may strongly influence the die attach strength. Yu, et al. [23] used a pressureless sintering process with micrometer-size Ag particles. This material was found to be reliable with Ag thin film die metallization and Ag thick film metallization after 8000 hours aging at 300°C and with PdAg thick film after 2000 hours. However, Au metallized die or Au thick film substrates had low shear strength due to the formation of Ag a depletion layer.

1.3.3 Substrate Materials

Organic-based printed circuit boards are widely used in the electronics manufacturing industry. However, organic substrates can not work above their glass transition temperature ($T_g$), ranging from 125°C to 200°C. As a result, ceramic materials like $Al_2O_3$, AlN and BeO have been

used in high temperature applications. Table 1.3 shows the properties of a number of potential high temperature substrate materials at room temperature.

Table 1.3 Package Substrate Material Parameters at 300K [24]

| Material | CTE (ppm/K) | Mass Density ($g/cm^3$) | Thermal conductivity ($W/m{\cdot}K$) |
| --- | --- | --- | --- |
| AlN substrate | 4.5 | 3.3 | 200 |
| Beryllia (BeO) substrate | 6.1 | 2.9 | 2.80 |
| $Al_2O_3$(Alumina substrate) | 6.5 | 3.9 | 30 |

Direct bonded copper (DBC) substrates are widely used in power electronics packaging. With excellent electrical and thermal conductivity, it can provide high current handling capacity. The copper can be bonded on $Al_2O_3$, AlN, and BeO. Among these, $Al_2O_3$ is the most commonly used as it is the lowest cost. However, the CTE mismatch between copper and the ceramic may cause failure in thermal cycling. The CTE mismatch effect on reliability can be effected by varying the thickness of copper and $Al_2O_3$. For example, Dupont, et al. studied the relationship between copper thickness and reliability of DBC substrate in high temperature cycling. They claim that the thinner metallization layer will result in longer ceramic substrate lifetime [25]. This problem still cannot be completely avoided, but delayed by proper design.

### 1.3.4 Surface Finishing

The copper surface of a DBC substrate is easily oxidized in high temperature applications. To protect the copper surface from oxidizing and deterioration, a thin layer of surface finish is necessary. A surface finish can also be referred to as a coating. Gold, palladium, silver and nickel are normally used for DBC surface coating. Table 1.4 shows different surface finish types. Table 1.5 shows the electrical and thermal properties of these metals.

Table 1.4 Surface Finishing Types [26]

| Metallic Coatings for DBC: | -ENIG (Electroless Nickel/Immersion Gold)<br>-Electrolytic Ni /Au (Electrolytic Nickel / Gold)<br>- ENEPIG (Electroless Nickel/ Electroless Palladium / Immersion Gold)<br>-Electroless Nickel-Immersion Palladium<br>-Immersion Ag<br>-Electrolytic Ag<br>-Nickel/Palladium-Immersion |
|---|---|

Table 1.5 Electrical and Thermal Properties of Ag, Au, Ni and Pd [27]

| | Silver | Gold | Nickel | Palladium |
|---|---|---|---|---|
| Electrical conductivity (10.E6 Siemens/m) | 62.1 | 44.2 | 14.3 | 9.5 |
| Electrical resistivity (10.E-8 Ohm.m) | 1.6 | 2.3 | 7.0 | 10.5 |
| Thermal Conductivity (W/m.k) | 420 | 317 | 91 | 72 |
| Melting point($^{o}$C) | 961 | 1064 | 1455 | 1555 |

Compared with the cost of gold and palladium, the cost of silver makes it an attractive option. However, silver finishing will be tarnished easily in high sulfur environments and Ag migration failures can occur under specific conditions [28].

Gold plating has excellent oxidation resistance and does not exhibit electromigration in most environments. However, the formation of brittle Au-Cu intermetallics like $Au_3Cu$ and $AuCu_3$ will weaken the strength of the assembly. As a result, a layer of nickel is often plated under the gold to inhibit interdiffusion between the Au and Cu and increase the durability of the gold plating. The typical thicknesses are 3-6 µm nickel followed by 0.25-1.3 µm of gold [26]. In some processes, an electroless palladium layer is used to prevent ‘black-pad’ failure in ENIG

finishes, creating an ENEPIG finishing [29]. Different nickel plating methods will be discussed in the next section.

#### 1.3.4.1 Electroless & Electrolytic Nickel Plating

With excellent solderability and good oxidation resistance, Ni/Au (nickel/gold) surface finishes are widely used in the electronics industry. There are two plating methods for nickel; electroless and electrolytic.

Electroless Ni is deposited by an auto-catalytic chemical reaction. During the plating process, a small amount of phosphorous or boron may residue in the Ni. Phosphorous is more commonly used than boron. Electroplated Ni is a process that uses DC current to reduce dissolved Ni cations in a plating bath and form a Ni layer on the cathode. ENIG has already been accepted by the industry as a common surface finish, which makes electroless Ni more commonly used than electrolytic Ni. The biggest disadvantage of electrolytic Ni plating is with patterned Cu, electrical contact to all of the Cu pads/ traces are required for electroplating, which is difficult. However, some researchers claim that electroplated Ni may have better performance in some aspects. For example, Islam, et al. [30] claimed that a 3μm electrolytic Ni layer can protect the Cu surface from Sn-Ag-Cu solder dissolution for more than 180min at 250$^{o}$C. While the electroless Ni:P layer was broken and Kirkendall voids were formed during the process.

**Plating Composition:** Electroless-plated Ni cannot plate 100% pure Ni, since solutions like, sodium hypophosphite, sodium borohydride, and dimethylaminoborane are used as reducing agents during the plating process [31]. Among them, the hypophosphite bath is the most commonly used. Equation 1.1-1.3 [32] is the simplified reaction for electroless Ni:P plating. In Equation 1.1, the reducing agent $H_2PO_2^-$ is oxidized to $H_2PO_3^{2-}$ and the extra ions reduce $Ni^{+2}$ to atomic nickel. Equation 1.3 is the sum of the oxidation and reduction equations. Some reduce

agent is also reduced during the reaction which is why electroless Ni plating is not 100% pure nickel.

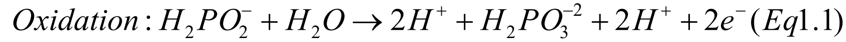

$$Oxidation: H_2PO_2^- + H_2O \rightarrow 2H^+ + H_2PO_3^{-2} + 2H^+ + 2e^- (Eq1.1)$$

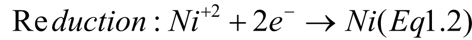

$$Reduction: Ni^{+2} + 2e^- \rightarrow Ni (Eq1.2)$$

$$Ni^{+2} + H_2PO_2^- + H_2O \rightarrow Ni + H_2PO_3^- + 2H^+ (Eq1.3)$$

In addition, ternary alloy of Ni:P:X where X can be tungsten, chromium, molybdenum, copper and tin can be formed by using particular formulations [33]. In nickel phosphorous plating, nickel with10%-13% phosphorous weight percentage is considered high phosphorous nickel. 5%-9% is medium phosphorous nickel. Below 5% is low phosphorous nickel. The high phosphorous nickel has better corrosion resistance and the low phosphorous nickel has the highest hardness [34].

Nickel sulfate and nickel chloride are usually used as Ni ion sources in electrolytic plating. Ni ions have a reduce reaction with the electron at the cathode and form a layer of Ni on it. Typically, boric acid is used as a buffer agent. Besides pure Ni, with adding other additives like phosphorous acid or cobalt sulfate, electrolytic Ni alloys Ni:P and Ni:Co are available.

**Plating Distribution:** Electroless-plated nickel is more uniform than the electroplated nickel. In the electrolytic plating process, thickness depends on current density. Locations with higher current density have higher thickness. Figure 1.4 compares the uniformity of the electroless and electrolytic Ni. When using electrolytic plating, the sharp corners tend to be plated faster than the concave surfaces.

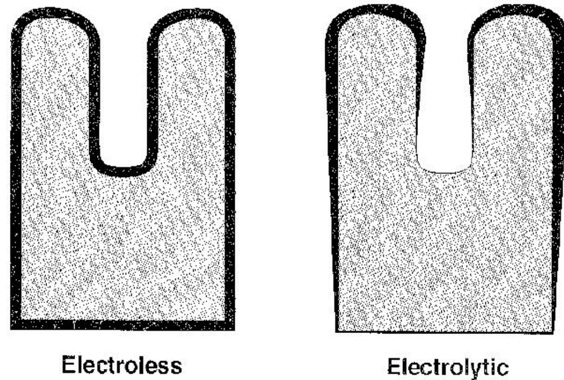


Figure 1.4 Note the Uniformity of the Electroless Coating as Compared with that of Electrolytic Ni Deposit [35]

**Crystal structure:** Research results indicate that as deposited medium and low phosphorous electroless Ni are a mixture of amorphous and microcrystalline nickel phases [36]. High phosphorous electroless Ni is amorphous [37]. Also, both amorphous and crystalline structures were found in electroplated nickel [38].

Nickel composition ratio and plating method may influence the reliability of the solder joint. Yoon, et al. [39] has shown that Ni:(7-10%)P was more reliable than Ni:(1-3%)B after high temperature (150°C) aging of Sn-3.5Ag BGA solder spheres as determined by ball shear analysis. The brittle $Ni_3Sn_4$ intermetallic grew faster on the Ni:B compared to the Ni:P layer. At higher temperatures, Johnson, et al. [40] have shown degraded die shear strength for SiC die attached with AuSn liquid transient phase (LTP) bonding to an electroless Ni:P electroplated Au finish on Cu with aging at 400°C due to Kirkendall voiding. No degradation was observed with an electroplated Ni/Au surface finish. Electroless or electrolytic and which alloy will be superiority will depend on the application and die attach material.

1.3.5 Electronic Coating Technology

Electronics operating in harsh environments face more challenges than in normal environments. For example, in a high temperature environment with bias, silver can migrate

along insulating surface materials and cause a short circuit failure. For example, Henson [7] reported short circuit failures between a 40 mil gap caused by silver migration at 300°C with bias. As a result, protective coatings are quite necessary for electronic devices.

Typical electronic coating technologies include conformal coating, potting and encapsulation. An electronic coating can provide protection for electronic components on a printed circuit board (PCB) or for semiconductor chips in a power electronics module. Especially for electronics working in harsh environments such as high moisture, high voltage, and high temperature, electronic coating is necessary.

Conformal coating is normally a thin layer (25-75μm) of polymer, which conforms to the circuit board topology [41]. Figure 1.5 is a metal nozzle spraying conformal coating on a PCB. Materials like acrylic, epoxy, polyurethane, silicones, parylene, and copolymer are used as conformal coating materials. The material can be applied in the board by spraying, dipping, brushing or specialized vacuum deposition. Among them, the coating process of parylene is relatively special. Figure 1.6 is the Parylene N coating process. Different Parylene coatings may need different temperatures in these steps [42]. Generally, Parylene coatings have 3 steps and the process is called chemical vapor deposition (CVD). First, the dimer material must be heated until it vaporizes into dimeric gas in a vacuum chamber. Then, the dimer is cleaved to monomeric form during the pyrolysis process. Finally, the monomer gas can be deposited on targets and form a thin uniform Parylene layer at room temperature [43].

Figure 1.5 Conformal Coating [44]

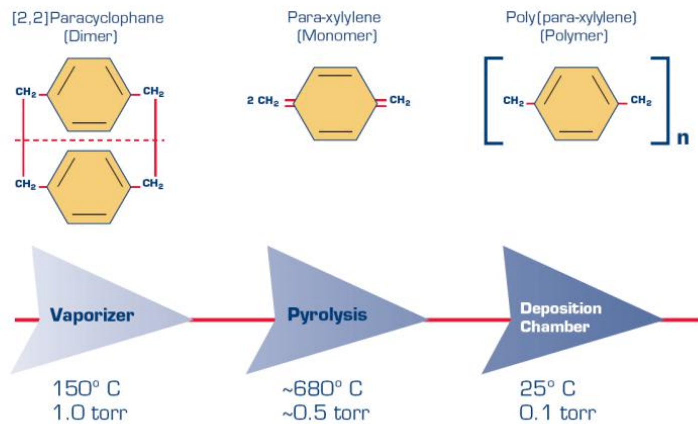


Figure 1.6 Parylene Coating Process [43]

Compared with conformal coating, potting and encapsulation are to immerse the whole board or several components in the coating compound [45]. The coating thickness is much thicker than the conformal coating (see Figure 1.7). Potting can provide higher thermal or physical shock and vibration resistance than conformal coating. However, it is hard to remove the coating if the components need to be replaced. The concept of encapsulation is quite similar with potting, on some occasions they are synonyms.

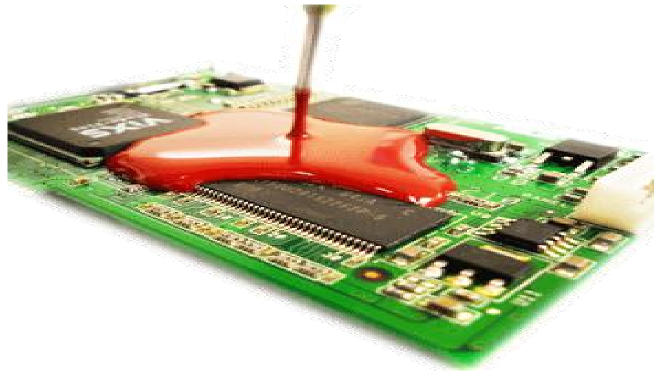

Figure 1.7 Potting and Encapsulation [46]

To select proper coating methods and materials, some factors must be taken into consideration. The operating environment will determine the moisture resistance, applicable temperature range and dielectric properties needed of the coating material. Long duration applications may require longer reliability testing, likewise, problems like coefficient of thermal expansion (CTE) mismatch, adhesion degradation, decomposition will cause unexpected failure in the application. In this research, a conformal coating material, Parylene HT® ( Special Coating System Inc.) and a potting material Duraseal 1531® (Cotronics Corporation) were both evaluated at 300°C.

**1.4 Research Outline**

The goal of this thesis was to evaluate high temperature applicable materials. This thesis is composed of 5 chapters.

Chapter 2 presents an investigation of electronic coating materials. Parylene HT and a silicone potting material from Cotronics were evaluated at 300°C. The test pattern was designed to test the electrical insulation performance of the materials under 5000V bias. Adhesion testing for Parylene HT on AlN and electroplated gold was also studied.

Chapter 3 describes die attach using BiAgX solder on different types of Ni/ Au surface finishes. The reliability based on high temperature storage (200$^{o}$C) and thermal cycling test is discussed.

Chapter 4 reports die attach using AuGe12 solder on different types of Ni/Au surface finishes. 300$^{o}$C thermal aging and -55$^{o}$C to 300$^{o}$C cycling tests was conducted. The growth kinetics of Ni-Ge intermetallic were calculated.

Chapter 5 concludes this thesis and suggests directions for the future work.

# CHAPTER 2 HIGH TEMPERATURE ELECTRONIC COATING

## 2.1 Introduction

Parylene is the trade name of a variety of polyxylylene polymers that forms a polymer film on the target surface by chemical vapor deposition (CVD). Figure 2.1 is the chemical structure of the Parylenes. With excellent chemical stability and electric properties, Parylenes can be used as conformal coating or dielectric barrier layer in electrical assemblies.

Commercially available Parylene products include Parylene C, N, D, and HT. Table 2.1 shows the electrical properties of Parylene coatings. All Parylene coatings have high dielectric strength, which allows them served in high voltage insulate application. Among them, Parylene N and C are the most commonly used. However, the continuous working temperature for Parylene N is only 60°C, and that for Parylene C is 80°C which can not be used in high temperature application (see Table 2.2).

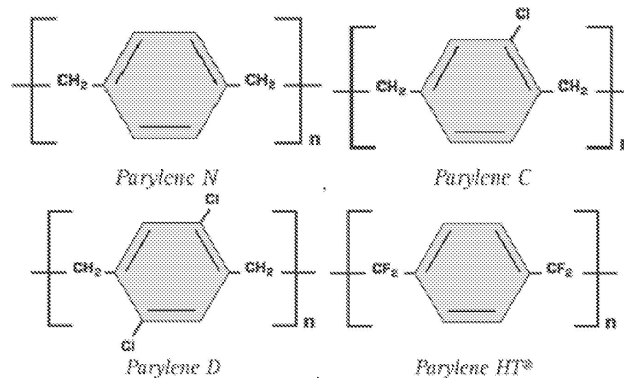


Figure 2.1 Chemical Structure of Parylenes [47]

Table 2.1 Electric Properties of Parylenes [48]

| Properties | Method | Parylene N | Parylene C | Parylene D | Parylene HT | Acrylic (AR)[a,b] | Epoxy (ER)[a,b] | Polyurethane (UR)[a,b] | Silicone (SR)[a,b] |
|---|---|---|---|---|---|---|---|---|---|
| Dielectric Strength V/mil | 1 | 7,000 | 5,600 | 5,500 | 5,400 | 3,500 | 2,200 | 3,500 | 2,000 |
| Volume Resistivity, ohm-cm, 23°C, 50% RH | 2 | $1.4 \times 10^{17}$ | $8.8 \times 10^{16}$ | $1.2 \times 10^{17}$ | $2.0 \times 10^{17}$ | $1.0 \times 10^{15}$ | $1.0 \times 10^{16}$ | $1.0 \times 10^{13}$ | $1.0 \times 10^{15}$ |
| Surface Resistivity, ohms, 23°C, 50% RH | 2 | $1.0 \times 10^{13}$ | $1.0 \times 10^{14}$ | $1.0 \times 10^{16}$ | $5.0 \times 10^{15}$ | $1.0 \times 10^{14}$ | $1.0 \times 10^{13}$ | $1.0 \times 10^{14}$ | $1.0 \times 10^{13}$ |
| Dielectric Constant 60 Hz | 3 | 2.65 | 3.15 | 2.84 | 2.21 | – | 3.3 – 4.6 | 4.1 | 3.1 – 4.2 |
| 1 KHz | | 2.65 | 3.10 | 2.82 | 2.20 | – | – | – | – |
| 1 MHz | | 2.65 | 2.95 | 2.80 | 2.17 | 2.7 – 3.2 | 3.1 – 4.2 | 3.8 – 4.4 | 3.1 – 4.0 |
| Dissipation Factor 60 Hz | 3 | 0.0002 | 0.020 | 0.004 | <0.0002 | 0.04 – 0.06 | 0.008 – 0.011 | 0.038 – 0.039 | 0.011– 0.02 |
| 1 KHz | | 0.0002 | 0.019 | 0.003 | 0.0020 | – | – | – | – |
| 1 MHz | | 0.0006 | 0.013 | 0.002 | 0.0010 | 0.02 – 0.03 | 0.004 – 0.006 | 0.068 – 0.074 | 0.003 – 0.006 |

[a]*Handbook of Plastics, Elastomers, and Composites*, Chapter 6, "Plastics in Coatings and Finishes," 4th Edition, McGraw Hill, Inc., New York, 2002.
[b]*Conformal Coating Handbook*, Humiseal Division, Chase Corporation, Pennsylvania, 2004.

**Test Methods:**
1. ASTM D 149
2. ASTM D 257
3. ASTM D 150

Table 2.2 Thermal Properties of Parylenes [48]

| Properties | Method | Parylene N | Parylene C | Parylene D | Parylene HT | Acrylic (AR) | Epoxy (ER) | Polyurethane (UR) | Silicone (SR) |
|---|---|---|---|---|---|---|---|---|---|
| Melting Point (°C)[a] | 1 | 420 | 290 | 380 | >500 | 85 – 105[b] | NA | ~170[b] | NA |
| T5 Point (°C) (modulus = 690 MPa) | 2, 3 | 160 | 125 | 125 | 377 | – | 110 | ~30 | ~125 |
| T4 Point (°C) (modulus = 70 MPa) | 2, 3 | >300 | 240 | 240 | >450 | – | 120 | – | ~80 |
| Continuous Service Temperature (°C) | – | 60 | 80 | 100 | 350 | 82[b] | 177[b] | 121[b] | 260[b] |
| Short-Term Service Temperature (°C) | – | 80 | 100 | 120 | 450 | – | – | – | – |
| Linear Coefficient of Thermal Expansion at 25°C (ppm) | 4 | 69 | 35 | 38 | 36 | 55 – 205[b,c] | 45 – 65[b,c] | 100 – 200[b,c] | 250 – 300[b,c] |
| Thermal Conductivity at 25°C (W/(m•K)) | 5, 6 | 0.126 | 0.084 | – | 0.096 | 0.167 – 0.21[c,d] | 0.125 – 0.25[c,d] | 0.11[c,d] | 0.15 – 0.31[c,d] |
| Specific Heat at 20°C (J/(g•K)) | – | 0.837 | 0.712 | – | 1.04 | 1.04[b] | 1.05[b] | 1.76[b] | 1.46[b] |

[a]The temperature at which heat flow properties show signs of change.
[b]*Handbook of Plastics, Elastomers, and Composites*, Chapter 6, "Plastics in Coatings and Finishes," 4th Edition, McGraw Hill, Inc., New York, 2002.
[c]*Coating Materials for Electronic Applications*, Licari, J.J., Noyes Publications, New Jersey, 2003.
[d]*Lange's Handbook of Chemistry*, 5th Edition, McGraw Hill, Inc., New York, 1999.

**Test Methods:**
1. DSC
2. Taken from Secant modulus-temperature curve (except Parylene HT)
3. ASTM 5026 (Parylene HT only)
4. TMA
5. ASTM C 177 (except Parylene HT)
6. ASTM 1461 (Parylene HT only)

Parylene HT is the newest commercial available Parylene product provided by Special Coating System Inc. (Indianapolis, IN, USA) [48]. Compared with other Parylenes, it consists of fluorine atom instead of alpha hydrogen in the N dimer [48]. Parylene HT was specially invented for high temperature application with a melting point higher than 500°C. In Table 2.2 the continuous service temperature of Parylene HT is 350°C, which is much higher than the others.

Tung et, al. [49] reported that Parylene HT successfully served as an insulating liner layer for through-Si-via and also as an interlayer dielectric in 3D interconnection at 250°C and 300°C. In this work, Parylene HT was investigated as a dielectric coating on AlN (Aluminum Nitride) thin film structure at 300°C. Adhesion performance on both electroplated gold and AlN substrates was also studied.

Silicones are a family of polymers containing inert, synthetic compound made up of repeating units of siloxane [50]. Typically, silicones are rubber-like with good heat resistance and are used as adhesives, sealants, lubricants, and electrical insulation. Silicone materials have wide operating temperature range from -155°C to 300°C which can be used in high temperature applications. Duraseal 1531 silicone putty from Cotronics Corp. (Brooklyn, NY, USA) offers high bond strength, high temperature stability, and excellent electrical properties (see Table 2.3). In this work, Duraseal 1531 was evaluated as a potential electronic encapsulant for 300°C applications.

Table 2.3 Properties of Duraseal 1531 [51]

| **Product** | **1531** |
|---|---|
| **Max Use Temp. °F** | **800** |
| Continuous Service Temp. °F | 650 |
| Composition | Silicone |
| Viscosity | Putty |
| Toxicity | Low |
| Density (#/ft$^3$) | 80 |
| Elongation (%) | 250 |
| Hardness Shore | A31 |
| Tensile Strength (psi) | 275 |
| Specific Heat (BTU/# °F) | 0.35 |
| Dielectric Constant (@ $10^8$ cps) | 3.9 |
| Volume Resistivity (ohm-cm) | $10^{11}$ |
| Dielectric Strength (volts/mil.) | 500 |
| Thermal Conductivity* (@ 500 °F) | 2.0 |
| Solids Content (%) | 98 |
| Shrinkage (%) | 1 |
| Shelf Life (months) | 6-9 |
| Tack Free Time (min.) | 30 |
| Full Cure Time (hrs. - ¼" Bead) | 24 |
| Color | Gold |

## 2.2 Test Vehicle

2.2.1 Substrate

The substrate used in this experiment was one side polished 3.0 inch ×3.0 inch × 0.025 inch (Length × Width × Height) AlN substrate from Stellar Industries (Millbury, MA, USA).

The substrate was first cleaned in a 5% HCL solution for 10 seconds then rinsed with DI water for 30 seconds. To dehydrate the substrate before photoresist coating, it was baked at 120°C for 20 minutes. The photoresist, AZ4620 from AZ Electronic Materials (Martin, SC, USA) was applied uniformly on the substrate by spinning at 3000 RPM for 30 sec. After spinning, the substrate was soft baked on a hotplate at 110°C for 2 minutes. The substrate was exposed for 4 cycles (4 seconds per cycle) with a Karl Suss MA6 Mask Aligner.

The AZ 400 developer was diluted 1:2 with DI water, which was used to develop the photoresist for 45 seconds after exposure. Then the substrate was rinsed with DI water and dried with nitrogen. The substrate was put in a vacuum chamber for thin film metal deposition. The deposition sequence was: e-beam evaporation of 25nm Ti, sputtering of 50nm Ti:W and then e-beam evaporation of 50nm Au. The Ti layer was to provide good adhesion to the substrate. The Ti:W layer (10% Ti and 90% W (wt.%)) was a diffusion barrier to prevent interdiffusion between the Ti and Au at 300°C. The thin layer of Au was deposited as the seed layer for electrolytic gold plating.

Prior to the electroplating process, the substrate was first electroplated with Otrostrike C® solution from TECHNIC Inc. (Cranston, RI, USA) at 40°C for 5 minutes. This pre-plating solution improved adhesion between the thin film gold and the electroplated gold. Then, Techni-

Gold 434 HS solution was used to deposit 2 μm of gold on the substrate. The current density was set to 1-2 A/ft$^2$ during the plating process.

2.2.2 Encapsulation

The test vehicle is shown in Figure 2.2. The pattern consisted of two tips tapering to a point leaving a 10 mil or 5 mil gap. At the other end, a square pad was defined, which was used for applying 5000 V during the high voltage tests. Each substrate has 19 pairs of 5mil gap tips and 19 pairs of 10 mil gap tips.

After dicing, the substrate was sent out to Special Coating Systems for deposit of a 14.5 μm thick layer of Parylene HT.

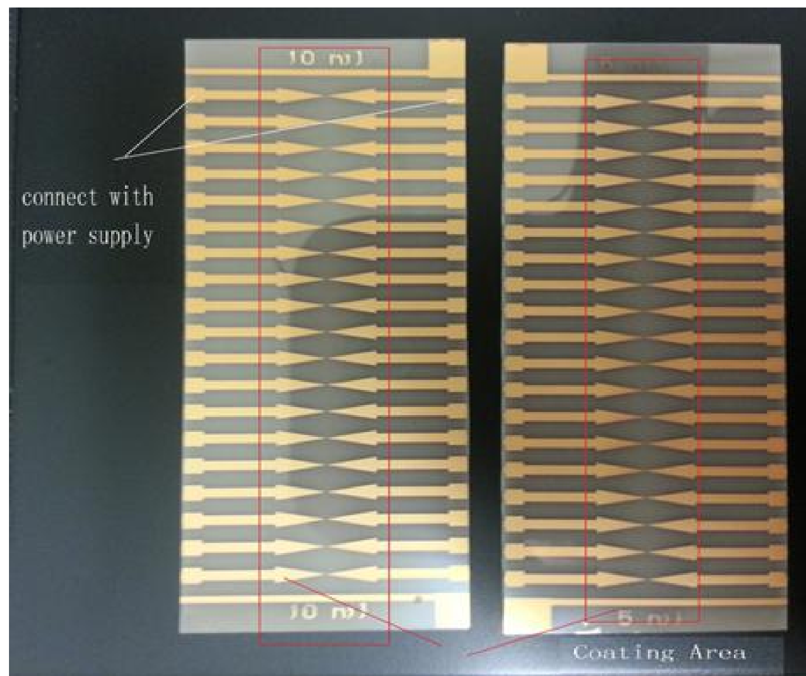


Figure 2.2 High Voltage Breakdown Test Vehicle

The adhesion between Duraseal 1531 and the substrate is poor. To improve the adhesion between the silicone and substrate, a silicone primer CF1-135 (NuSil Technology) was coated by hand on the sample surface. After dried 30 minutes at room temperature, Duraseal 1531 was applied on the surface using a piece of ceramic as a doctor blade with the 0.15 mm thick Kapton

tape on both sides (Figure 2.3). The Duraseal 1531 was cured at room temperature for 24 hours in the air.

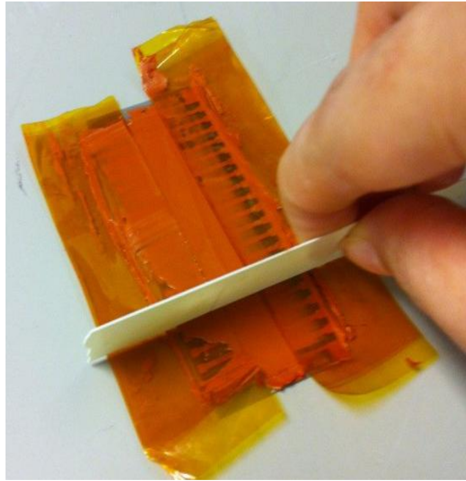

Figure 2.3 Apply Duraseal 1531 on Substrate

## 2.3 Breakdown Voltage Without Coating

The test was conducted on a probe station with hotplate (see Figure 2.4). The probes were connected with Keithly 248 programmable voltage supply. The maximum voltage of the power supply was 5000V and the ramp was set to 10V/sec. The hotplate was heated at 300$^{o}$C during the test.

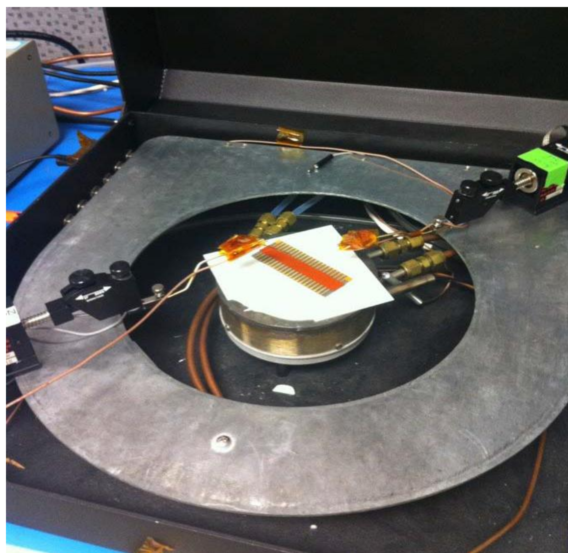

Figure 2.4 Probe Station

Table 2.4 shows the breakdown voltage without any coating on it. The breakdown voltage of the 10mil structure was about 100 V higher than that of the 5mil structure. Figure 2.5 shows the tip surface after breakdown test under an optical microscope.

Table 2.4 Initial Breakdown Data Without Coating

| NO. | Breakdown voltage (V) 5mil | Breakdown voltage (V) 10mil |
|---|---|---|
| 1 | 526 | 645 |
| 2 | 553 | 625 |
| 3 | 486 | 580 |
| 4 | 429 | 548 |
| 5 | 557 | 695 |
| 6 | 482 | 533 |
| 7 | 546 | 640 |
| 8 | 562 | 679 |
| 9 | 554 | 629 |
| 10 | 559 | 658 |
| AVG | 525.4 | 623.2 |

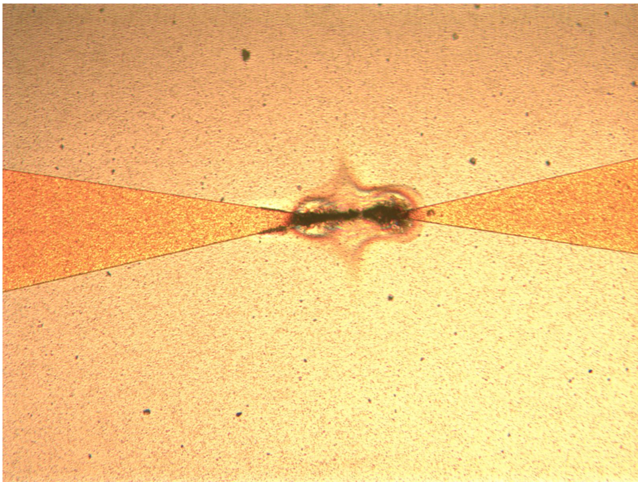

Figure 2.5 High Voltage Breakdown Surface

## 2.4 Aging Test

The test was conducted in air at 300°C without bias. The samples were taken out at predefined intervals for high voltage breakdown testing. The leakage current was measured with a Keithley 248 power supply. Figure 2.6 and Figure 2.7 plot the leakage current as a function of aging hour for Parylene HT and Duraseal 1531 respectively.

For the Parylene (Figure 2.6), there was an increase in leakage current during aging. The leakage current data of Parylene HT aged for 2000 hours was missing, since the Parylene HT was observed to peel off from the substrate surface (see Figure 2.8). All of the Duraseal 1531 coated samples survived 2000 hours aging at 300°C.

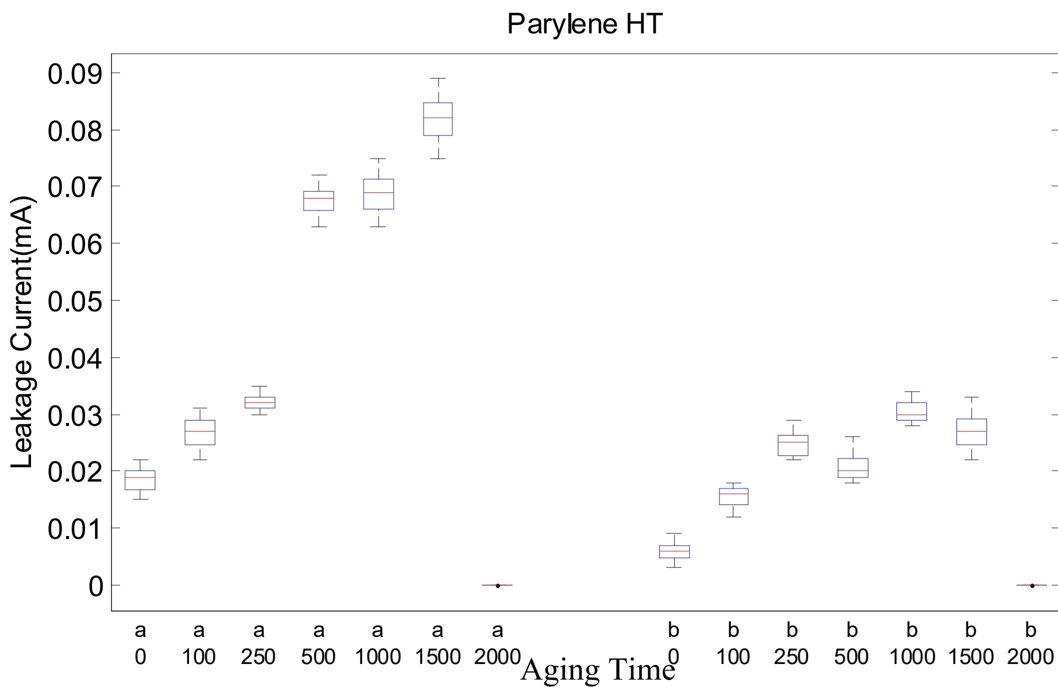


Figure 2.6 Leakage Current versus Aging Time at 300°C of Parylene HT (a) 5 mil (b) 10 mil

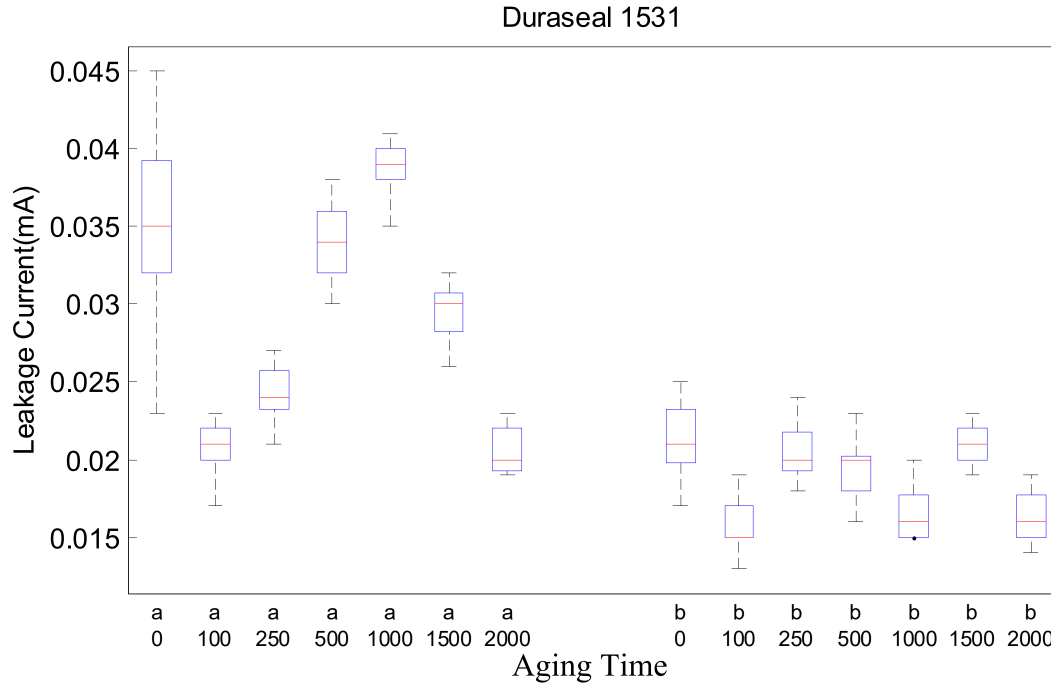


Figure 2.7 Leakage Current Versus Aging Time at 300ºC of Duraseal 1531 (a) 5 mil (b) 10 mil

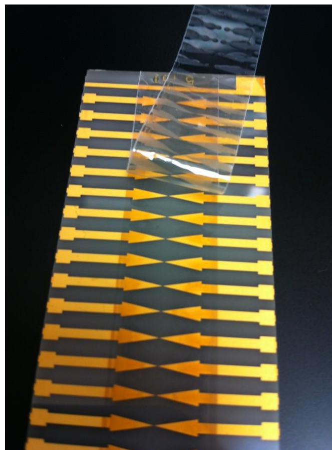

Figure 2.8 Parylene HT Peel Off after 2000 hours Aging at 300ºC

## 2.5 Parylene HT Adhesion Test

From the results of the aging test, the adhesion loss of Parylene HT with high temperature aging merited additional study. As a result, tests were designed to evaluate the adhesion performance of Parylene HT on both one side polished AlN and electroplated gold.

To get the adhesion strength between Parylene HT and AlN substrates, blank AlN substrates were deposited with Parylene HT. To analysis the adhesion strength for electroplated gold, a special pattern was designed (see Figure 2.9). The fabrication process was the same as used in fabricating the substrates for the leakage current experiment.

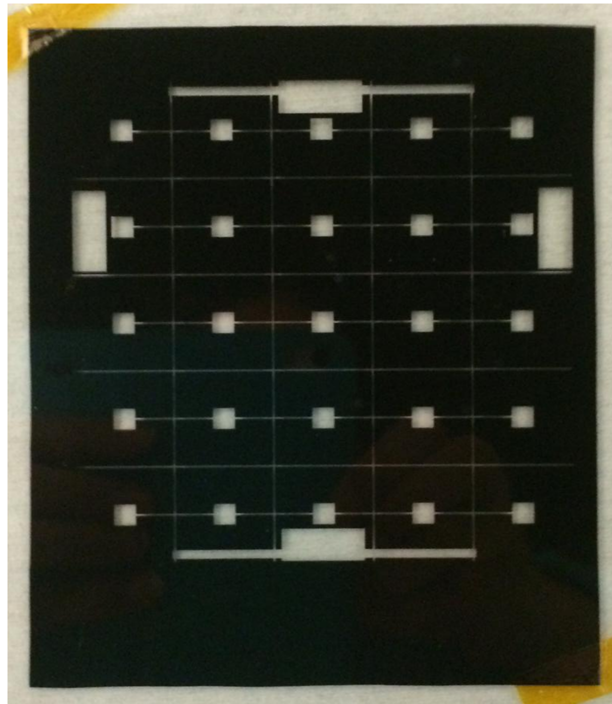

Figure 2.9 Mask of Parylene HT on Electroplated Gold Test Vehicle

After Parylene HT coating, one AlN substrate was diced into 25 individual test coupons after Parylene HT deposition. The aluminum studs from Quad Group Inc. (Spokane, WA, USA) coated with epoxy on the end were aligned to the sample surface and held in place with a clamp (see Figure 2.10). The epoxy cure was conducted at 150$^{o}$C for 1 hour. The pull test is illustrated in Figure 2.11.

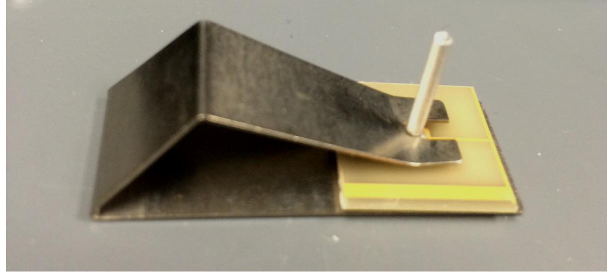

Figure 2.10 Parylene HT Adhesion Test Sample

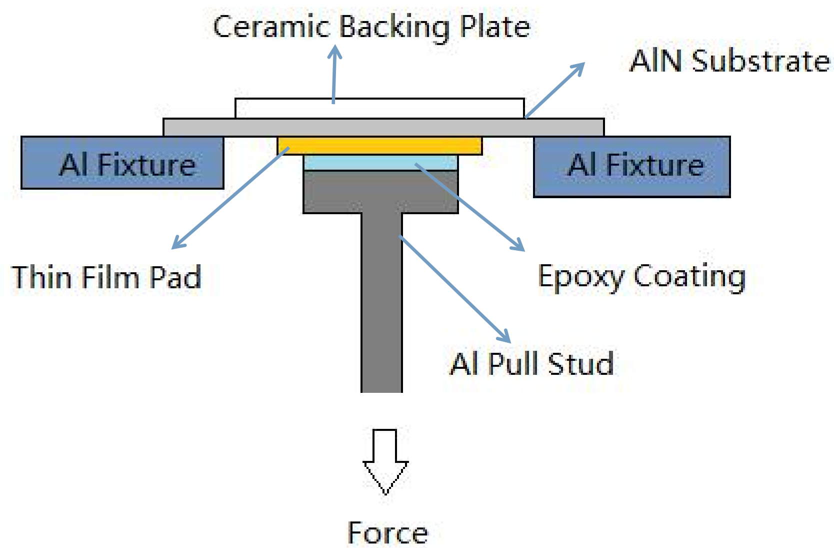


Figure 2.11 Illustration of Pull Testing

Figure 2.12 plots the adhesion strength of Parylene HT on electroplated gold and AlN as a function of aging time at 300$^{o}$C. Both surfaces had dramatic decreases in adhesion strength after aging. The as-built and 100 hours aging data of Parylene HT on AlN could not be measured, since the failure was in the AlN, not on the Parylene HT to AlN interface. Even though the Parylene HT adhesion strength on AlN was a little higher than that on the electroplated gold surface, both of them failed after 2000 hours aging at 300$^{o}$C.

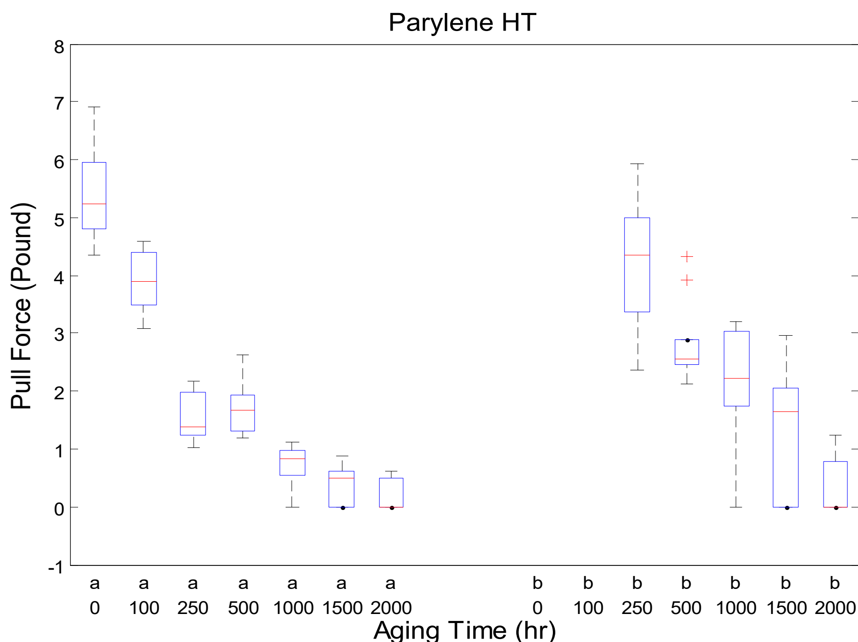


Figure 2.12 Pull Strength of Parylene HT on Electroplated Gold and AlN as a Function of Aging hour at 300°C (a) Electroplated Gold (b) AlN

## 2.6 FTIR Analysis for Parylene HT

Fourier-Transform Infrared Spectroscopy (FTIR) is widely used in organic synthesis, polymer science, and the pharmaceutical industry because it can analyze sample formations and degradation of chemical bonds [52]. In an FTIR spectroscopy, an infrared source emits different wavelength infrared radiation ranging from 4000 ~ 40 $cm^{-1}$. When exposed to infrared radiation, the sample molecules selectively absorb infrared radiation at certain wavelengths and pass through the others. The frequency of the absorption peak is determined by the vibrational energy gap which can be used to specify certain chemical bonds [52].

Figure 2.13 is the FTIR result of Parylene HT conducted by Special Coating System [48]. Figure 2.14 is the FTIR results of the as-built sample and the 1000 hours aged sample performed at Auburn University. The main absorptance peaks from 1500 $cm^{-1}$ to 500 $cm^{-1}$ in Figure 2.13

and Figure 2.14 for the as-built samples were similar as would be expected. The peaks around 1150 $cm^{-1}$ and 1260 $cm^{-1}$ correspond to C-F bonds [53]. There was not much difference between the as-built and the aged sample, which indicated the chemical bonds of Parylene HT was relatively stable during the aging test. The small peaks from 2000 $cm^{-1}$ to 2500 $cm^{-1}$ could be corresponded to the AlN substrate.

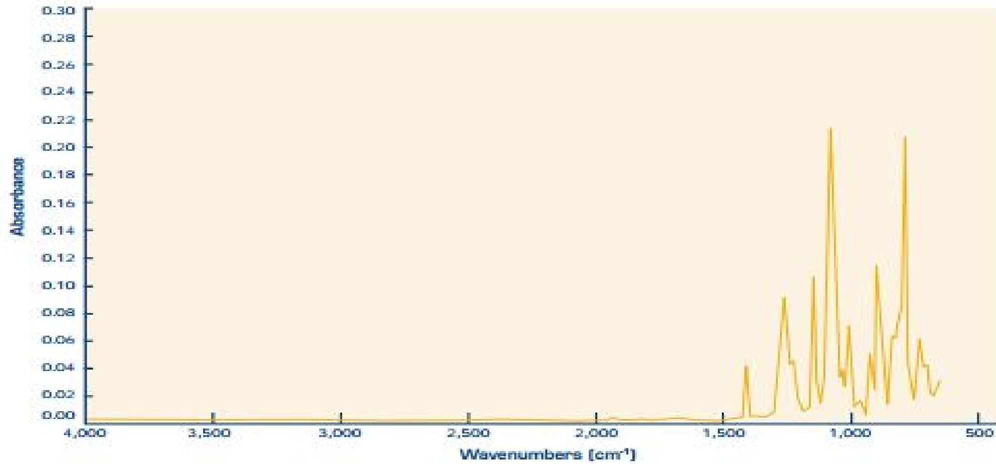


Figure 2.13 FTIR Result of Parylene HT by SCS [48]

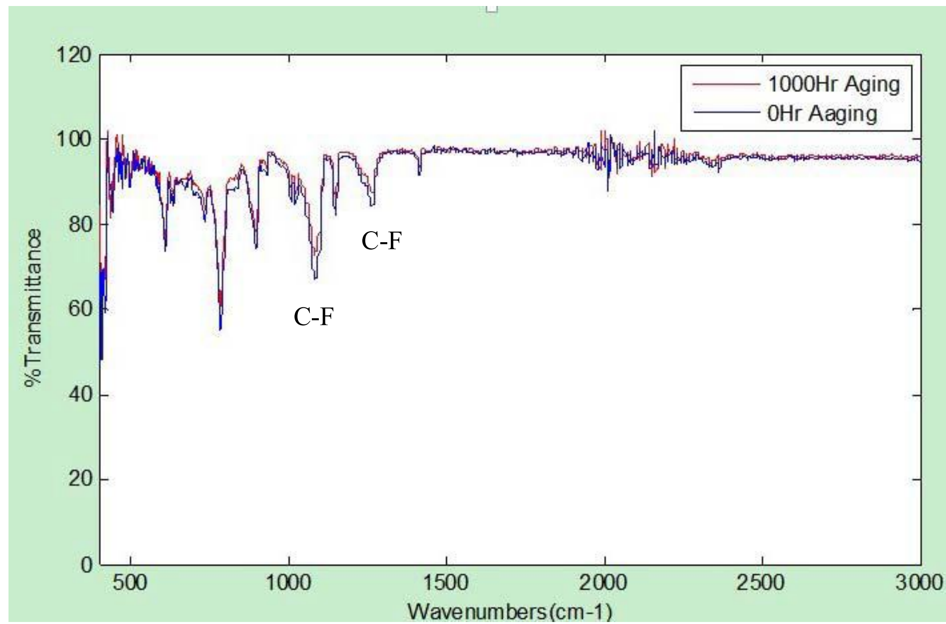


Figure 2.14 FTIR Result of Parylene HT

## 2.7 AFM Analysis for Parylene HT

Atomic Force Microscopy (AFM) is used for studying sample surface roughness at the nanoscale. The surface information is obtained with a mechanical probe by touching the sample surface, which can achieve more than 1000 times higher resolution than traditional optical microscopy [54]. Figure 2.15 and Figure 2.16 are the AFM three dimensional topography image of as-built and 1000 hours aged sample respectively. Table 2.5 shows the average roughness compare between the as-built and the 1000 hours aged sample. The average roughness after aging was 1.9 nm higher than the as-built sample. The increase was about 7%, which indicated the surface become only slightly rougher after aging.

Table 2.5 Parylene HT Roughness

| | As-Built | 1000 Hours Aaging |
|---|---|---|
| Roughness Average | 29.7 nm | 31.6 nm |
| Root Mean Square Roughness | 38.4 nm | 41.3 nm |

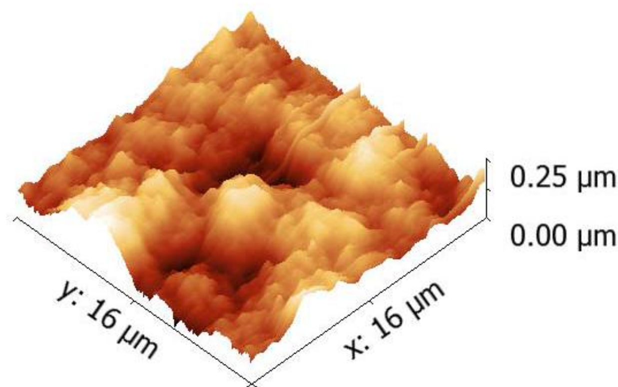


Figure 2.15 AFM 3-D Topography of Parylene HT on As-built Sample

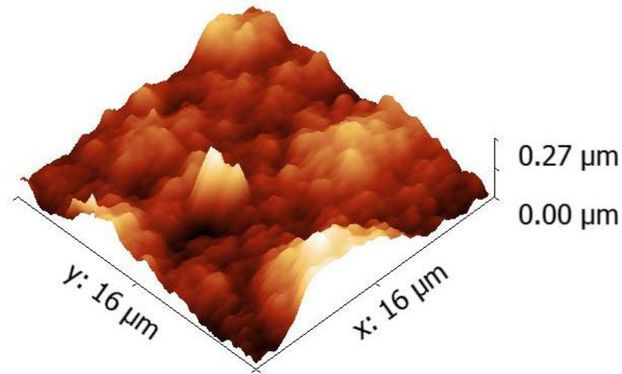


Figure 2.16 AFM 3-D Topography of Parylene HT on 1000 hours Aged Sample

**2.8 Summary**

Parylene HT and Duraseal 1531 were evaluated as electronic coatings for high temperature applications. Both of them provided high voltage insulation at 300$^{o}$C. However, Parylene HT cannot be used for 2000 hours application, as it lost adhesion to the substrate.

Parylene HT adhesion tests were performed on both electroplated gold and bare AlN substrates. A dramatic decrease in adhesion was observed with the increasing aging time.

FTIR and AFM results showed Parylene HT is a thermally stable material. The chemical bonds and roughness did not change much with the aging time. It is suspected the adhesion promoter used with Parylene HT decomposed at 300$^{o}$C. Further study is needed to improve Parylene HT adhesion strength and explore further applications for Duraseal 1531.

# CHAPTER 3 BIAGX ON NI PLATING

## 3.1 Introduction of BiAgX

BiAgX is a lead-free solder for high temperature applications. This solder was developed based on Bi-Ag alloys [55]. Binary Bi-Ag has a eutectic temperature of 262$^{o}$C (see Figure 3.1), which satisfied the requirement of die attach in high temperature (200$^{o}$C) environments. However, poor wetting and low ductility make Bi-Ag alloys less competitive when compare with other lead-free solders like Zn-Sn, Au-Sn and Zn-Al. Lalena, et al. [56] tried to dope a small amount of Ge in Bi-Ag11 alloy to improve the wetting performance, however, it did not work and even showed inferior wetting behavior. Meanwhile, Zhang, et al. [55] from Indium Corp. found with additive X, the Bi-Ag alloy showed better wetting on thick film and copper surfaces. X in BiAgX is Sn in the form of eutectic BiSn which has a eutectic temperature of 139$^{o}$C. During the reflow process, Bi-Sn melts earlier than the Bi-Ag alloy and forms intermetallics with metal surfaces like Ni and Cu. This kind of surface reaction can improve wetting performance dramatically. Besides, the shear strength result of BiAgX is comparable or even better than high lead solders like Pb5Sn2.5Ag, Pb10Sn and Pb2.5Ag [55].

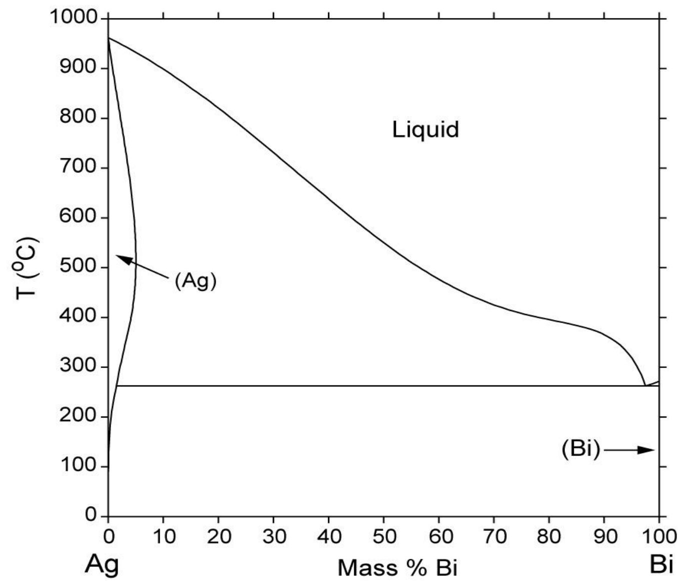


Figure 3.1 Ag-Bi Phase Diagram [57]

**3.2 Potential Intermetallic Formation**

The formation of brittle intermetallics during assembly or high temperature storage may reduce the solder joint reliability and cause failure. Shen, et al, have shown that the aged (200°C) die shear strength of SiC die assembled with BiAgX is higher on Cu with an Ag finish than on Cu with a Ni:B/Au finish [18, 58]. The Bi reacted with the Ni to form $NiBi_3$ intermetallic with high temperature aging. Cu does not form intermetallics with Bi. In this work, BiAgX die attach on different Ni platings was explored.

Figures 3.1, 3.2 and 3.3 are the phase diagrams of Bi-Ag, Bi-Cu, and Sn-Bi respectively. There are no intermetallic reactions in the Bi-Ag, Cu-Bi and Sn-Bi systems.

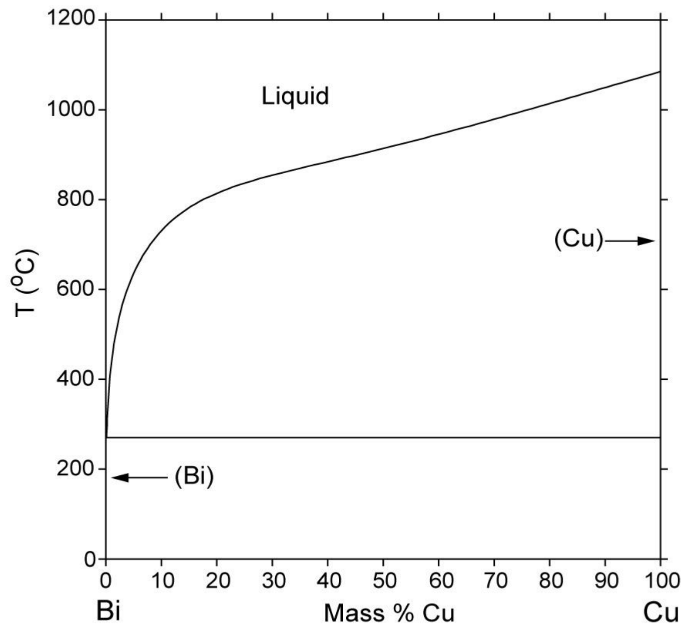


Figure 3.2 Bi-Cu Phase Diagram [59]

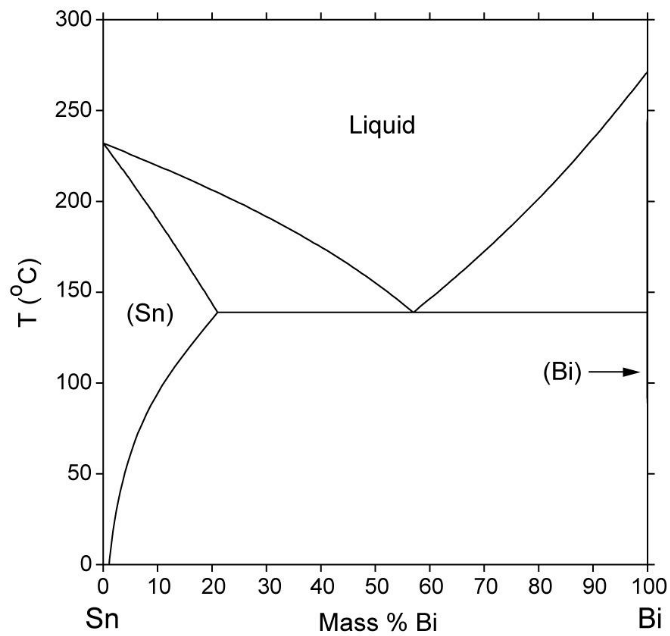


Figure 3.3 Bi-Sn Phase Diagram [60]

Figure 3.4 is the phase diagram of Ni-Bi. Theoretically, both $NiBi_3$ and NiBi would be found in Ni-Bi reactions. However, $NiBi_3$ is more commonly found. Lee et al. [61] reported reaction between Ni and liquid Bi at 300°C, 360°C, 420°C and 480°C, $NiBi_3$ was the only IMC

compound formed in the experiment. Also, Chachula, et al. [62] reported the formation of $NiBi_3$ when studying the interaction of BiAg11 solder with Ni substrates. Sn as the low melting temperature addictive in BiAgX, reacted with the surface finish metal Ni. Figure 3.5 shows the possible IMC formation of $Ni_xSn_y$.

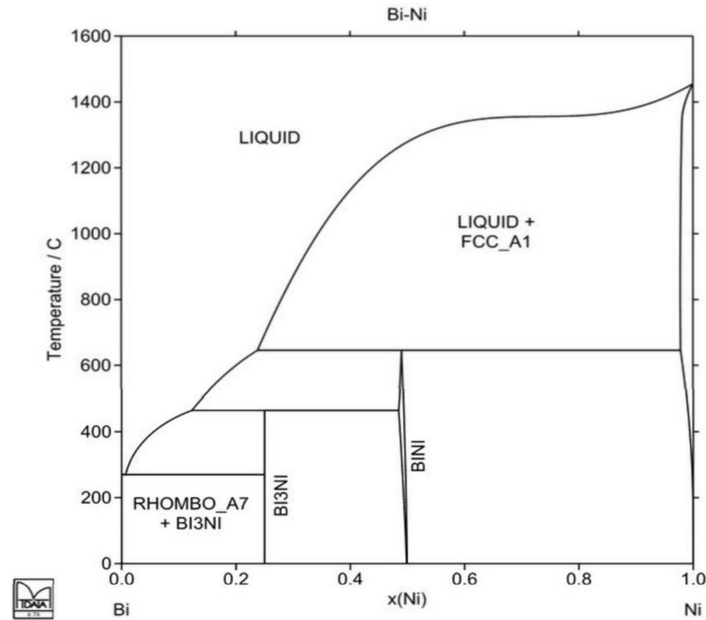


Figure 3.4 Bi-Ni Phase Diagram [63]

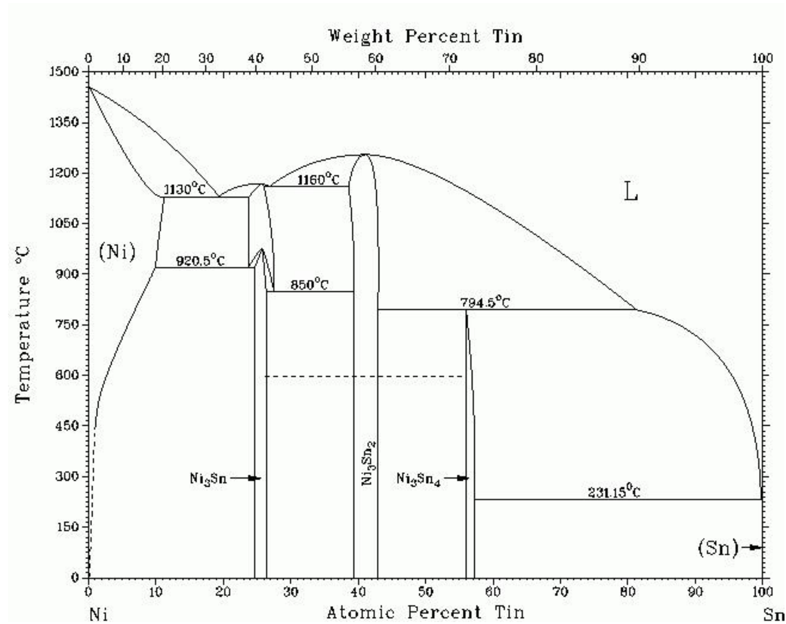


Figure 3.5 Ni-Sn Phase Diagram [64]

## 3.3 Assembly

### 3.3.1 Die

The die for the BiAgX die attach studies were fabricated from 0.38mm thick SiC wafers with deposited Ti/Ni/Ag (50nm/200nm/50nm) metallization in a CHA Industries MARK-50 metal deposition system. After thin film deposition, the wafers were diced into 2 mm × 2 mm and 5 mm × 5 mm for the thermal cycle test.

### 3.3.2 Substrate

The substrates were 96% aluminum oxide direct bond copper (DBC) from Stellar Industries (Millbury, MA, USA). The size of the DBC was 19.05 cm × 13.716 cm. The thickness of the $Al_2O_3$ was 0.635 mm and copper was 0.2032 mm thick. The copper thickness for the thermal cycling test was 0.127mm since thick copper may cause more rapid failure due to the CTE mismatch.

### 3.3.3 Finishes

For the BiAgX studies, the DBC Cu was plated with a 1.8 µm Ni layer and a 0.17 µm Au layer except for the Ni:Co samples, which were not Au plated. The Ni plating compositions are shown in Table 3.1.

Table 3.1 Nickel Composition as Provided by the Plating Suppliers

| Plating | Ni Percentage (at.%) |
|---|---|
| Ni:P - electroless | 80%~85% |
| Ni:P - electroplated | 80%~85% |
| Pure Ni - electroplated | 100% |
| Ni:Co - electroplated | 95%~97% |

3.3.4 Assembly Process

The BiAgX solder paste was printed on the DBC substrate with a 0.127 mm thick stainless steel stencil. Then, a Palomar Model 3500 automated die placement machine was used for die placement. The solder reflow was performed in a pure nitrogen environment using a PEO 601 furnace. A 3 minute ramp from room temperature to 321°C was used. A thermocouple was attached to the DBC substrate with Kapton tape and the measured profile is plotted in Figure 3.6.

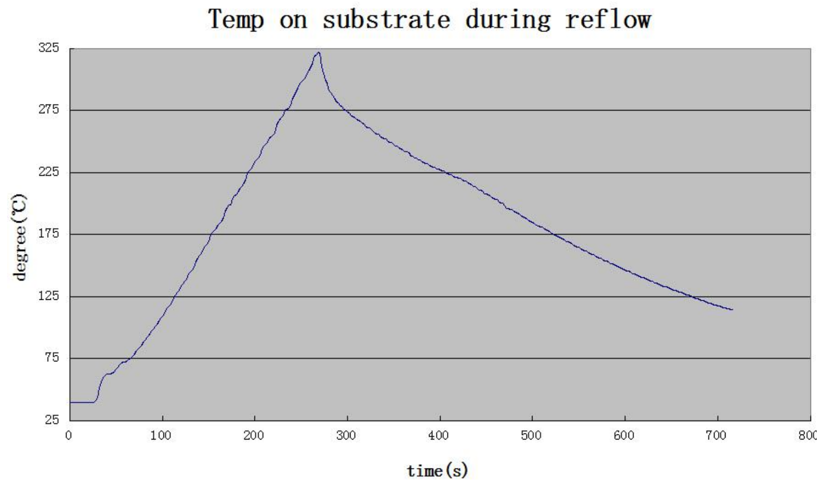


Figure 3.6 Reflow Profile

**3.4 Initial Shear Data**

The die shear strength was measured with a Dage PC2400 using a 100kg shear module. Test height was set to 2.54 µm and test speed was 50.8 µm/s. The BiAgX samples had an average shear strength of 4.8 kg/mm$^2$ (Table 3.2) for all Ni finishes.

Table 3.2 BiAgX Initial Average Shear Strength

| Plating | Initial Average Shear Data (kg/mm$^2$) |
| --- | --- |
| Pure Ni - electroplated | 4.84 |
| Ni:P - electroplated | 4.83 |
| Ni:P - electroless | 4.80 |
| Ni:Co - electrolplated | 4.80 |

3.4.1 Cross Section & Fracture Analysis

Figure 3.7 shows a SEM cross section of an as-built BiAgX sample with electroplated Ni:P. In the solder region of the die attach, the ζ-phase $(AgAu)_{0.86}Sn_{0.14}$ was found in a Bi matrix. The ζ-phase contains Sn in the range from 11.8 at.% to 18 at.% Sn at 200°C. The ζ-phase was observed in all samples (Figures 3.8-3.10). In the Ni:Co samples, the ζ-phase did not contain Au, since the substrates were not Au plated (Figure 3.11). The EDS spot size did not allow exact determination of the Ni-Sn intermetallic composition as Bi was always included. The Ni-Sn intermetallic had less protrusions into the Bi solder for electrolytic pure Ni and Ni:P (Figures 3.8-3.9), compared to electroless Ni:P and electrolytic Ni:Co platings (Figures 3.10-3.11).

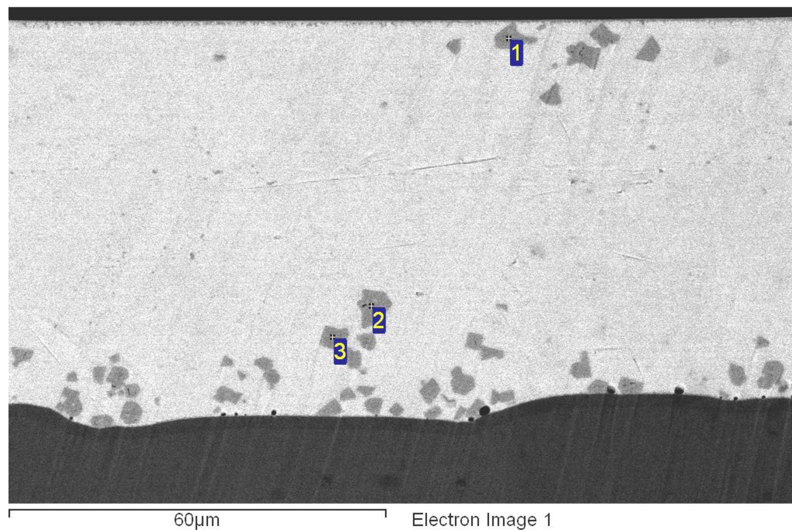


| Locations | Ag | Sn | Au |
|---|---|---|---|
| 1 | 78.2 | 14.2 | 7.6 |
| 2 | 77.9 | 14.0 | 8.1 |
| 3 | 80.6 | 14.0 | 5.4 |

Figure 3.7 As-built BiAgX on Electrolytic Ni:P Cross Section and Elemental Analysis (at.%)

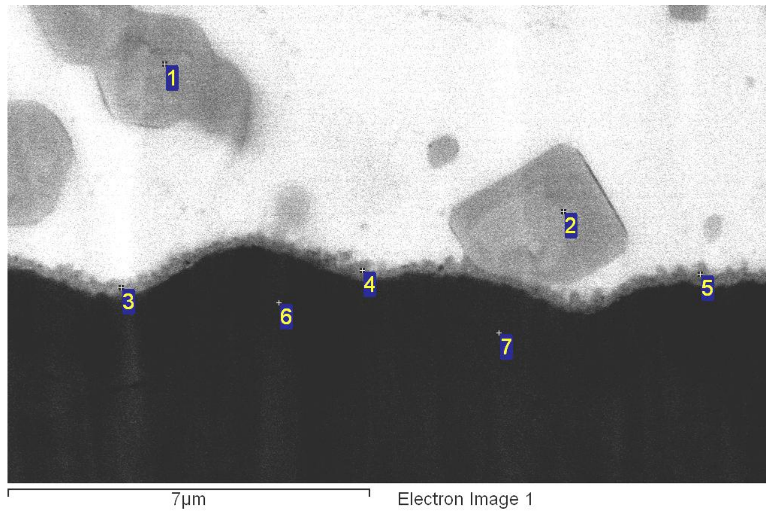


| Locations | Ni | Ag | Sn | Bi | Au |
|---|---|---|---|---|---|
| 1 | 0.0 | 75.8 | 16.0 | 0.0 | 8.2 |
| 2 | 0.0 | 70.5 | 17.9 | 0.0 | 11.6 |
| 3 | 55.1 | 0.0 | 19.3 | 25.6 | 0.0 |
| 4 | 63.1 | 0.0 | 24.1 | 12.8 | 0.0 |
| 5 | 52.6 | 0.0 | 18.7 | 28.7 | 0.0 |
| 6 | 100.00 | 0.0 | 0.0 | 0.0 | 0.0 |
| 7 | 100.00 | 0.0 | 0.0 | 0.0 | 0.0 |

Figure 3.8 As-built BiAgX on Electrolytic Ni Cross Section and Elemental Anaylsis (at.%)

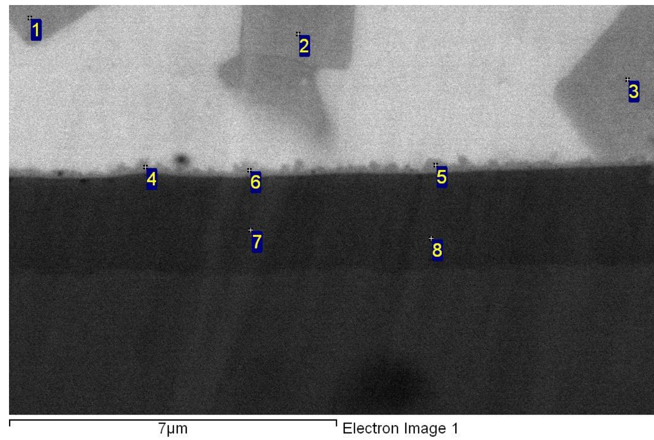


| Location | Ni | Ag | Sn | Bi | P | Au |
|---|---|---|---|---|---|---|
| 1 | 0.0 | 80.0 | 14.0 | 0.0 | 0.0 | 6.0 |
| 2 | 0.0 | 79.0 | 14.4 | 0.0 | 0.0 | 6.6 |
| 3 | 0.0 | 79.6 | 13.7 | 0.0 | 0.0 | 6.7 |
| 4 | 41.7 | 0.0 | 25.5 | 32.8 | 0.0 | 0.0 |
| 5 | 47.7 | 0.0 | 32.1 | 24.2 | 0.0 | 0.0 |
| 6 | 46.1 | 0.0 | 23.7 | 30.2 | 0.0 | 0.0 |
| 7 | 82.1 | 0.0 | 0.0 | 0.0 | 17.9 | 0.0 |
| 8 | 82.9 | 0.0 | 0.0 | 0.0 | 17.1 | 0.0 |

Figure 3.9 As-built BiAgX on Electrolytic Ni:P Cross Section and Elemental Analysis (at.%)

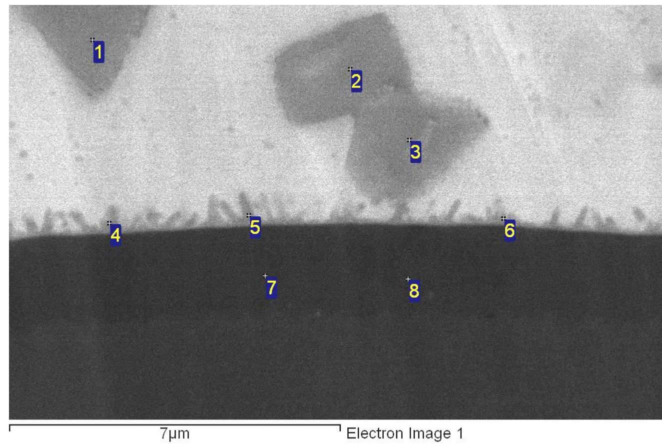


| Location | Ni | Ag | Sn | Bi | P | Au |
|---|---|---|---|---|---|---|
| 1 | 0.0 | 77.4 | 15.0 | 0.0 | 0.0 | 7.6 |
| 2 | 0.0 | 78.8 | 14.8 | 0.0 | 0.0 | 6.4 |
| 3 | 0.0 | 75.9 | 15.8 | 0.0 | 0.0 | 8.3 |
| 4 | 48.7 | 0.0 | 31.0 | 20.3 | 0.0 | 0.0 |
| 5 | 43.3 | 0.0 | 30.5 | 26.2 | 0.0 | 0.0 |
| 6 | 44.6 | 0.0 | 30.3 | 25.1 | 0.0 | 0.0 |
| 7 | 81.6 | 0.0 | 0.0 | 0.0 | 18.4 | 0.0 |
| 8 | 82.1 | 0.0 | 0.0 | 0.0 | 17.9 | 0.0 |

Figure 3.10 As-built BiAgX on Electroless Ni:P Cross Section and Elemental Analysis (at.%)

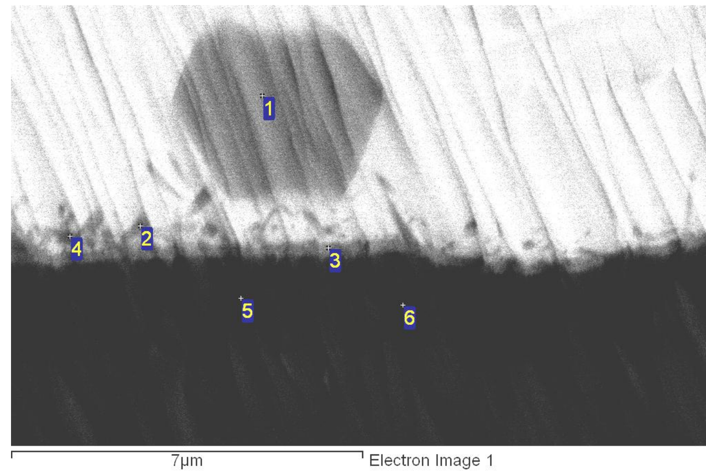


| Location | Ni | Ag | Sn | Bi | Co |
|---|---|---|---|---|---|
| 1 | 0.0 | 86.6 | 13.4 | 0.0 | 0.0 |
| 2 | 34.8 | 0.0 | 29.3 | 35.9 | 0.0 |
| 3 | 42.5 | 0.0 | 33.1 | 24.4 | 0.0 |
| 4 | 42.9 | 0.0 | 31.9 | 25.2 | 0.0 |
| 5 | 94.5 | 0.0 | 0.0 | 0.0 | 5.5 |
| 6 | 94.5 | 0.0 | 0.0 | 0.0 | 5.5 |

Figure 3.11 As-built BiAgX on Electrolytic Ni:Co Cross Section and Elemental Analysis (at.%)

Fracture surfaces were examined after die shear. The fracture surfaces for the electrolytic Ni:P are shown in Figure 3.12. Based on the fracture surface analysis and the cross sections, failure occurred in the solder near the Ni-Sn intermetallic layer (Ni, Ag, Sn, Bi on the substrate side and Bi and Ag on the die side). No P was detected on the substrate side, since P was pushed ahead of the Ni-Sn IMC. The electroless Ni:P also had Bi and Ag on the die side and Ni, Ag, Sn and Bi on the substrate side. The electrolytic Ni and electrolytic Ni:Co failed in approximately the same region with both having Bi, Ag and Sn on the die side and Ni, Ag, Sn and Bi on the substrate side. Similar failure locations are consistently with nearly identical initial shear strengths for the different Ni finishes.

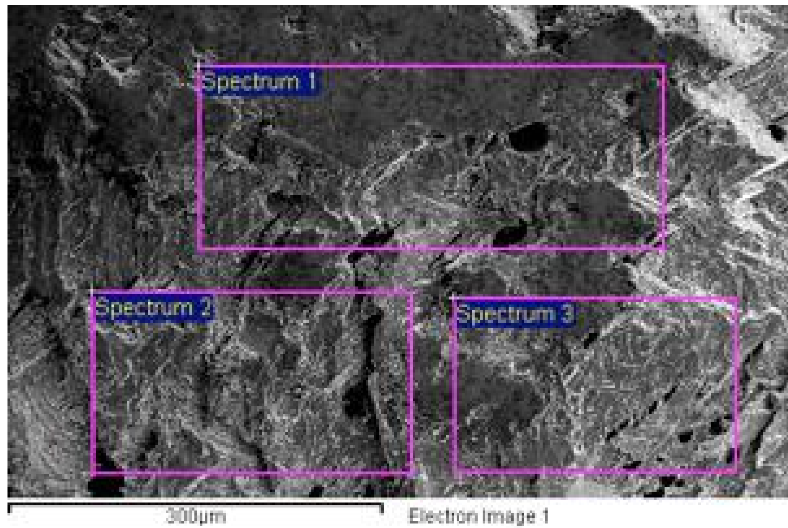


| Location | Bi | Ag |
|---|---|---|
| 1 | 100 | 0 |
| 2 | 94.3 | 5.7 |
| 3 | 95.7 | 4.3 |

(a) Die Side

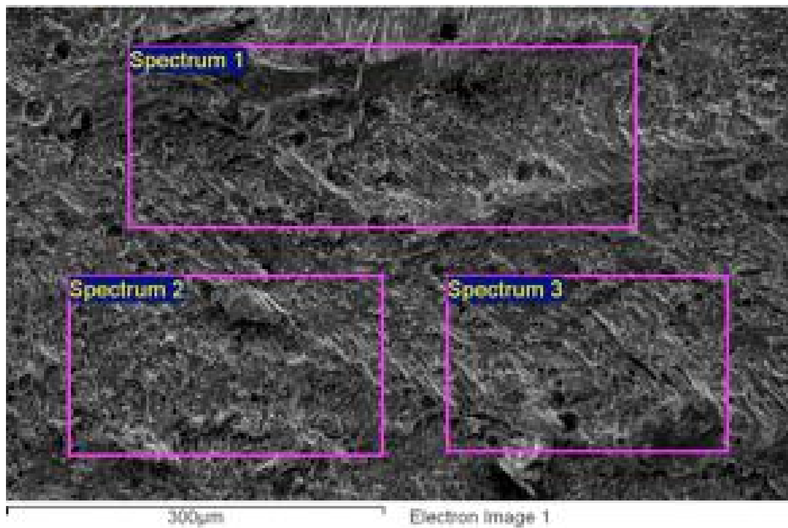


| Location | Ni | Ag | Sn | Bi |
|---|---|---|---|---|
| 1 | 13.1 | 7.1 | 5.4 | 74.4 |
| 2 | 12.0 | 6.1 | 8.6 | 73.3 |
| 3 | 12.4 | 5.9 | 6.9 | 74.8 |

(b) Substrate Side

Figure 3.12. As-built BiAgX on Electrolytic Ni:P Fracture Surfaces after Die Shear (at.%)

### 3.5 Aging Test

The BiAgX samples with 2 mm x 2 mm SiC die were aging at 200°C in air. Samples were removed for shear testing at specified time intervals. The die shear results are plotted in Figure 3.13. There was a significant decrease in shear strength during the first 1500 hours for both the electroless Ni:P and the electrolytic Ni. The average shear strength dropped to approximately 3kg/mm$^2$ and was relatively stable through 3000hr. This was similar to the results with electroless Ni:B in [59, 60]. The electroplated Ni:P samples showed less degradation. After a decrease in the shear strength during the first 500 hours, the shear strength of the electroplated Ni:P was stable with an average shear strength of 3.8 kg/mm$^2$. The electrolytic Ni:Co had a comparable decrease in die shear strength during the first 500 hours at 200°C. The shear strength decreased to about 2 kg/mm$^2$ after 1500 hours aging.

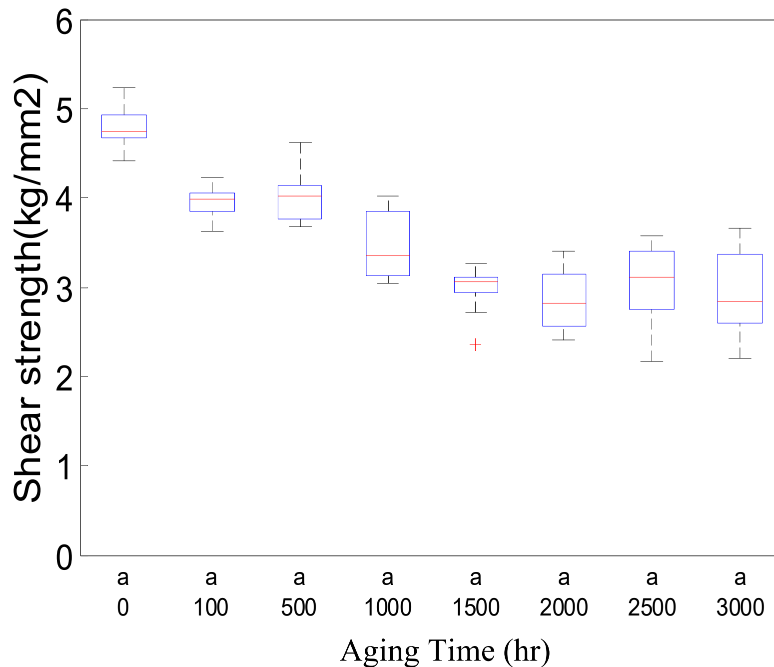


(a) Electroless Ni:P

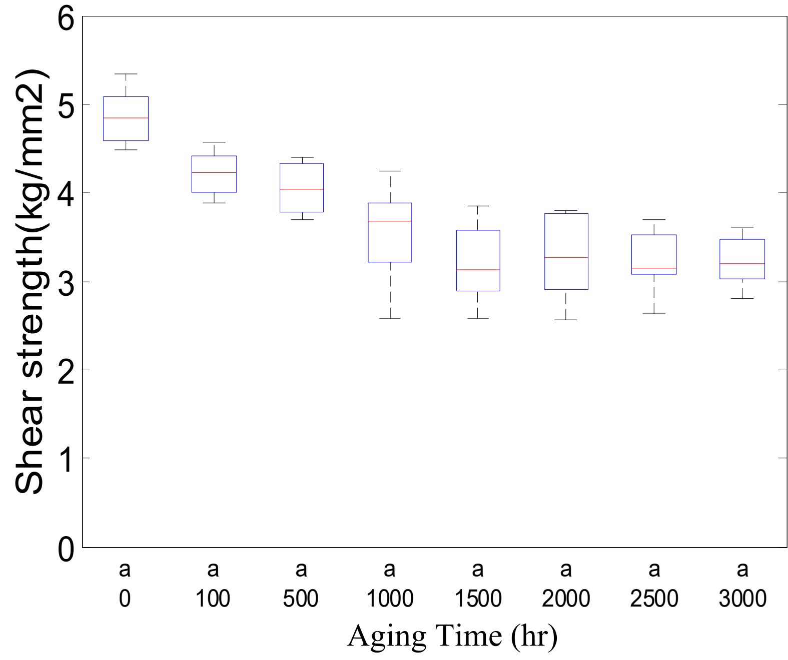


(b) Electrolytic Ni

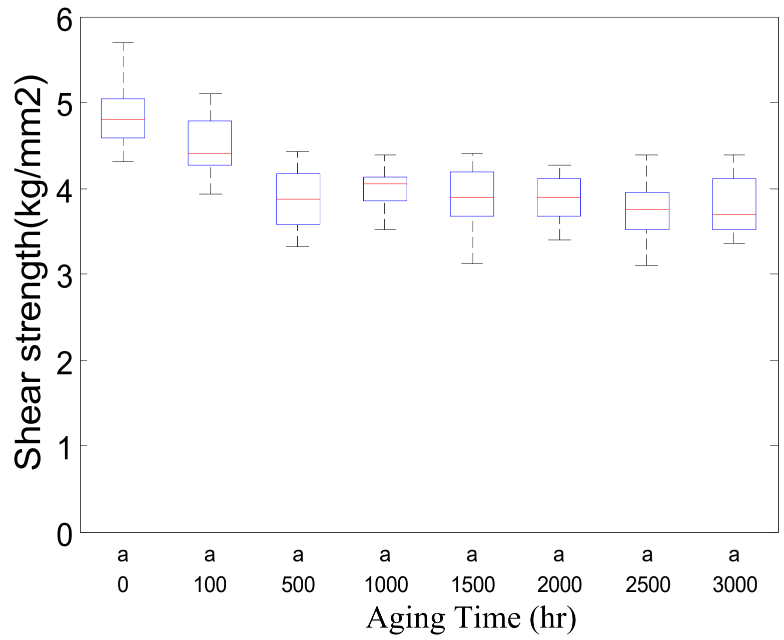


(c) Electrolytic Ni:P

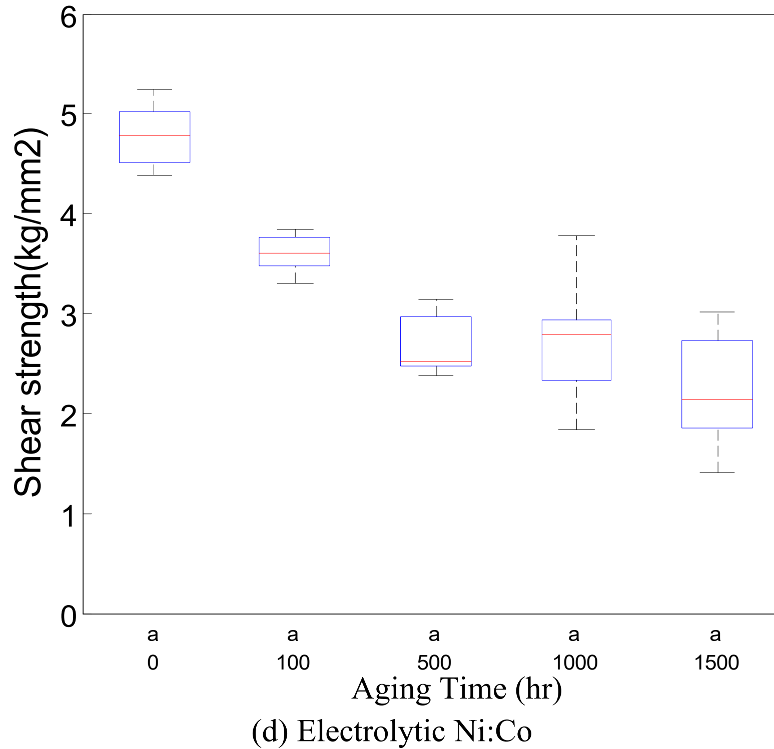

(d) Electrolytic Ni:Co

Figure 3.13 Die Shear Data for BiAgX as a Function of Storage Time at 200ºC. (a) Electroless Ni:P, (b) Electroplated Ni, (c) Electroplated Ni:P, and (d) Electrolytic Ni:Co.

3.5.1 Cross Section and Fracture Analysis

Figure 3.14 is a cross section of the BiAgX die attach on the electrolytic Ni substrate after 16 hours aging at 200ºC. Figure 3.15 is the corresponding element analysis at higher magnification. The EDS results revealed the $NiBi_3$ was first formed after the Ni-Sn IMC lifting from the Ni surface. This $NiBi_3$ bulk was randomly distributed along the Ni to Bi interface. ζ-phase $(AgAu)_{0.86}Sn_{0.14}$ was also detected.

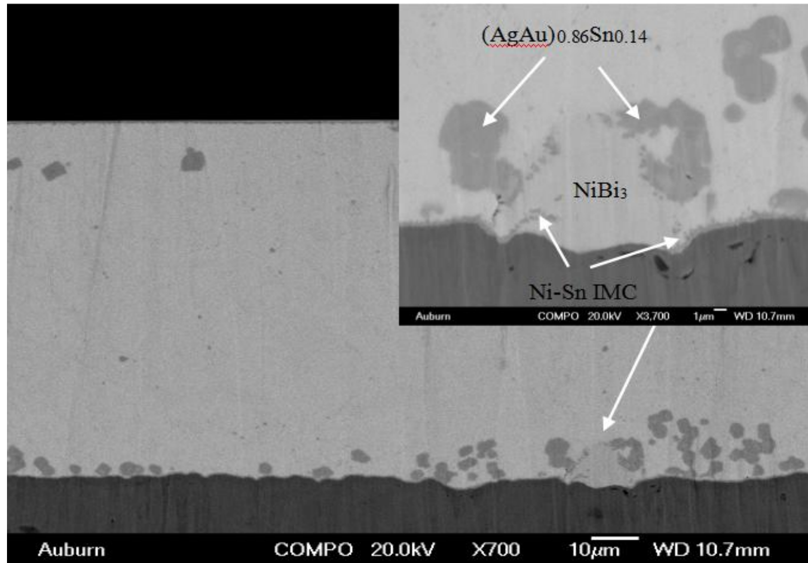


Figure 3.14 Cross Section of BiAgX on Electrolytic Ni Aging after 16 hours at 200°C

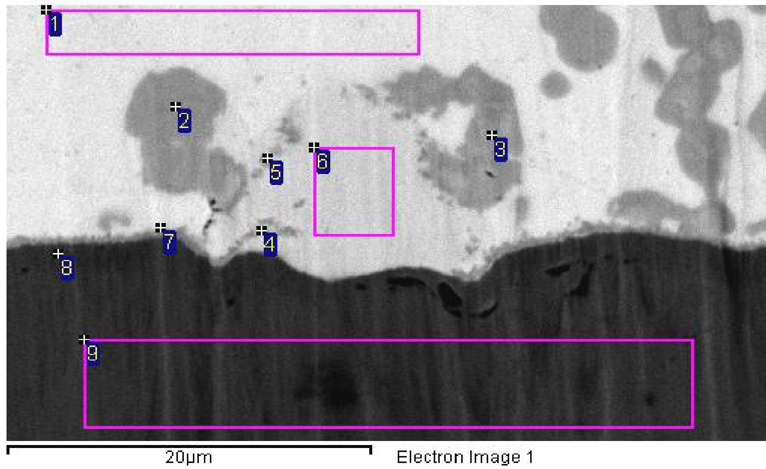


| Location | Ni | Bi | Ag | Sn | Au | Cu |
|---|---|---|---|---|---|---|
| 1 | | 100.0 | | | | |
| 2 | | | 78.5 | 14.1 | 7.4 | |
| 3 | | | 78.8 | 13.6 | 7.6 | |
| 4 | 31.1 | 57.9 | | 11.0 | | |
| 5 | 41.4 | 32.4 | | 26.2 | | |
| 6 | 24.5 | 75.5 | | | | |
| 7 | 35.3 | 47.6 | | 17.1 | | |
| 8 | 100.0 | | | | | |
| 9 | | | | | | 100.0 |

Figure 3.15 Cross Section and Element Analysis of the BiAgX Die Attach on Electrolytic Ni after 16 hours at 200°C

Figure 3.16 and Figure 3.17 are cross sections of the BiAgX die attach on the electrolytic Ni substrate after 144 hours and 500 hours aging at 200°C respectively. In Figure 3.16, the $NiBi_3$ layer became thicker and the area was larger compared to the 16 hours aging sample. A clear Ni layer was observed where no $NiBi_3$ was formed. After 500 hours aging, a uniform $NiBi_3$ layer was formed (see Figure 3.17).

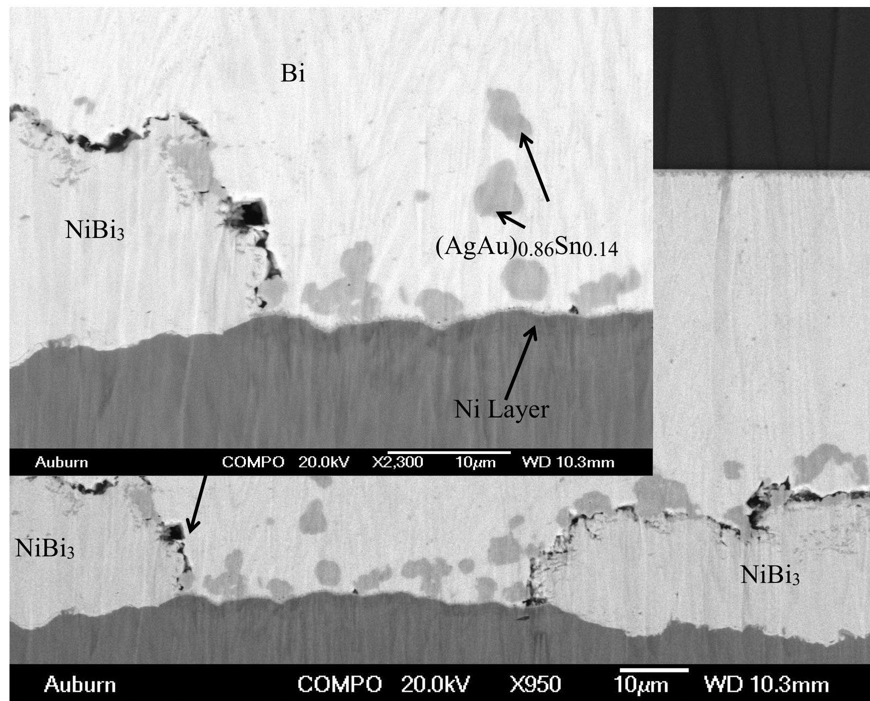


Figure 3.16 Cross Section of BiAgX on Electrolytic Ni Aging after 144 hours at 200°C

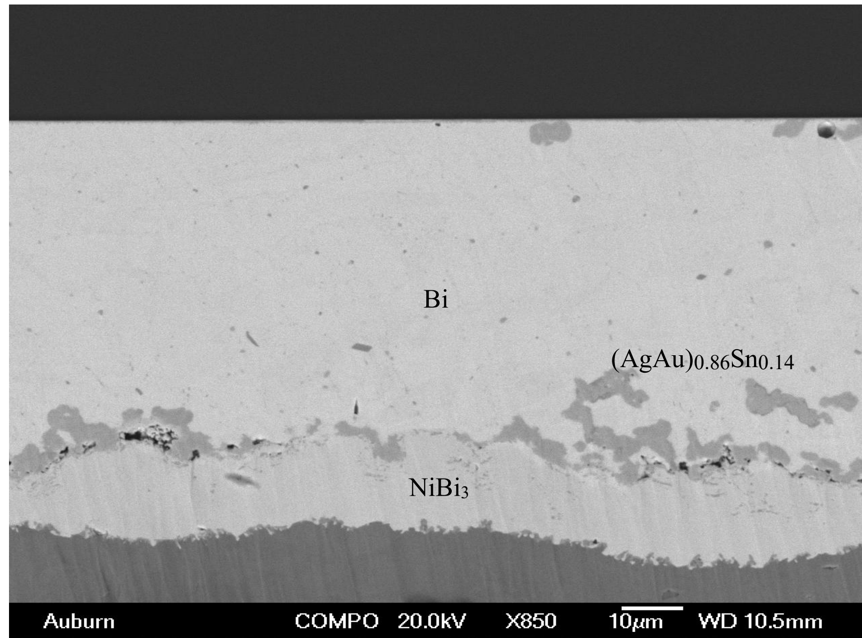


Figure 3.17 Cross Section of BiAgX on Electrolytic Ni Aging after 500 hours at 200°C

3.5.1.1 Electroless Ni:P

Figure 3.18 is a cross section of the electroless Ni:P after 500 hours aging at 200°C. The Ni:P layer has started to spall from the Cu. After 3000 hours, it has completely spalled (Figure 3.19). Figure 3.20 is a higher magnification image and elemental analysis of the spalled region after 3000 hours. $NiBi_3$ has formed on both sides of the Ni:P layer. From the elemental analysis of the 3000 hours aged die sheared fracture surfaces (Figure 3.21), the failure occurs near the spalled Ni:P-to-$NiBi_3$ and Ni-Sn intermetallic interface along the top side of the Ni:P layer.

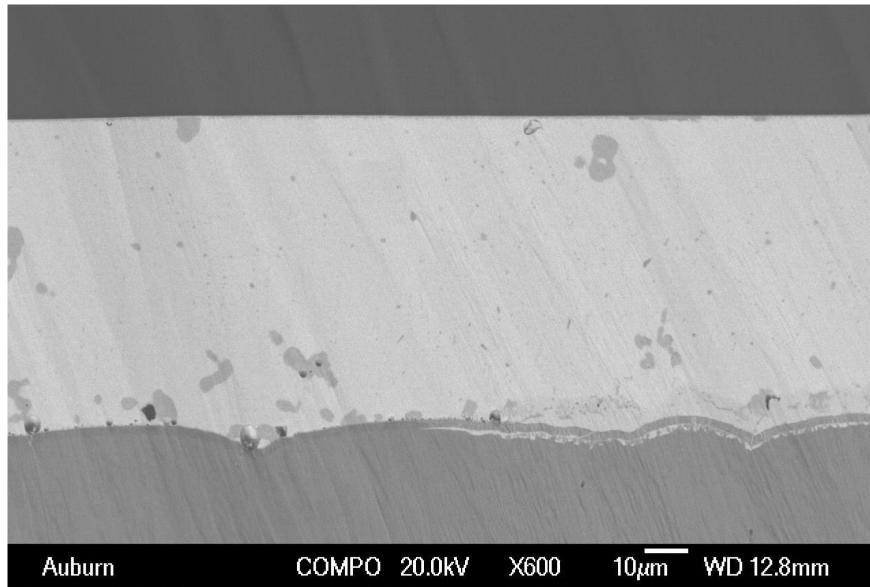


Figure 3.18 Cross Section of the BiAgX Die Attach on Electroless Ni:P after 500 hours at 200$^{o}$C

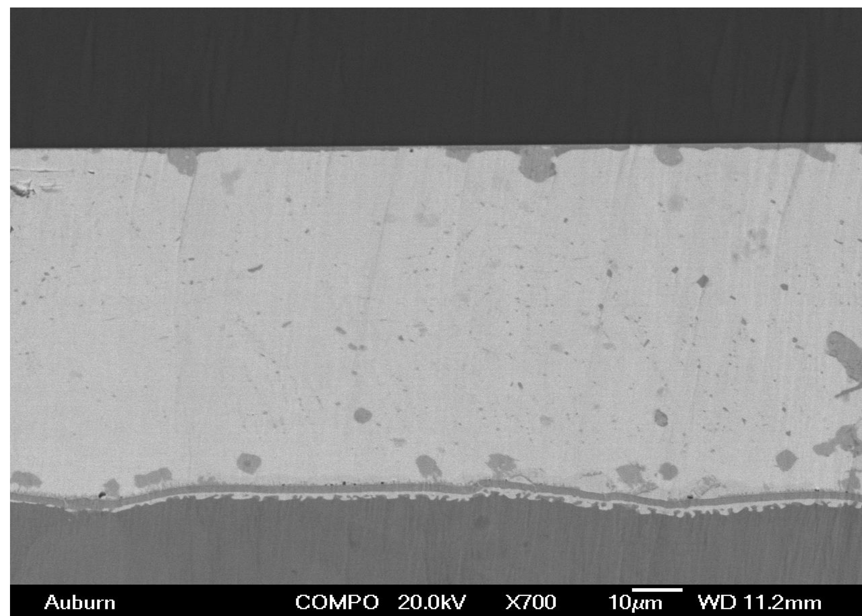


Figure 3.19 Cross Section of the BiAgX Die Attach on Electroless Ni:P after 3000 hours at 200$^{o}$C

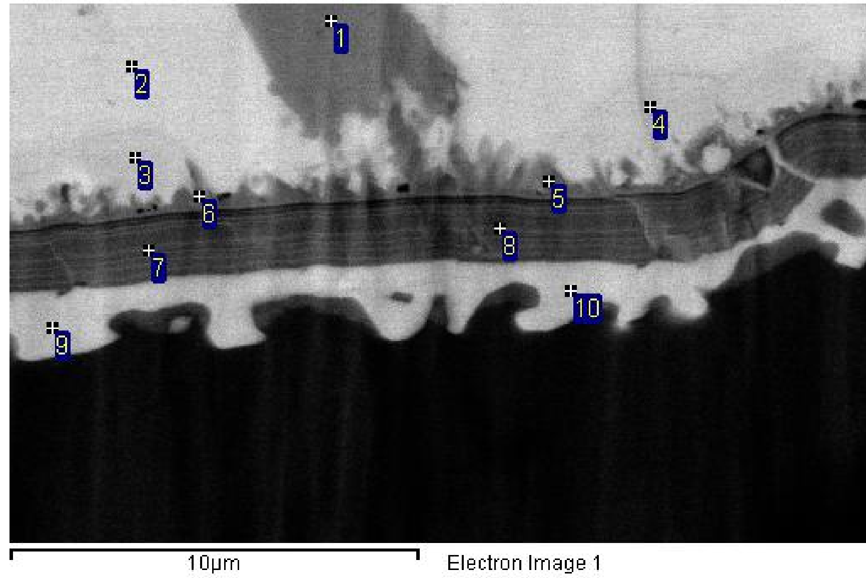


| Location | P | Ni | Au | Ag | Sn | Bi |
|---|---|---|---|---|---|---|
| 1 | 0.0 | 0.0 | 5.4 | 91.1 | 3.5 | 0.0 |
| 2 | 0.0 | 0.0 | 0.0 | 0.0 | 0.0 | 100.0 |
| 3 | 0.0 | 22.5 | 0.0 | 0.0 | 0.0 | 77.5 |
| 4 | 0.0 | 22.2 | 0.0 | 0.0 | 0.0 | 77.8 |
| 5 | 0.0 | 35.7 | 0.0 | 0.0 | 48.1 | 16.2 |
| 6 | 0.0 | 40.8 | 0.0 | 0.0 | 41.7 | 17.5 |
| 7 | 32.3 | 67.7 | 0.0 | 0.0 | 0.0 | 0.0 |
| 8 | 33.1 | 66.9 | 0.0 | 0.0 | 0.0 | 0.0 |
| 9 | 0.0 | 23.6 | 0.0 | 0.0 | 0.0 | 76.4 |
| 10 | 0.0 | 24.6 | 0.0 | 0.0 | 0.0 | 75.4 |

Figure 3.20 BiAgX on Electroless Ni:P Cross Section and Elemental Analysis after 3000 hours at 200°C (at.%)

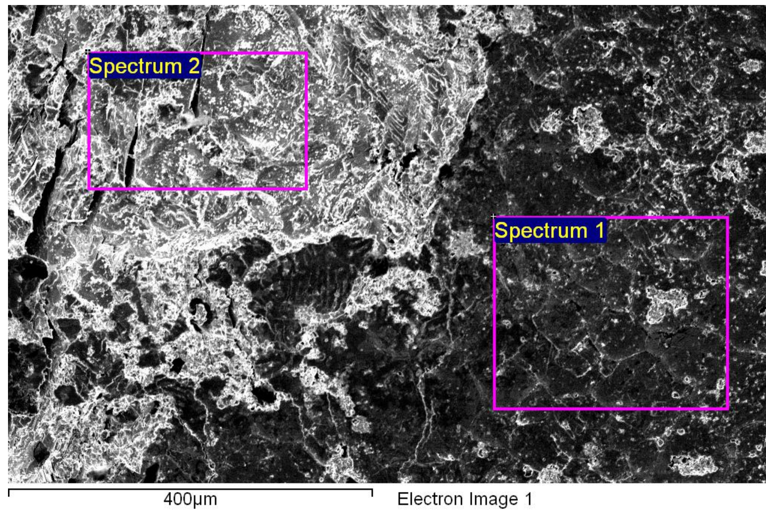


(a) Die Side

| Location | Ni | Sn | Bi |
|---|---|---|---|
| 1 | 30.0 | | 69.7 |
| 2 | 14.3 | 12.4 | 73.3 |

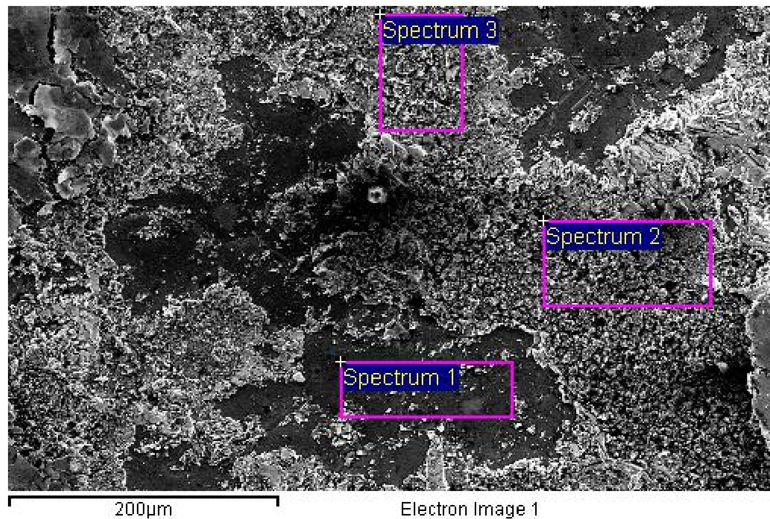


(b) Substrate Side

| Location | P | Ni | Ag | Sn | Au | Bi |
|---|---|---|---|---|---|---|
| 1 | 23.6 | 66.0 | | | | 10.4 |
| 2 | | 21.0 | 11.8 | 13.0 | 1.5 | 52.7 |
| 3 | | 20.4 | 17.3 | 17.1 | 1.0 | 44.2 |

Figure 3.21 Die Shear Fracture Surfaces of BiAgX on Electroless Ni:P Sample Aged for 3000 hours at 200°C (at.%)

3.5.1.2 Electrolytic Ni

Figure 3.22 is a cross section of the BiAgX die attach on electrolytic Ni after 3000 hours at 200°C. A thick layer of $NiBi_3$ intermetallic has formed and the Ni has been consumed. The Sn content in the (AgAu)-Sn IMC had decreased from 14% to 0~5%. Figure 3.23 is a cross section at the higher magnification close to the die side. Location 1 contained Cu, Ni, and Sn and is (CuNi)-Sn intermetallic. Compare to the result in location 2 that correspond to Ni-Sn IMC in Bi matrix. Location 1 should be the some Ni-Sn IMC on the die side. Locations 3 and 5 were primarily Ag with 5%~6% Au dissolved in it. Location 4 was Cu-Sn IMC with 2% Au. Figure 3.24 is a cross section at the higher magnification close to the substrate side. Locations 6 and 7 corresponded to Ni-Sn IMC. Locations 8 and 9 were copper with 11%~10% Au dissolved in it.

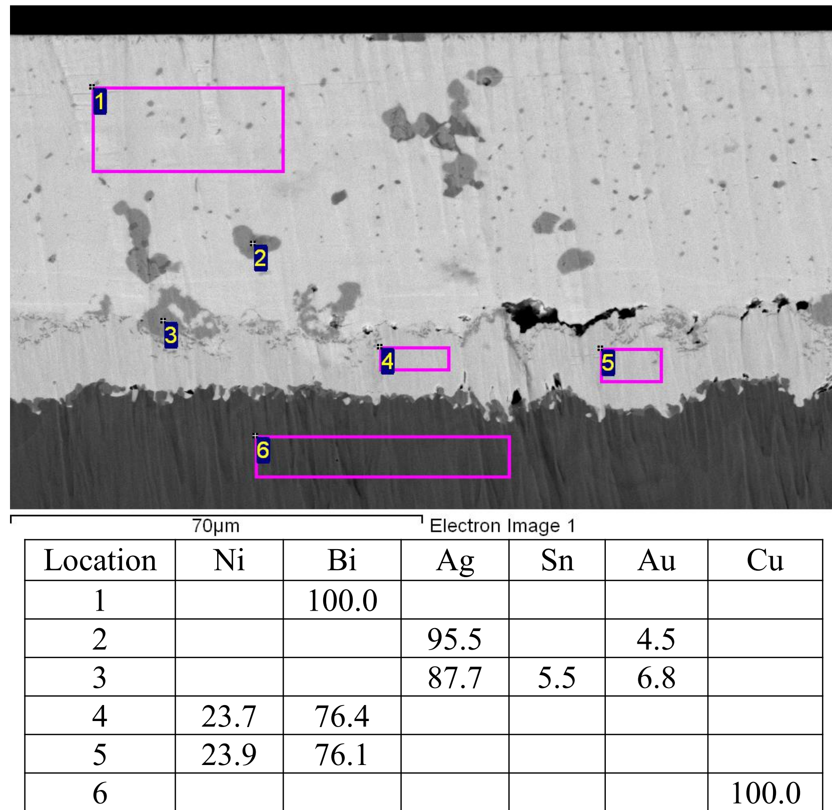


| Location | Ni | Bi | Ag | Sn | Au | Cu |
|---|---|---|---|---|---|---|
| 1 | | 100.0 | | | | |
| 2 | | | 95.5 | | 4.5 | |
| 3 | | | 87.7 | 5.5 | 6.8 | |
| 4 | 23.7 | 76.4 | | | | |
| 5 | 23.9 | 76.1 | | | | |
| 6 | | | | | | 100.0 |

Figure 3.22 Cross Section of BiAgX on Electrolytic Ni 3000 hours Aging at 200°C (at.%)

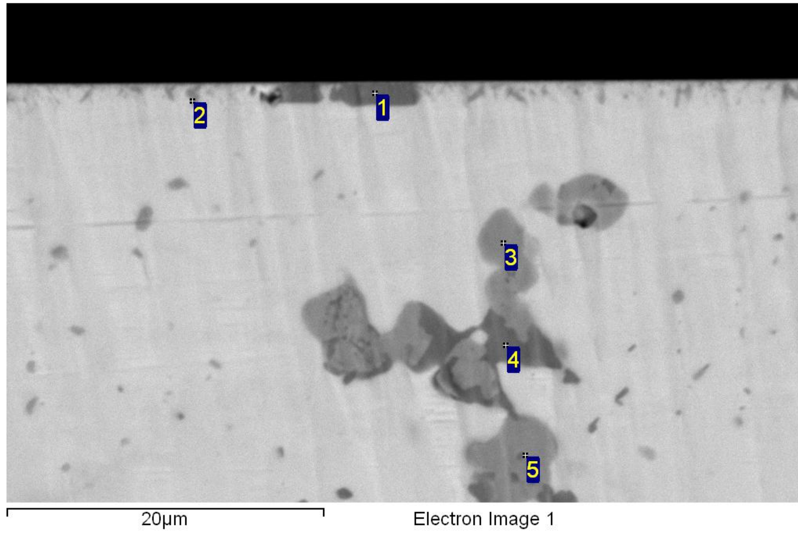


| Location | Ni | Bi | Ag | Sn | Au | Cu |
|---|---|---|---|---|---|---|
| 1 | 13.7 | | | 23.9 | | 62.4 |
| 2 | 43.6 | 19.2 | | 37.2 | | |
| 3 | | | 93.8 | | 6.3 | |
| 4 | | | | 15.6 | 2.6 | 81.8 |
| 5 | | | 94.4 | | 5.6 | |

Figure 3.23 Cross Section of BiAgX on Electrolytic Ni 3000 hours Aging at 200$^{o}$C in High Magnification Close to the Die Side (at.%)

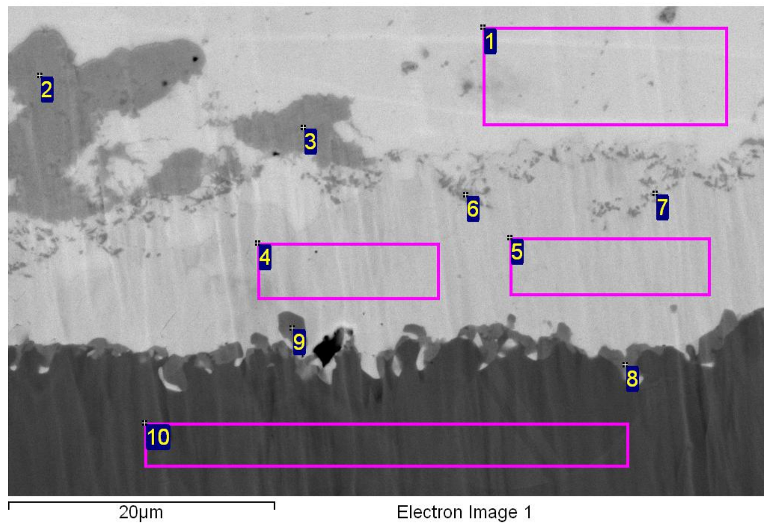


| Location | Ni | Bi | Ag | Sn | Au | Cu |
|---|---|---|---|---|---|---|
| 1 | | 100.0 | | | | |
| 2 | | | 96.4 | | 3.6 | |
| 3 | | | 95.9 | | 4.1 | |
| 4 | 23.7 | 76.4 | | | | |
| 5 | 23.7 | 76.3 | | | | |
| 6 | 36.0 | 42.9 | | 21.1 | | |
| 7 | 32.9 | 49.9 | | 17.3 | | |
| 8 | | | | | 12.5 | 87.5 |
| 9 | | | | | 11.4 | 88.6 |
| 10 | | | | | | 100.0 |

Figure 3.24 Cross Section of BiAgX on Electrolytic Ni 3000 hours Aging at 200°C in High Magnification Close to the Die Side (at.%)

The examination of the fracture surfaces after die shear of 3000 hours aged samples revealed Ni, Ag, Sn, and Bi on both the substrate and die fracture surfaces (see Figure 3.25). Au was only found on the substrate side. The amount of Au on the die side may be too small to be detected. The Ni-to-Bi ratio on the substrate side corresponded to $NiBi_3$. From the cross section, the fracture surface was along the $NiBi_3$ to Bi interface with Ag(Au)-Sn and Ni-Sn randomly distributed.

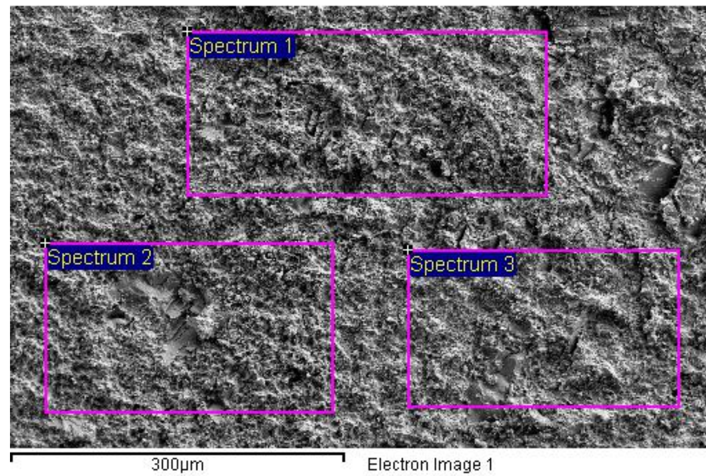


(a) Die Side

| Location | Ni | Bi | Ag | Sn |
|---|---|---|---|---|
| 1 | 11.2 | 74.0 | 5.3 | 9.5 |
| 2 | 3.9 | 88.0 | 3.5 | 4.6 |
| 3 | 4.1 | 90.4 | 2.7 | 2.8 |

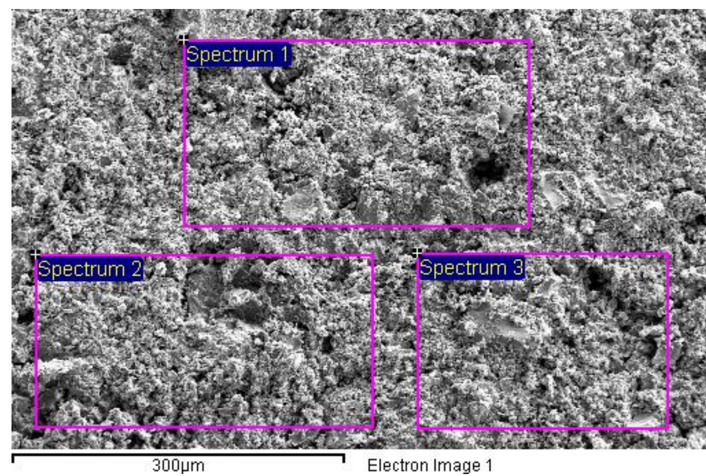


(b) Substrate Side

| Location | Ni | Bi | Ag | Sn | Au |
|---|---|---|---|---|---|
| 1 | 20.0 | 63.3 | 7.9 | 7.1 | 1.8 |
| 2 | 22.7 | 55.2 | 8.0 | 12.0 | 2.1 |
| 3 | 17.8 | 59.4 | 11.3 | 9.4 | 2.1 |

Figure 3.25 Die Shear Fracture Surfaces of BiAgX on Electrolytic Ni Sample Aged for 3000 hours at 200$^{o}$C (at.%).

3.5.1.3 Electrolytic Ni:P

Figure 3.26 is a cross section of the electrolytic Ni:P after 3000 hours at 200$^{o}$C. The Ni:P layer remains intact. This is consistent with the higher shear strength for the electrolytic Ni:P after 3000 hours aging. The failure interface remained at the solder-to-Ni-Sn intermetallic region (see Figure 3.27).

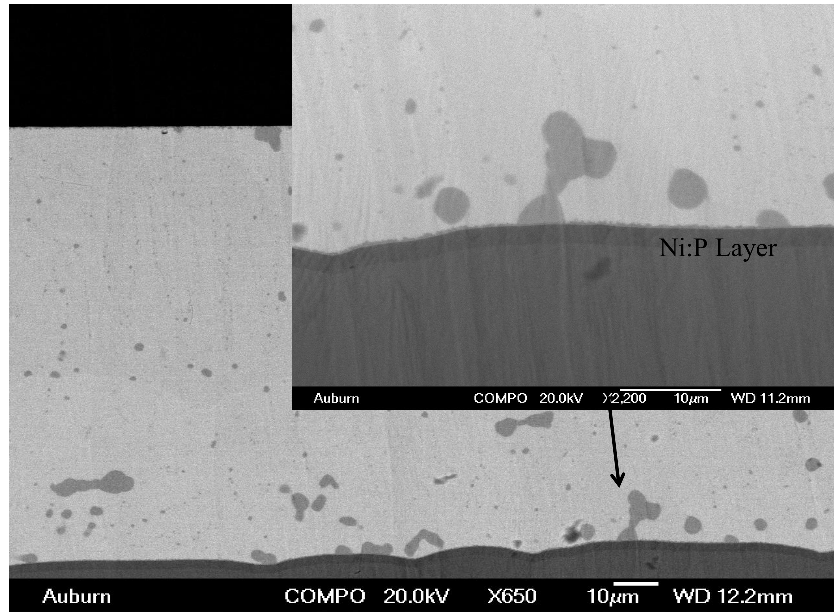


Figure 3.26 Cross Section of the BiAgX Die Attach on Electrolytic Ni:P after 3000 hours at 200$^{o}$C

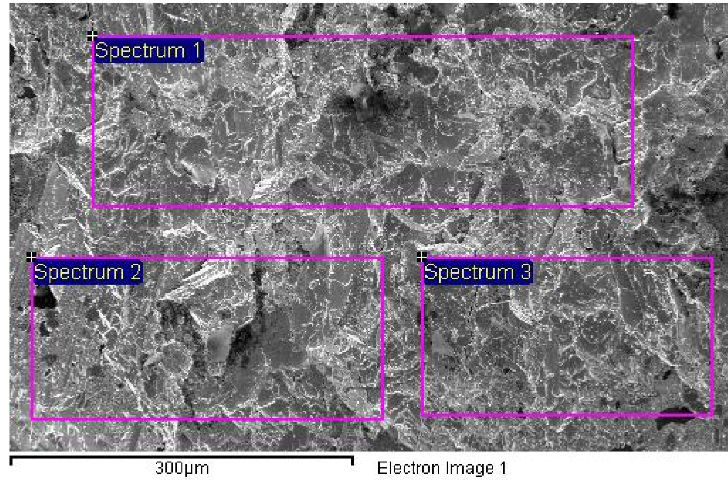


(a) Die Side

| Location | Ni | Ag | Sn | Bi |
|---|---|---|---|---|
| 1 | | 3.7 | 3.0 | 93.4 |
| 2 | 4.8 | | 7.7 | 87.5 |
| 3 | | 4.1 | 8.4 | 87.4 |

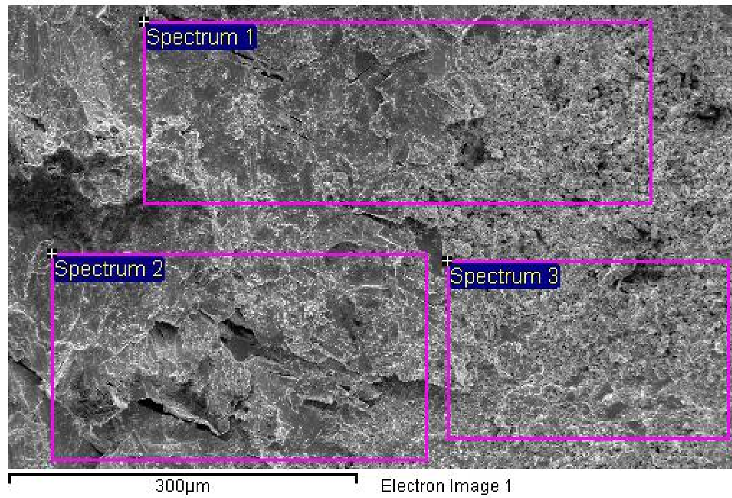


(b) Substrate Side

| Location | Ni | Ag | Sn | Bi |
|---|---|---|---|---|
| 1 | 7.2 | 5.2 | 3.1 | 84.6 |
| 2 | 3.3 | 7.5 | 2.4 | 86.8 |
| 3 | 26.7 | 6.1 | 9.0 | 53.7 |

Figure 3.27 Die Shear Fracture Surfaces of BiAgX on Electrolytic Ni:P Sample Aged for 3000 hours at 200°C (at.%)

3.5.1.4 Electrolytic Ni:Co

Figure 3.28 is a cross section of the electrolytic Ni:Co assembled with BiAgX after 500 hours at 200°C. There is significant $NiBi_3$ intermetallic formation. Figure 3.29 is a higher magnification elemental analysis of the cross section. Locations 1 and 2 were Ni-Sn IMC in $NiBi_3$ and locations 3and 4 corresponded to Ag in $NiBi_3$ and the Bi matrix. The elemental analysis of the fracture surface reveals that at 100 hours aging the failure was between the Bi and $NiBi_3$. However, after 500 hour aging, the $NiBi_3$ start to peel off from the copper surface, leaving bare Cu surface after shear testing. Figure 3.30 is the fracture analysis of the samples on electrolytic Ni:Co substrates after 500 hours aging. The failure was primarily at the Cu to $NiBi_3$ interface and partially along the $NiBi_3$ to Bi interface. This failure mode corresponds to the dramatic decrease in shear strength.

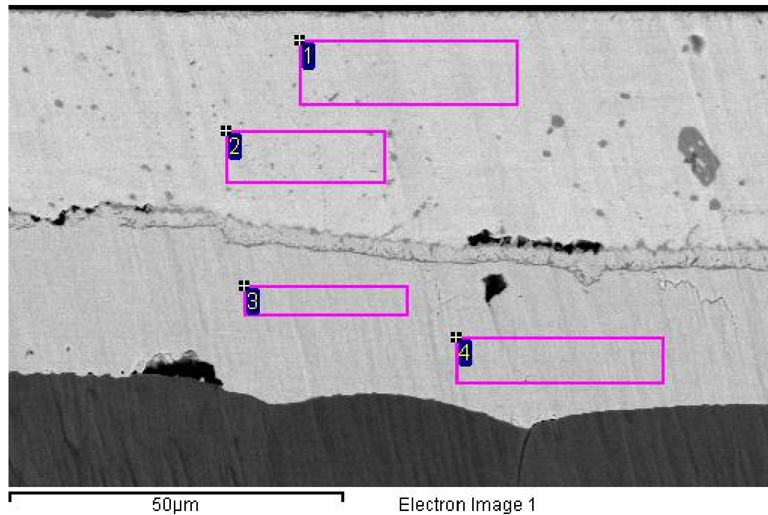


| Location | Ni | Bi |
|---|---|---|
| 1 | | 100.0 |
| 2 | | 100.0 |
| 3 | 23.9 | 76.1 |
| 4 | 23.0 | 77.0 |

Figure 3.28 Cross Section of the BiAgX Die Attach on Electrolytic Ni:Co after 500 hours at 200°C (at.%)

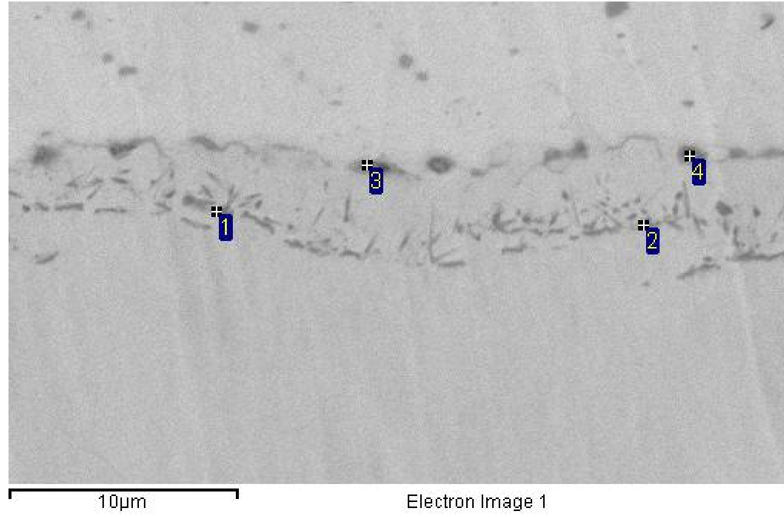


| Location | Ni | Sn | Bi | Ag |
| --- | --- | --- | --- | --- |
| 1 | 38.3 | 28.5 | 33.2 | |
| 2 | 41.2 | 30.3 | 28.5 | |
| 3 | 4.0 | | 27.3 | 68.7 |
| 4 | 3.3 | | 17.6 | 79.1 |

Figure 3.29 Cross Section of the BiAgX Die Attach on Electrolytic Ni:Co after 500 hours at $200^{o}C$ (at.%)

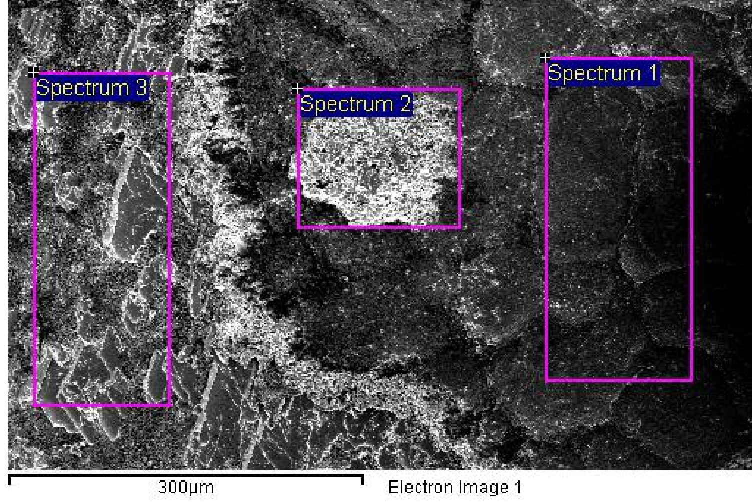


(a) Die Side

| Location | Ni | Ag | Sn | Bi |
|---|---|---|---|---|
| 1 | 22.72 | | | 77.28 |
| 2 | 24.13 | | | 75.87 |
| 3 | 4.42 | 17.13 | 2.78 | 75.67 |

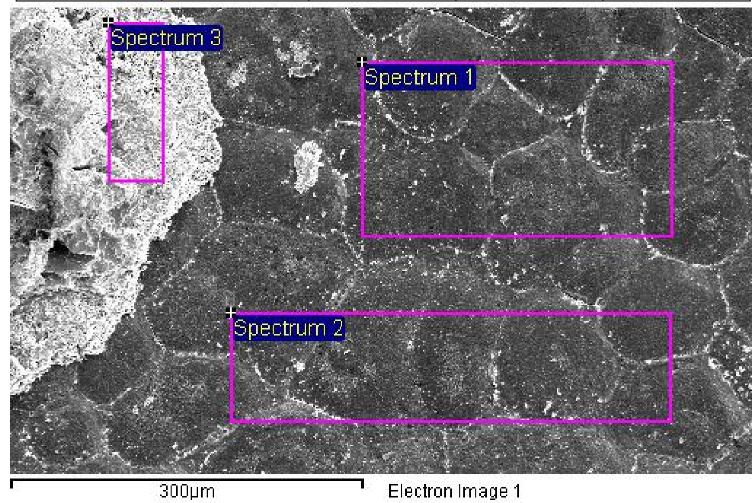


(b) Substrate Side

| Location | Ni | Cu | Bi |
|---|---|---|---|
| 1 | | 100.0 | |
| 2 | | 100.0 | |
| 3 | 23.84 | | 76.16 |

Figure 3.30 Die Shear Fracture Surfaces of BiAgX on Electrolytic Ni:Co Sample Aged for 500 hours at 200$^{o}$C (at.%).

### 3.6 Thermal Cycling

In the thermal cycling test, the samples were cycled between -55°C and 195°C. According to the profile in Figure 3.31, dwelling time at each temperature extreme was about 15 minutes.

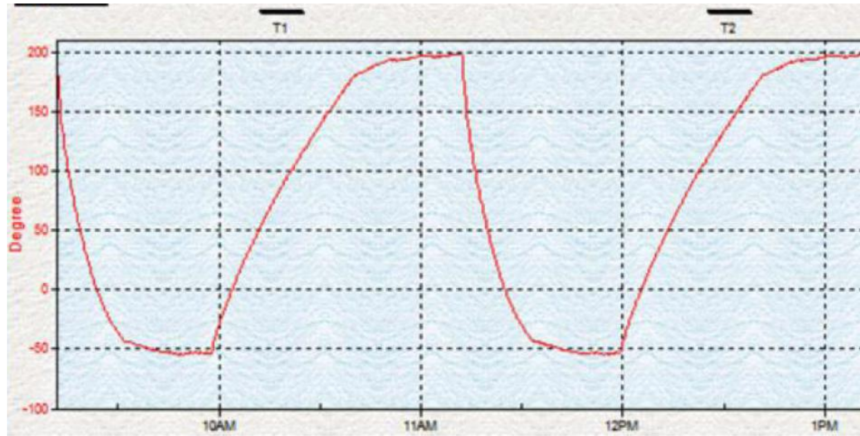


Figure 3.31 Thermal Cycle Profile

Table 3.3 presents the shear strength of (a) Electroless Ni:P, (b) Electrolytic Ni:P, (c) Electrolytic Ni, (d) Electrolytic Ni:Co. The initial shear strength of all samples exceeded the capability of the 100kg shear cartridge (>4kg/mm$^2$). This result was consistent with the initial shear strength of the aging samples. The shear strength of the electroless Ni:P and electrolytic Ni:P were both around 3 kg/mm$^2$ after 1500 cycles. The shear strengths of the electrolytic Ni and electrolytic Ni:Co decreased to less than 3 kg/mm$^2$ after 1500 cycles and 1000 cycles respectively. While decreased, all of the shear strengths was still much higher than the requirements of MIL-STD-883, Method 2019.7 (>0.1kg/mm$^2$) for 5 mm × 5 mm die after thermal cycling.

Table 3.3 Thermal Cycle Data for 5 mm × 5 mm SiC Die Attached to DBC Substrates in kg/mm$^2$

(a) Electroless Ni:P

| As Built | 100 Cycles | 500 Cycles | 1000 Cycles | 1500 Cycles |
|---|---|---|---|---|
| >4 | >4 | >4 | 3.03 | 3.06 |
| >4 | >4 | >4 | 3.27 | 3.47 |
| >4 | >4 | 3.94 | 3.1 | 3.0 |
| >4 | >4 | 3.9 | 3.2 | 3.4 |
| >4 | 3.95 | 3.82 | 3.32 | 3.04 |
| >4 | 3.62 | 3.7 | 3.09 | 2.96 |
| >4 | 3.99 | 3.64 | 3.57 | 2.89 |
| >4 | 3.92 | 3.59 | 3.44 | 3 |
| | | | AVG=3.25 | AVG=3.10 |

(b) Electrolytic Ni:P

| As Built | 100 Cycles | 500 Cycles | 1000 Cycles | 1500 Cycles |
|---|---|---|---|---|
| >4 | >4 | >4 | 3.65 | 3.12 |
| >4 | >4 | >4 | 3.68 | 3.02 |
| >4 | >4 | >4 | 3.62 | 2.77 |
| >4 | >4 | >4 | 3.44 | 3.1 |
| >4 | >4 | 3.84 | 3.41 | 2.98 |
| >4 | 3.98 | 3.88 | 3.46 | 2.92 |
| >4 | 3.73 | 3.74 | 3.49 | 3.01 |
| >4 | 3.95 | 3.63 | 3.34 | 3.29 |
| | | | AVG=3.51 | AVG=3.026 |

(c) Electrolytic Ni

| As Built | 100 Cycles | 500 Cycles | 1000 Cycles | 1500 Cycles |
|---|---|---|---|---|
| >4 | >4 | 4 | 2.72 | 2.64 |
| >4 | >4 | 3.98 | 3.34 | 3.02 |
| >4 | >4 | 3.83 | 3.14 | 2.75 |
| >4 | >4 | 3.71 | 3.45 | 2.39 |
| >4 | >4 | 3.57 | 2.38 | 2.97 |
| >4 | 3.53 | 3.47 | 3.29 | 2.51 |
| >4 | 3.99 | 3.27 | 3.34 | 2.3 |
| >4 | 3.98 | 3.24 | 2.88 | 2.95 |
| | | AVG=3.63 | AVG=3.07 | AVG=2.69 |

(d) Electrolytic Ni:Co

| As Built | 100 Cycles | 500 Cycles | 1000 Cycles |
|---|---|---|---|
| >4 | >4 | 2.85 | 3.43 |
| >4 | >4 | 3.26 | 3.2 |
| >4 | >4 | 3.78 | 2.47 |
| >4 | >4 | 3.42 | 3.69 |
| >4 | >4 | 2.36 | 2.43 |
| >4 | 3.95 | 2.96 | 2.11 |
| >4 | 3.39 | 1.9 | 2.96 |
| >4 | 3.98 | 3.91 | 2.24 |
| | | AVG=3.06 | AVG=2.82 |

3.6.1 Cross Section & Fracture Analysis

Figure 3.32 is the cross section near one edge of the die on an electroless Ni:P sample after 1500 cycles. A crack extending from the edge of the die to the solder was observed. Figure 3.33 is the element analysis of the fracture surface. On the substrate side, no Ni was detected at locations 1 and 2, which were around the perimeter of the die. Locations 3 and 4 reveals a small amount of Ni. Thus, the fracture in the perimeter area (1 and 2) corresponds to the cracks resulting from the thermal cycling. The results indicate the failure from the shear test was in the solder near the Ni-Sn intermetallic.

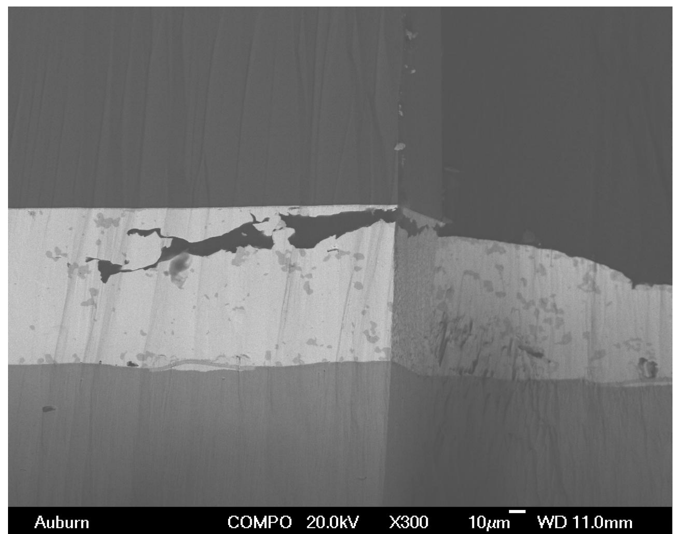


Figure 3.32 Cross Section of the BiAgX Die Attach on Electroless Ni:P after 1500 Thermal Cycles

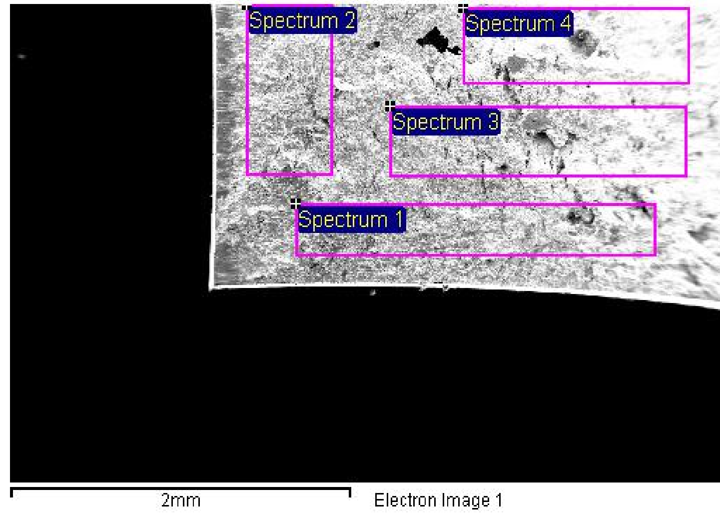


(a) Die Side

| | Ag | Au | Bi |
|---|---|---|---|
| 1 | 3.3 | 1.2 | 95.5 |
| 2 | 3.8 | | 96.2 |
| 3 | 4.2 | | 95.8 |
| 4 | 6.3 | | 93.7 |

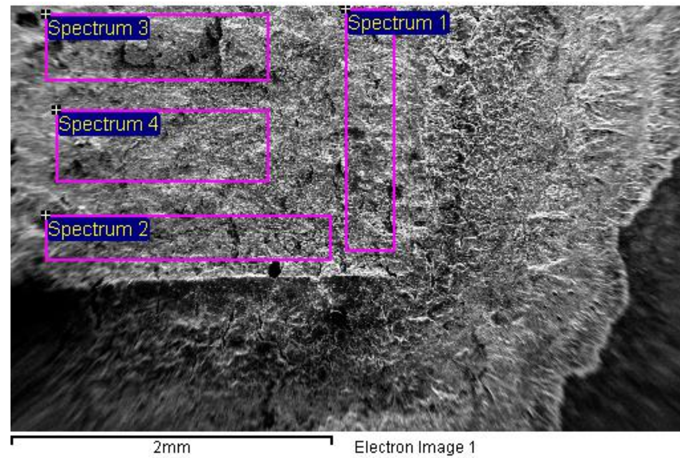


(b) Substrate Side

| | Ni | Ag | Sn | Au | Bi |
|---|---|---|---|---|---|
| 1 | | 4.9 | 1.7 | 1.5 | 91.9 |
| 2 | | 5.3 | 2.5 | | 92.2 |
| 3 | 2.7 | 5.7 | 2.4 | 1.3 | 87.9 |
| 4 | 4.2 | 6.6 | 2.1 | | 87.0 |

Figure 3.33 Die Shear Fracture Surfaces of BiAgX on Electroless Ni:P Sample after 1500 Thermal Cycles (at.%)

Figure 3.34 is a cross section of the electrolytic Ni:P after 1500 cycles. It shows similar cracking near the die perimeter. Figure 3.35 shows the elemental analysis of the fracture surfaces, which is quite similar to the results for the electroless Ni:P. The failure from shear testing occurred in the solder near the Ni-Sn intermetallic layer. The results corresponded to the similar decrease in the shear strength for the electroless and electrolytic Ni:P.

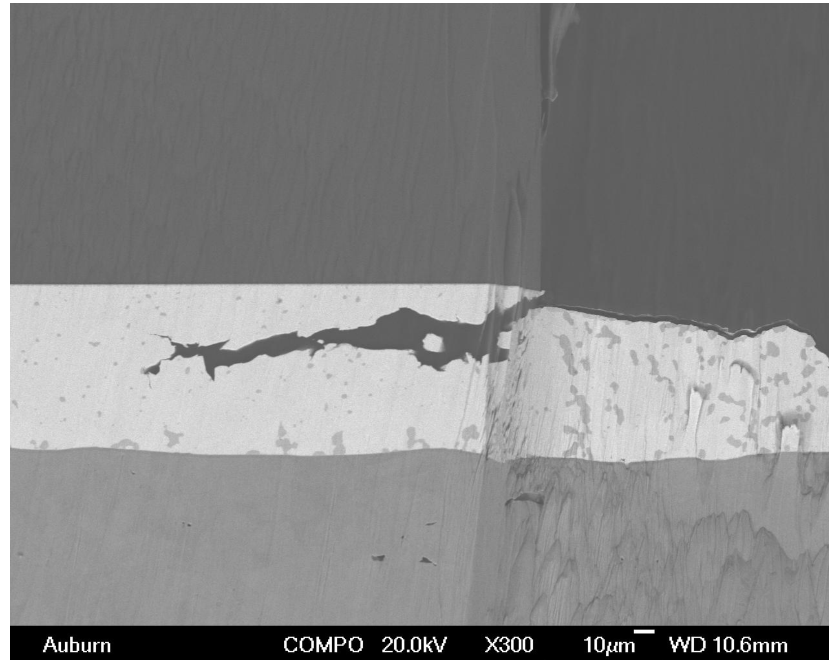


Figure 3.34 Cross Section of the BiAgX Die Attach on Electrolytic Ni:P after 1500 Thermal Cycles

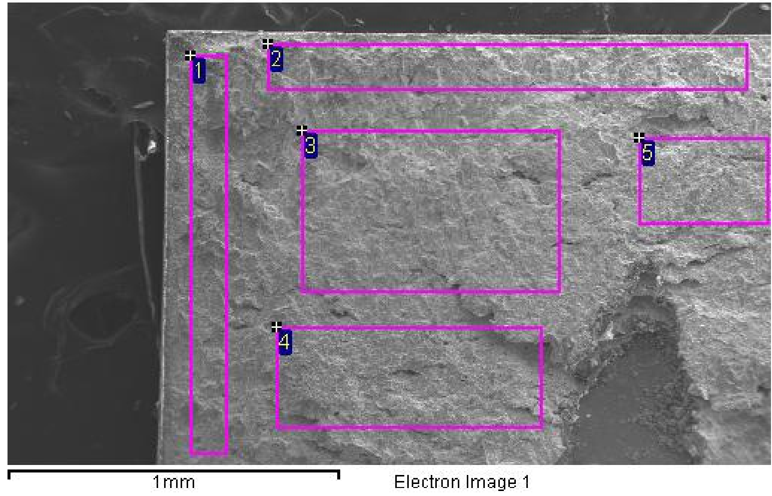


(a) Die Side

| Location | Ag | Bi |
|---|---|---|
| 1 | | 100.0 |
| 2 | | 100.0 |
| 3 | 10.3 | 89.7 |
| 4 | 7.9 | 92.1 |
| 5 | 10.7 | 89.3 |

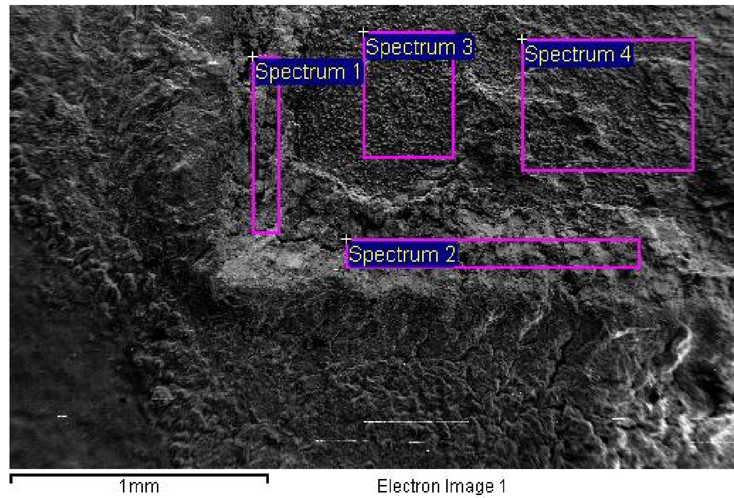


(b) Substrate Side

| Location | Ni | Ag | Sn | Bi |
|---|---|---|---|---|
| 1 | | | | 100.0 |
| 2 | | | | 100.0 |
| 3 | 10.3 | 18.3 | 7.2 | 64.2 |
| 4 | 11.3 | 15.3 | 6.0 | 67.4 |

Figure 3.35 Die Shear Fracture Surfaces of BiAgX on Electrolytic Ni:P Sample after 1500 Thermal Cycles (at.%)

Figure 3.36 shows a cross section of an electrolytic Ni sample after 1500 thermal cycles. A layer of $NiBi_3$ was formed and all of the Ni was consumed. The element analysis of fracture surfaces revealed that the failure after shear testing was in the $Ni_3Bi$ near the copper layer (see Figure 3.37). Figure 3.38 is an element analysis at the center of the fracture surfaces. No copper was detected on location 3 and 4 which revealed that the failure had also partially occurred along the interface of the Bi to the $NiBi_3$.

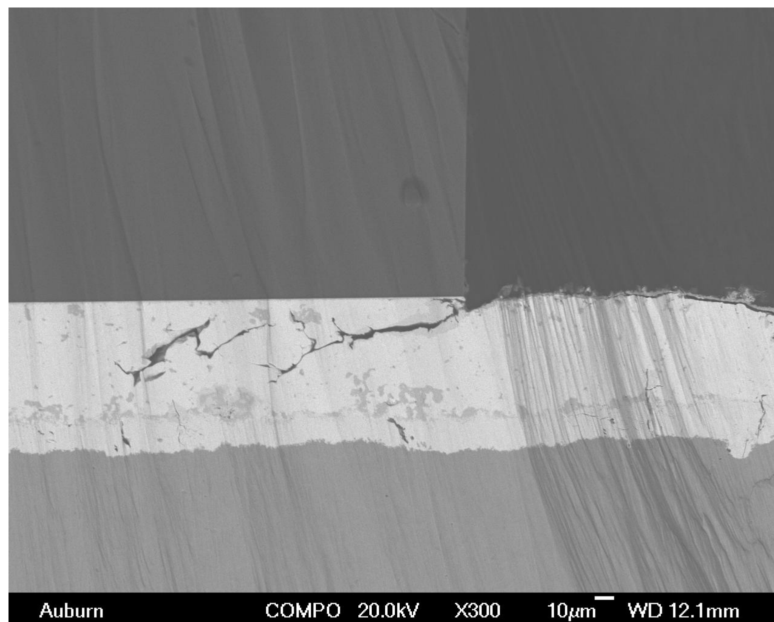

Figure 3.36 Cross Section of the BiAgX Die Attach on Electrolytic Ni after 1500 Thermal Cycles

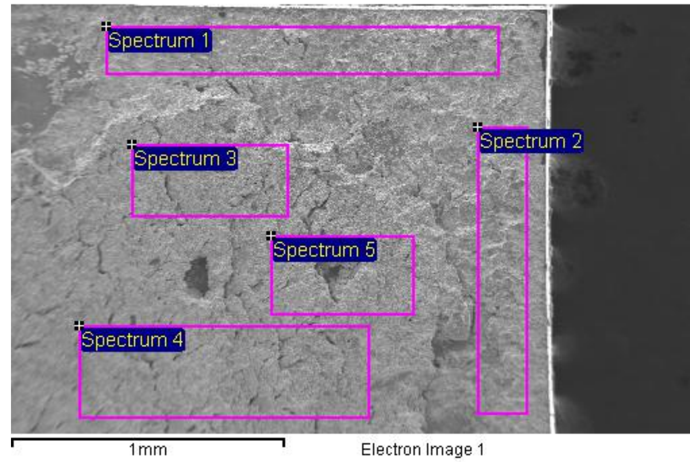


(a) Die Side

| | Ni | Ag | Bi |
|---|---|---|---|
| 1 | | 3.1 | 96.9 |
| 2 | | 3.6 | 96.4 |
| 3 | 29.5 | | 70.5 |
| 4 | 27.3 | | 72.7 |
| 5 | 27.7 | | 72.3 |

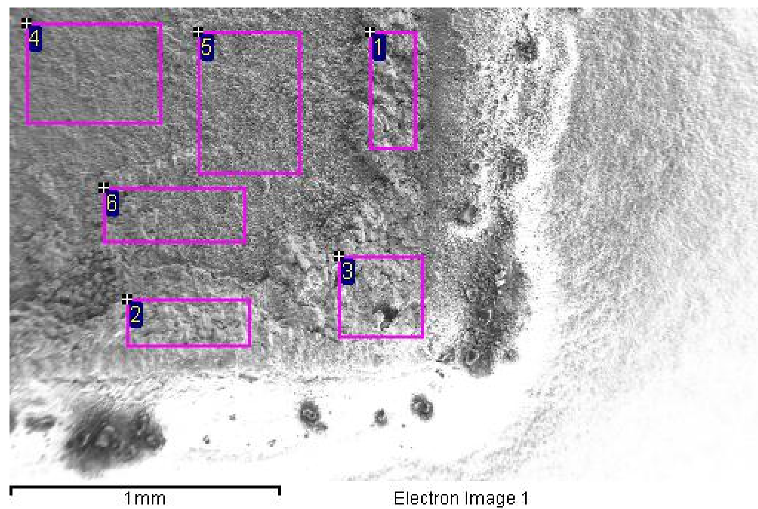


(b) Substrate Side

| | Ni | Cu | Bi |
|---|---|---|---|
| 1 | | | 100 |
| 2 | | | 100 |
| 3 | | | 100 |
| 4 | 16.5 | 33.8 | 49.8 |
| 5 | 18.5 | 25.3 | 56.2 |
| 6 | 21.2 | 19.0 | 59.8 |

Figure 3.37 Die Shear Fracture Surfaces of BiAgX on Electrolytic Ni Sample after 1500 Thermal Cycles (at.%)

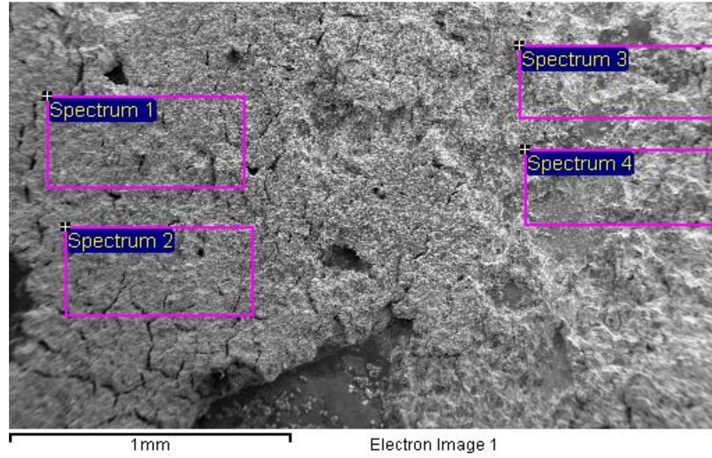


(a) Die Side

| | Ni | Ag | Sn | Bi |
|---|---|---|---|---|
| 1 | 26.2 | | | 73.8 |
| 2 | 25.0 | | | 75.0 |
| 3 | | 5.5 | 4.4 | 90.1 |
| 4 | 8.2 | 3.5 | 10.4 | 77.8 |

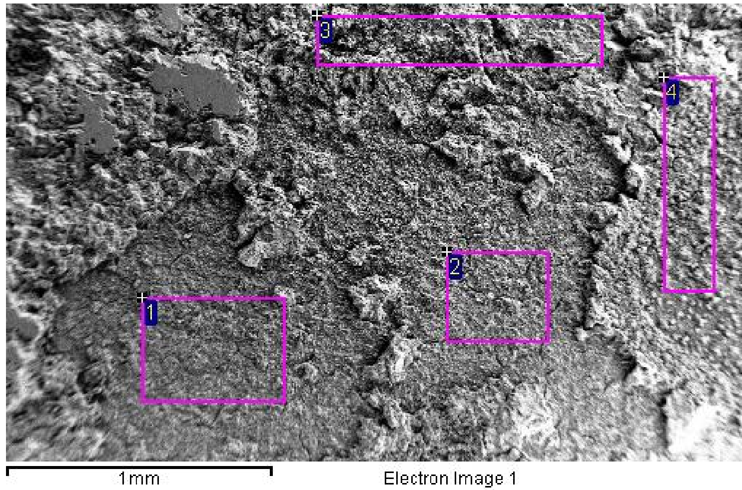


(a) Substrate Side

| | Cu | Ni | Ag | Sn | Bi |
|---|---|---|---|---|---|
| 1 | 49.4 | 11.7 | | | 38.9 |
| 2 | 33.4 | 16.2 | | | 50.4 |
| 3 | | 27.7 | | | 72.3 |
| 4 | | 25.9 | 25.3 | 11.1 | 37.8 |

Figure 3.38 Die Shear Fracture Surfaces at Center of BiAgX on Electrolytic Ni Sample after 1500 Thermal Cycles (at.%)

Figure 3.39 shows a cross section of an electrolytic Ni:Co sample after 1000 thermal cycles. A layer of $NiBi_3$ was formed during the cycling. In Figure 3.40, the element analysis of the fracture surfaces after shear testing indicated the $NiBi_3$ layer was completely peeled off from the Cu surface. In the aging result, failures around the interface between the Bi to $NiBi_3$ layer were also founded. However, this kind of failure was not found in the 1000 cycles thermal cycled sample.

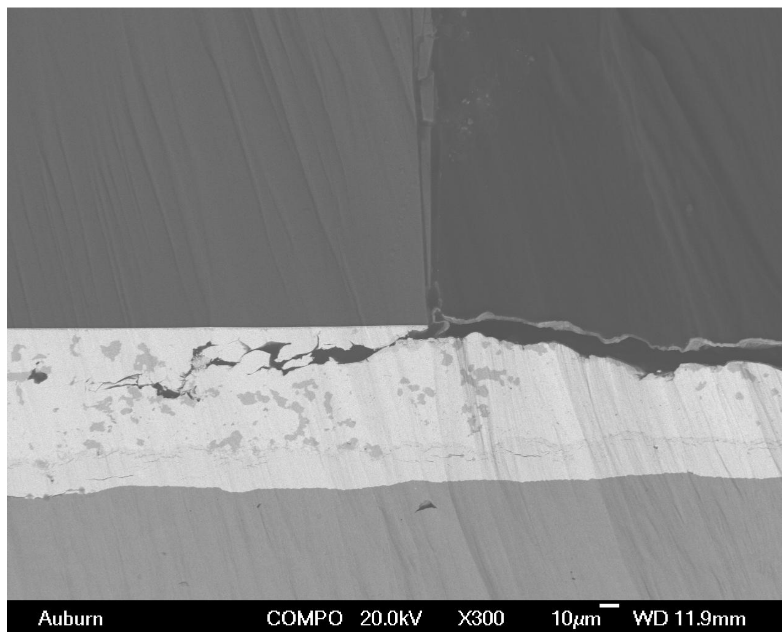


Figure 3.39 Cross Section of the BiAgX Die Attach on Electrolytic Ni:Co after 1000 Thermal Cycles

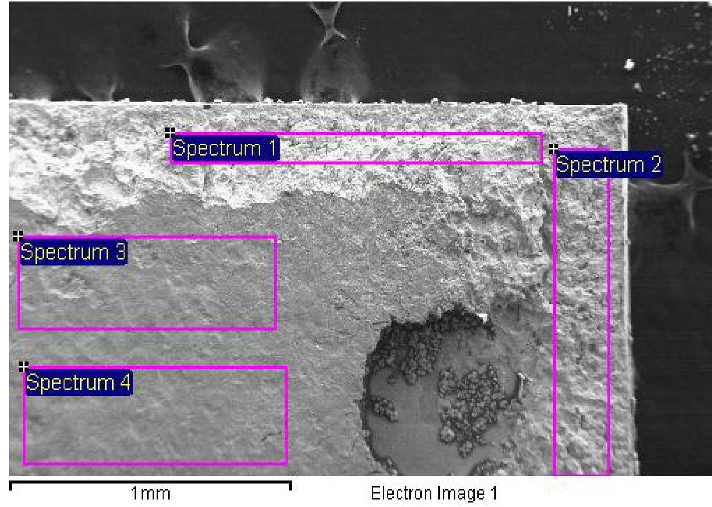


(a) Die Side

| | Ni | Bi | Ag | Sn |
|---|---|---|---|---|
| 1 | | 100.0 | | |
| 2 | | 88.9 | 8.0 | 3.1 |
| 3 | 22.3 | 77.7 | | |
| 4 | 22.8 | 77.2 | | |

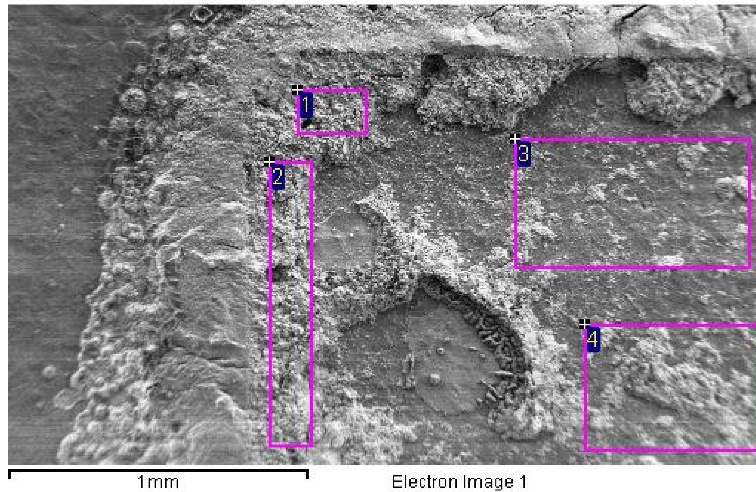


(b) Substrate Side

| | Ni | Cu | Bi | Ag | Sn |
|---|---|---|---|---|---|
| 1 | | | 79.1 | 15.7 | 5.2 |
| 2 | | | 81.4 | 18.6 | |
| 3 | 2.8 | 85.8 | 11.4 | | |
| 4 | 7.8 | 65.4 | 26.8 | | |

Figure 3.40 Die Shear Fracture Surfaces of BiAgX on Electrolytic Ni:Co Sample after 1000 Thermal Cycles (at.%)

### 3.7 Summary

BiAgX is a promising lead-free solder for 200$^{o}$C applications. The degradation of shear strength from low to high is electrolytic Ni:P, elecreoless Ni:P, electrolytic pure Ni and Ni:Co. After aging at 200$^{o}$C, the $NiBi_3$ was formed in electroless Ni:P, electrolytic pure Ni and electrolytic Ni:Co which caused the decrease in shear strength. No $NiBi_3$ was observed with the electrolytic Ni:P samples. While decreased, all of the shear strengths were still much higher than the requirements of MIL-STD-883, Method 2019.7 after high temperature storage and thermal cycling.

# CHAPTER 4 DIE ATTACH USING AUGE SOLDER PREFORM

## 4.1 Introduction

There are several widely used gold containing solders, such as AuSn, AuGe, and AuSi. Especially in high temperature applications, binary gold solder is a very promising candidate. The melting point of Au-Ge12 (wt%), Au-Sn20, Au-Si3.1 alloys are 356$^{o}$C, 280$^{o}$C, 363$^{o}$C, respectively.

Solder preforms such as AuGe are fluxless, because the high content of Au can prevent oxidation of the solder surface. Exact solder volume control is another advantage of using a solder preform. Also, with good thermal conductivity and low CTE AuGe is used in high power electronics. Physical properties are shown in Table. 4.1. Ge has very low solubility in Au at room temperature (see Figure 4.1). At 361$^{o}$C, the solubility is about at. 3% [66], Au is not soluble in Ge.

Table 4.1 Physical Properties of AuGe12 [65]

| Properties | 88Au12Ge |
|---|---|
| Liquidus ($^{o}$C) | 356 |
| Thermal Conductivity (W/mK) | 44 |
| Tensile Strength (PSI) | 26,835 |
| Shear Strength (PSI) | 26,825 |
| Thermal Expansion Coefficient @20$^{o}$C (PPM/$^{o}$C) | 13 |

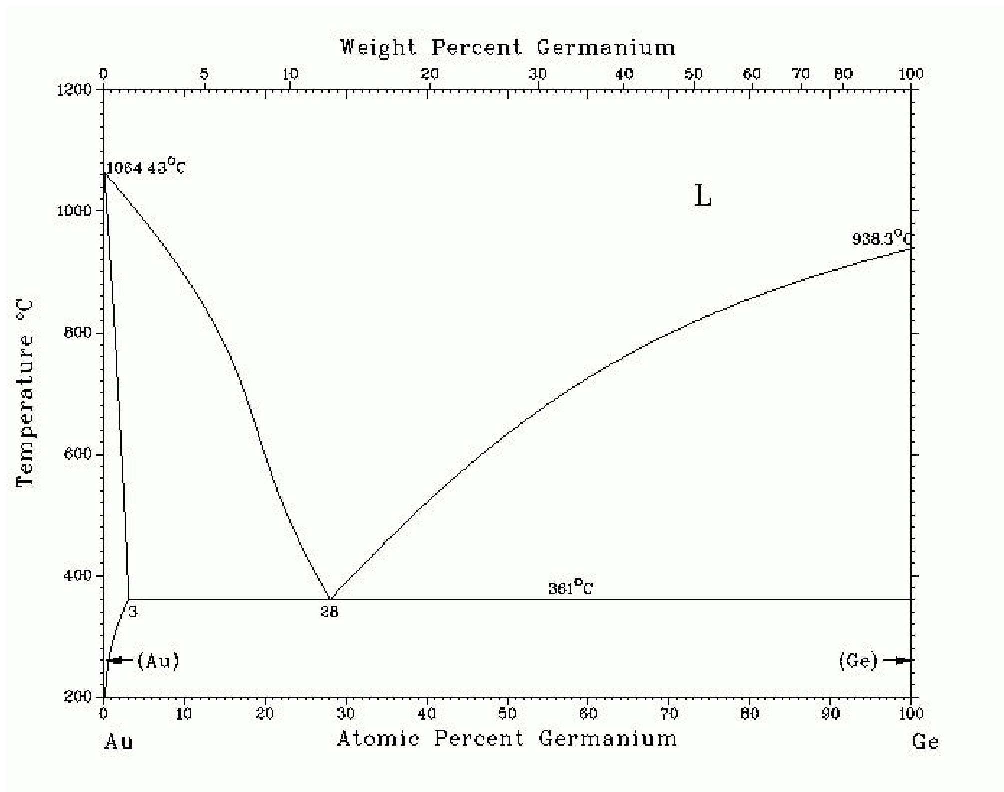

Figure 4.1 Au-Ge Phase Diagram [66]

## 4.2 Literature Review

Nickel is widely used as a diffusion barrier in surface finishes (Ni/Au, Ni/Pd/Au, Ni/Ag) for copper metallization. Surface finishes are of particular importance for high temperature electronics exposed to the atmosphere to prevent oxidation of the Cu. Especially for AuGe applied on copper, copper will diffuse into the gold and form intermetallics during high temperature use, which decreases solder joint strength dramatically. Chidambaram, et al. [67][68] reported 5μm copper was all consumed by AuGe bulk solder. $Au_3Cu$ was found to start spalling from the surface after 300 hours 300°C aging. After 500 hours aging, the ball shear strength dropped from 21.6 g/mil$^2$ to 1.8 g/mil$^2$.

Many publications also reveal that by dissolution process of Ge, Ni-Ge IMC layer is formed during assembly and grows thicker after high temperature storage. Normally, a thick

IMC layer can decrease the shear strength of the solder joint, since they are typically brittle. Lang, et al. [69] has shown a degradation from 70 MPa to 19 MPa in shear strength after 400 hours aging at 330$^{o}$C due to the formation of NiGe IMC. With a 250-nm-thick tungsten diffusion barrier on the Ni, the shear strength only decrease from 60 MPa to 41 MPa which was more than two times higher after 1000 hours aging than that on substrates with no barrier. Chidambaram, et al. [68] found the formation of NiGe and $Ni_5Ge_3$ when they using ENIG as an under bump metallurgy (UBM). The ball shear strength decrease from 14 g/mil$^2$ to 10.8 g/mil$^2$ after 500 hours aging at 300$^{o}$C. Tanimoto, et al. [70] also reported a dramatic decrease from 134 MPa to 6.2 MPa in shear strength after 3000 hours aging at 300$^{o}$C. Ni plating was used in all these experiments, but the details of the Ni composition and plating process were not discussed in these papers. Ni plating may influence the shear strength. For example, Palmer, et al. [71] has shown with the same assembly process, the shear strength of AuGe degraded faster on electrolytic Ni than on electroless Ni:P when aging at 300$^{o}$C.

In this work, different Ni platings were explored with AuGe12 alloy in 300$^{o}$C and 325$^{o}$C storage. Thermal cycling testing from 300$^{o}$C to -55$^{o}$C was also conducted.

### 4.3 Potential Intermetallic Compounds

As mentioned above, Cu and Au may form intermetallic $Au_3Cu$, which dramatically reduces the solder joint strength. With thick enough nickel as a barrier layer, no intermetallic will form between Cu and Au. Moreover, Ni does not form any intermetallic with Au or Cu (see Figures 4.2, 4.3), but it is continuously soluble in Cu. Ni also has the same limited solubility in Au.

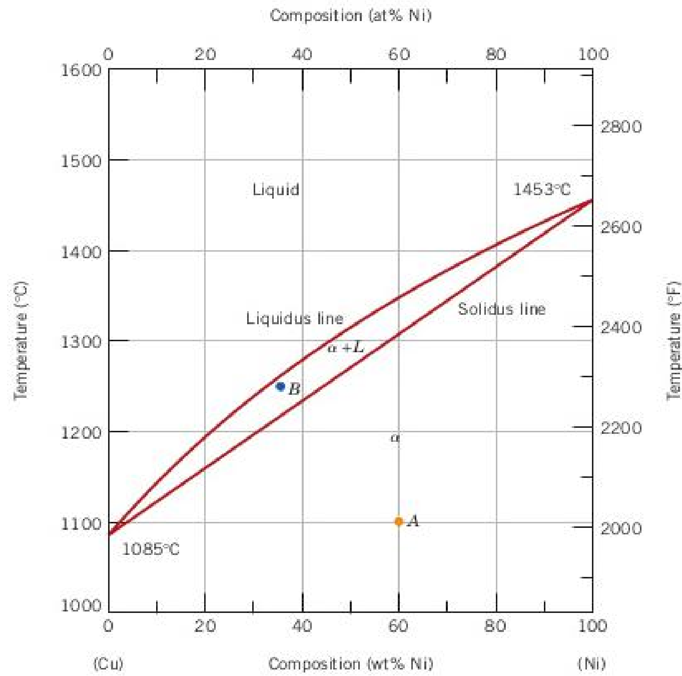


Figure 4.2 Ni-Cu Phase diagram [72]

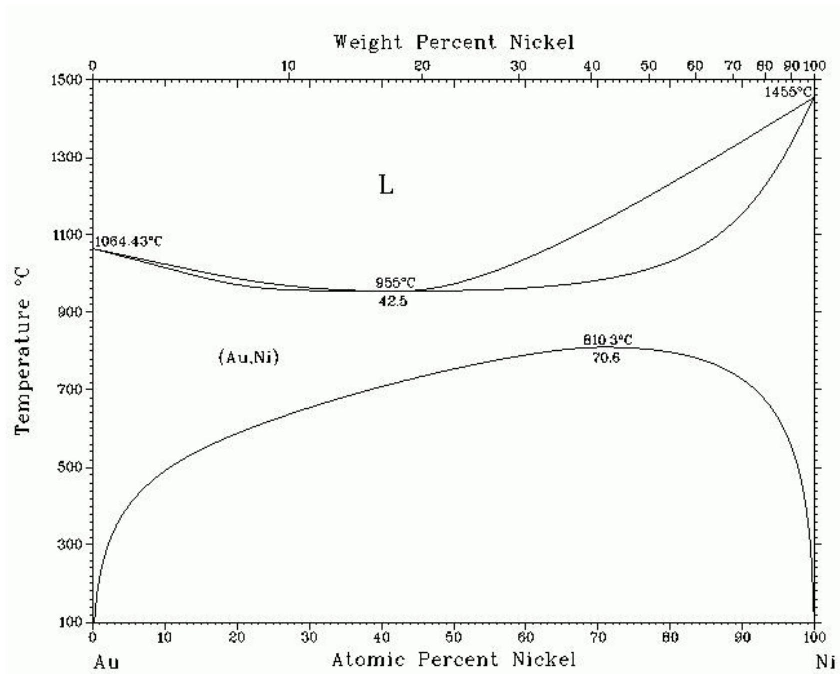


Figure 4.3 Ni-Au Phase diagram [73]

The only potential of forming intermetallic is between Ni and Ge. At room temperature, NiGe, ε phase $Ni_5Ge_3$, $Ni_2Ge$ and β phase $Ni_3Ge$ can be observed when the nickel gradually diffuses into the Ge.

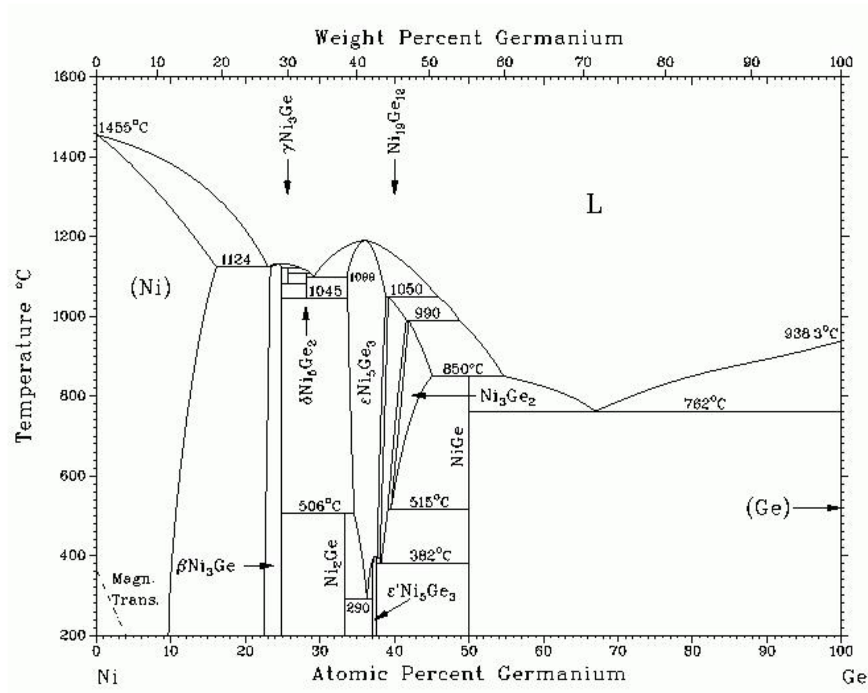


Figure 4.4 Ni-Ge Phase diagram [74]

## 4.4 Assembly

### 4.4.1 Die

The die for the AuGe die attach studies were fabricated from SiC wafers with deposited Ti/Ti:W (10:90 wt%)/Au (25 nm/ 50 nm/ 50 nm) metallization. After thin film deposition, 3 μm of Au was electroplated. The wafers were diced into 2 mm x 2 mm die for the aging test and for the thermal cycling test the die was 5 mm x 5 mm.

4.4.2 Substrate

The substrates were 96% aluminum oxide direct bond copper (DBC) from Stellar Industries (Millbury, MA, USA). The size of the DBC was 19.05 cm × 13.716 cm. The thickness of the $Al_2O_3$ was 0.635 mm and copper was 0.2032 mm thick. The copper thickness for the thermal cycling test was 0.127 mm since thick copper may cause more rapid failure due to the CTE mismatch between the Cu and the aluminum oxide.

For the AuGe studies, the DBC Cu was plated with a 5 μm Ni layer and a 0.17 μm Au layer. The Ni plating compositions are shown in Table 4.2.

Table 4.2 Nickel Composition as Provided by the Plating Suppliers

| Plating | Ni Percentage (at.%) |
|---|---|
| Pure Ni - electroplated | 100% |
| Ni:P - electroplated | 80%~85% |
| Ni:P - electroless | 80%~85% |
| Ni:B - electroless | ~97% |

4.4.3 Process

The Au88Ge12 preforms used in this experiment were purchased from Materion Advanced Materials Group (Buffalo, NY, USA). The dimensions were 2 mm×2 mm×25.4 μm (length*wide*height) for the aging samples and 5 mm×5 mm×25.4 μm for thermal cycling. An SST 3150 vacuum furnace was used for the assembly. A 3 min ramping from room temperature to 385°C with a 3 min peak hold time was used to achieve good wetting and flow. To spread the solder uniformly out, a 500 grams weight was placed on the top of the SiC die (see Figure 4.5). Figure 4.6 is the reflow profile measured by the thermocouple of the SST.

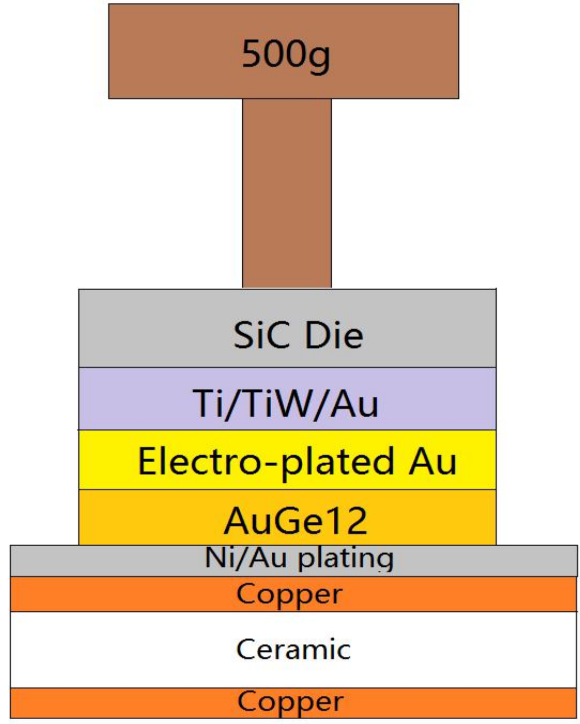


Figure 4.5 AuGe Die Attach Configuration

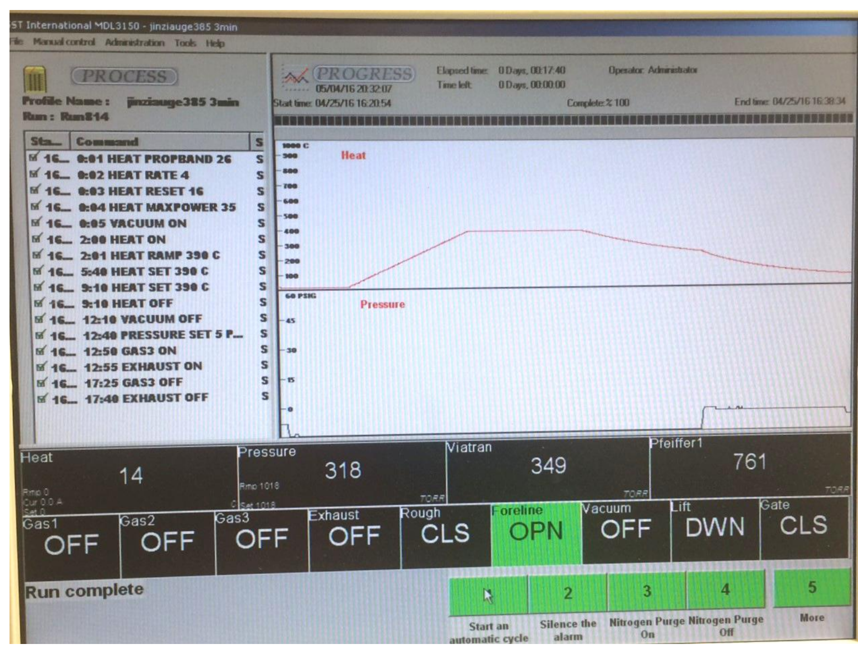


Figure 4.6 AuGe Assembly Profile

## 4.5 Initial Shear Data

The die shear strength was measured with a Dage PC2400 using a 100kg shear module. The test height was set to 2.54 μm and the test speed was 50.8 μm/s. For AuGe die attach, the initial shear strengths for the Ni:P electroless and electrolytic samples were high, with the average shear strength of 13.31 kg/mm$^2$ and 14.31kg/mm$^2$ (Table 4.3). Both the Pure Ni and Ni:B samples had significantly lower shear strengths.

Table 4.3 AuGe Initial Average Shear Strength

| Plating | Initial Average Shear Data (kg/mm$^2$) |
| --- | --- |
| Pure Ni - electroplated | 5.64 |
| Ni:P - electroless | 13.31 |
| Ni:B - electroless | 3.77 |
| Ni:P- electroplated | 14.31 |

### 4.5.1 Cross Section & Fracture Analysis

Figure 4.7 is a cross section of the AuGe die attach on electrolytic Ni. The Ge has precipitated out of the Au: there is very limited solubility of Ge in Au at room temperature. The appearance of the bulk solder was similar for all three Ni finishes.

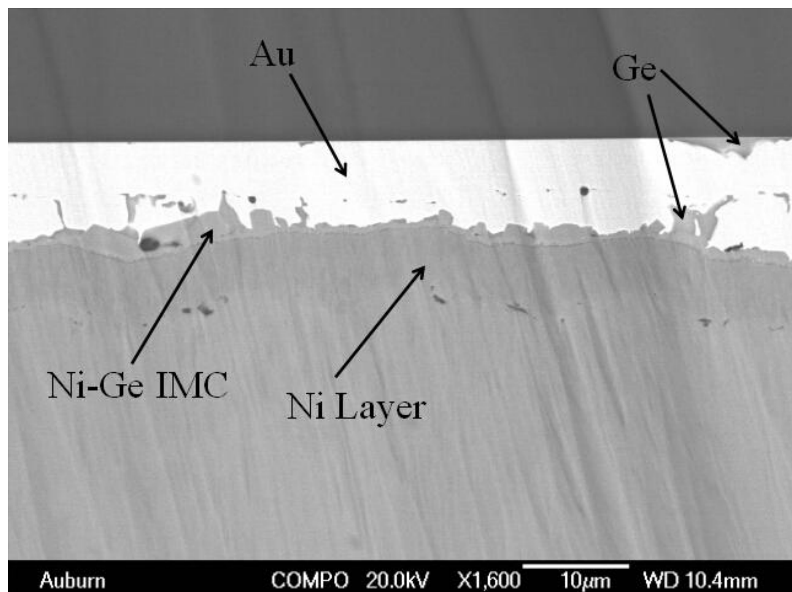


Figure 4.7 As-built AuGe on Electrolytic Ni Cross Section.

Figure 4.8 is an image and elemental analysis of the electrolytic Ni sample in the region near the substrate. The intermetallic (locations 3, 4 and 5) corresponds to $Ni_5Ge_3$. Interestingly, Au was detected at points 6 and 7.

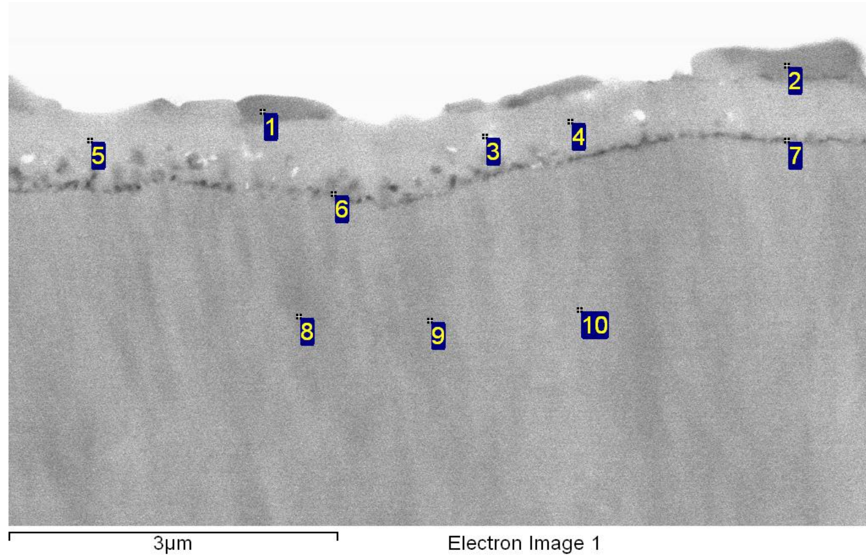


| Location | Ni | Ge | Au |
|---|---|---|---|
| 1 | 8.2 | 88.3 | 3.5 |
| 2 | 5.3 | 90.0 | 4.7 |
| 3 | 61.5 | 38.5 | 0.0 |
| 4 | 64.5 | 33.6 | 1.9 |
| 5 | 64.4 | 35.6 | 0.0 |
| 6 | 59.4 | 35.2 | 5.4 |
| 7 | 39.8 | 55.2 | 5.0 |
| 8 | 100.0 | 0.0 | 0.0 |
| 9 | 100.0 | 0.0 | 0.0 |
| 10 | 100.0 | 0.0 | 0.0 |

Figure 4.8 As-built AuGe on Electrolytic Ni Cross Section and Elemental Analysis (at.%)

A high magnification image of the $Ni_5Ge_3$ intermetallic-to-Ni interface (Figure 4.9) reveals voiding. Surface analysis of the die shear sample fracture surfaces (Figure 4.10) revealed $Ni_5Ge_3$ and a small amount of Au (~5 at.%) on the die side and only Ni on the substrate side.

Formation of voids and failure at this interface is consistent with the lower significantly lower shear strength shear for the electrolytic Ni samples.

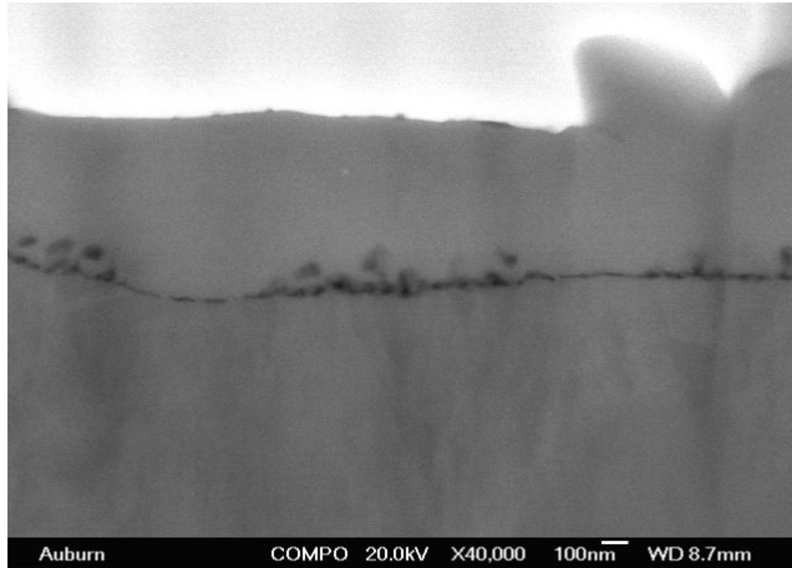


Figure 4.9 High Magnification Image of $Ni_5Ge_3$-to-Ni Interface Showing Voiding

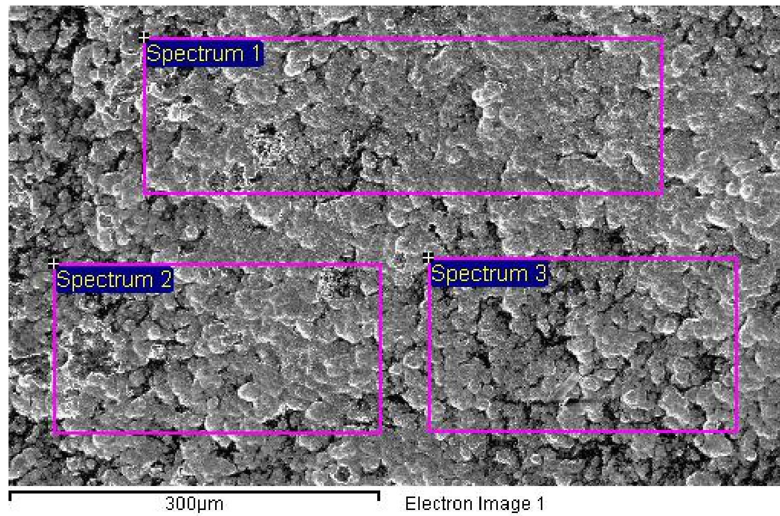


(a) Die Side

| Location | Ni | Ge | Au |
|---|---|---|---|
| 1 | 55.9 | 40.0 | 4.1 |
| 2 | 56.1 | 38.2 | 5.7 |
| 3 | 54.8 | 41.1 | 4.1 |

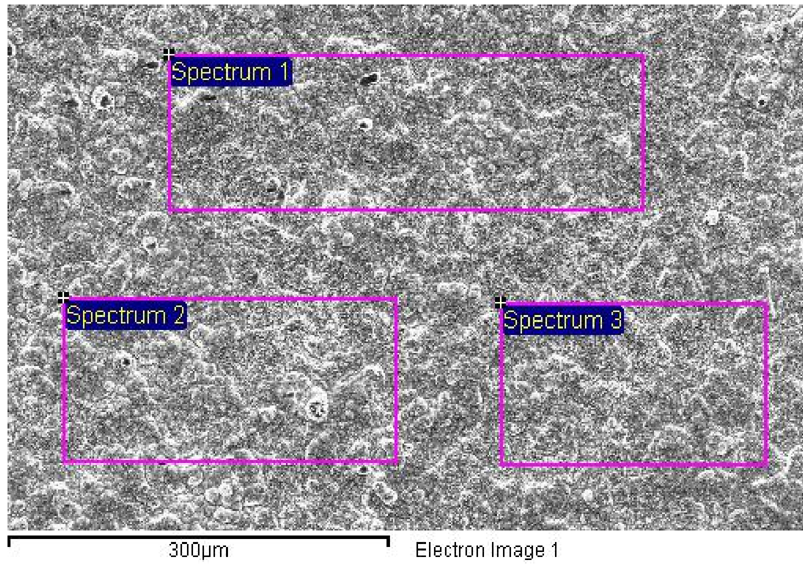


(b) Substrate Side

| Location | Ni |
|---|---|
| 1 | 100.0 |
| 2 | 100.0 |
| 3 | 100.0 |

Figure 4.10 Die Shear Fracture Surfaces of As-built AuGe on Electrolytic Ni Sample (at.%)

Figure 4.11 is a cross section and elemental analysis of the as-built AuGe on Ni:B sample. The die and die attach separated from the substrate during sample preparation along the NiGe-to-Ni interface. Figure 4.12 is the element analysis of fracture surfaces.

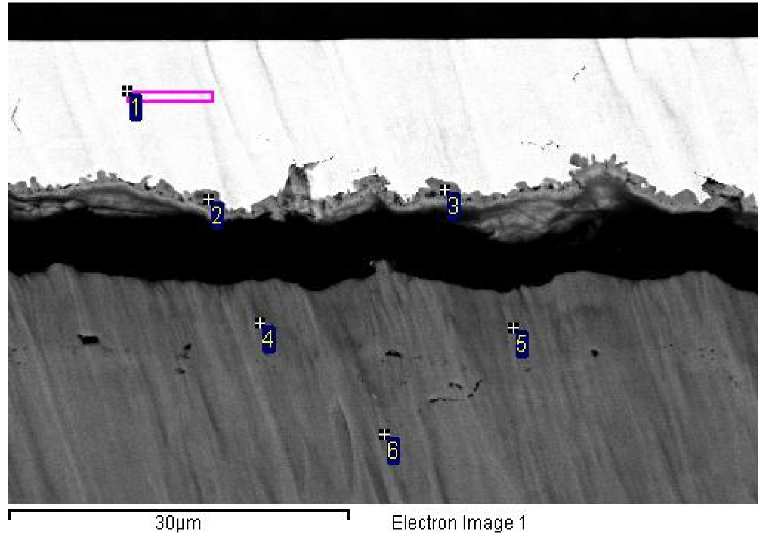


| Location | Ni | Ge | Au | Cu |
|---|---|---|---|---|
| 1 | 0.0 | 0.0 | 100.0 | 0.0 |
| 2 | 51.2 | 48.8 | 0.0 | 0.0 |
| 3 | 48.2 | 51.8 | 0.0 | 0.0 |
| 4 | 100.0 | 0.0 | 0.0 | 0.0 |
| 5 | 100.0 | 0.0 | 0.0 | 0.0 |
| 6 | 0.0 | 0.0 | 0.0 | 100.0 |

Figure 4.11 As-built AuGe on Electroless Ni:B Cross Section and Elemental Analysis (at.%)

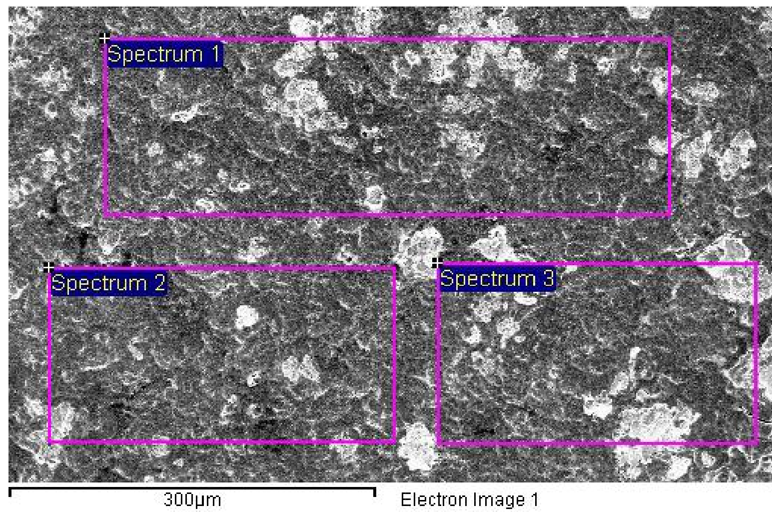


(a) Die Side

| Location | Ni | Ge | Au |
|---|---|---|---|
| 1 | 57.0 | 36.8 | 6.2 |
| 2 | 60.1 | 36.1 | 3.9 |
| 3 | 55.5 | 36.5 | 8.0 |

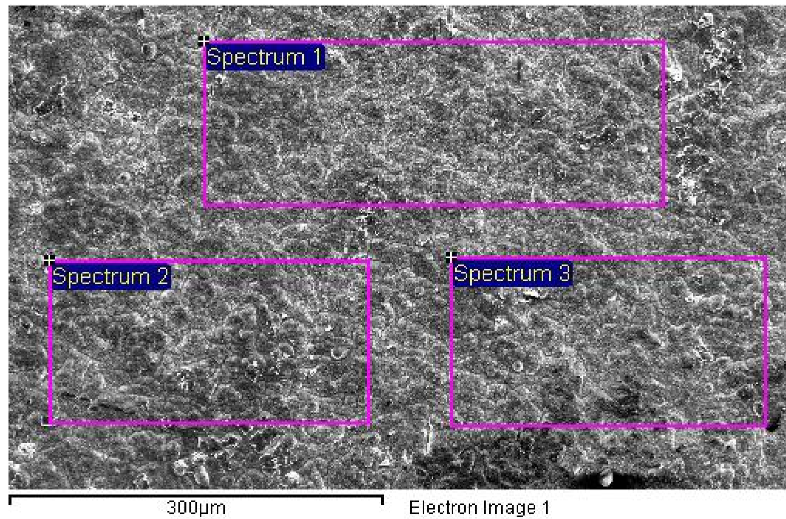


(b) Substrate Side

| Location | Ni |
|---|---|
| 1 | 100.0 |
| 2 | 100.0 |
| 3 | 100.0 |

Figure 4.12 Die Shear Fracture Surfaces of As-built AuGe on Electroless Ni:B Sample (at.%)

Figure 4.13 is a cross section and elemental analysis of the AuGe assembly on electroless Ni:P at the Ni:P interface. Locations 1, 2 and 3 correspond to approximately NiGe. Locations 6 and 7 indicate an increased P concentration due to the consumption of Ni in the formation of NiGe.

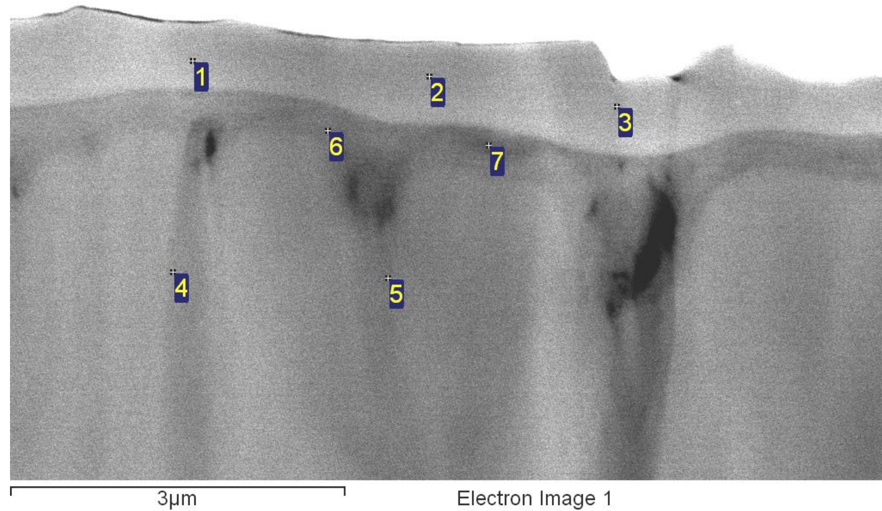


| Location | Ni | P | Ge |
|---|---|---|---|
| 1 | 53.8 | 0.0 | 46.2 |
| 2 | 50.4 | 0.0 | 49.6 |
| 3 | 52.0 | 0.0 | 48.0 |
| 4 | 86.7 | 13.3 | 0.0 |
| 5 | 85.5 | 14.5 | 0.0 |
| 6 | 68.4 | 19.2 | 12.4 |
| 7 | 68.9 | 20.5 | 10.6 |

Figure 4.13 As-built AuGe on Electroless Ni:P Cross Section and Elemental Analysis at Ni Interface (at.%)

Figure 4.14 is fracture analysis of an as-built AuGe assembly on electroless Ni:P. Ni, Ge and Au were found on both die and substrate side. Die side contained more Au, which indicates the failure was in the Au near the Ni-Ge intermetallic layer.

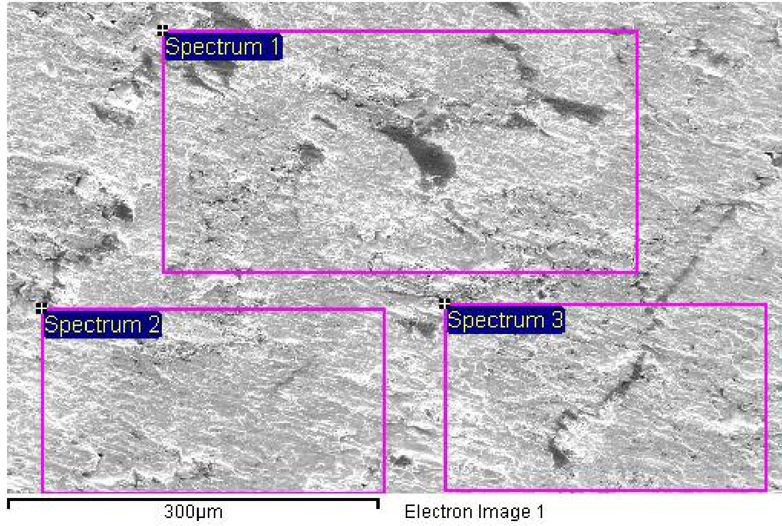


(a) Die Side

| Location | Ni | Ge | Au |
|---|---|---|---|
| 1 | 3.5 | 5.9 | 90.6 |
| 2 | 1.7 | 7.4 | 90.9 |
| 3 | 2.6 | 5.0 | 92.5 |

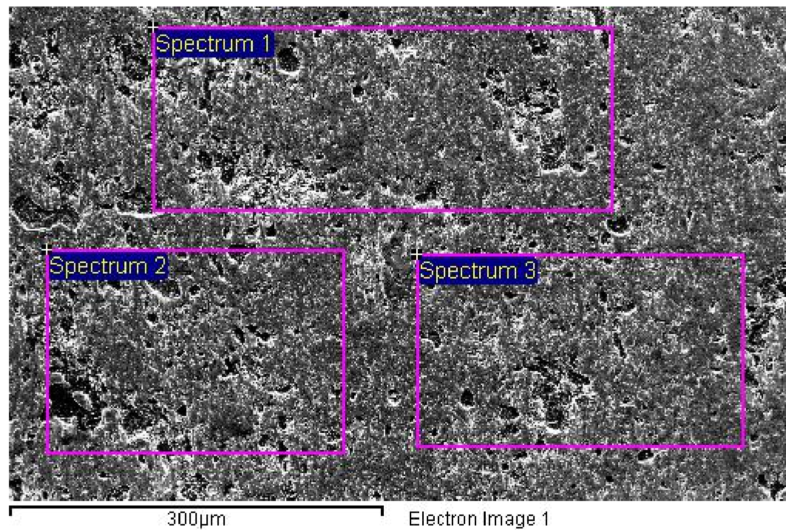


(b) Substrate Side

| Location | Ni | Ge | Au |
|---|---|---|---|
| 1 | 12.4 | 15.6 | 72.1 |
| 2 | 15.9 | 15.1 | 69.0 |
| 3 | 16.4 | 15.3 | 68.3 |

Figure 4.14 Die Shear Fracture Surfaces of As-built AuGe on Electroless Ni:P Sample (at.%)

### 4.6 Aging Study

Based on the as-built die shear results, only the AuGe on electroless Ni:P and electrolytic Ni:P samples were aged at 300$^{o}$C. Figure 4.15 plots the shear strength as a function of aging time at 300$^{o}$C. Eight samples were sheared for each test interval. For the electroless Ni:P, the shear strength started to decrease at 1000 hours, and the results became stable after 2000 hours. After 100 hours aging, the electrolytic Ni:P showed an obvious decrease in shear strength. There was a slow degradation in shear strength after 100 hours aging. Both of platings had about 30% decrease in shear strength compared with the with initial data after 3000 hours of aging.

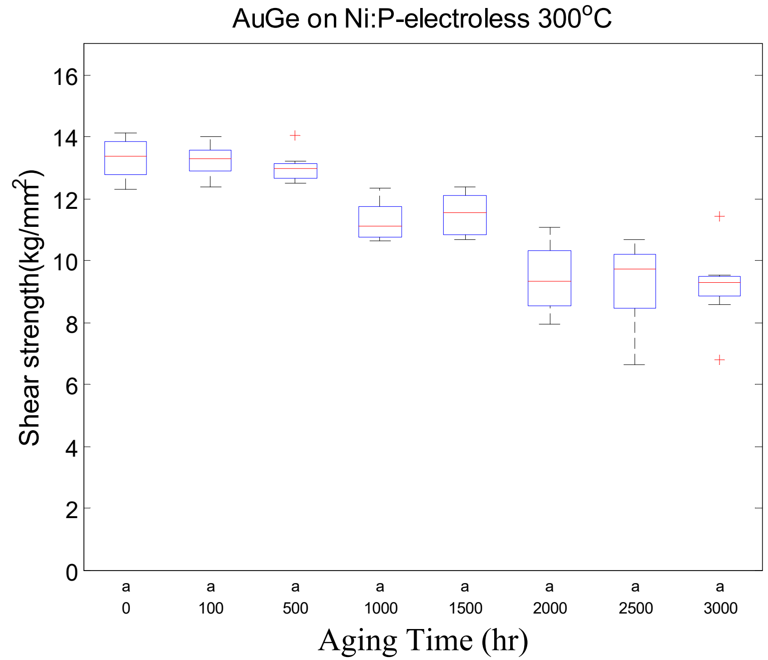


(a)

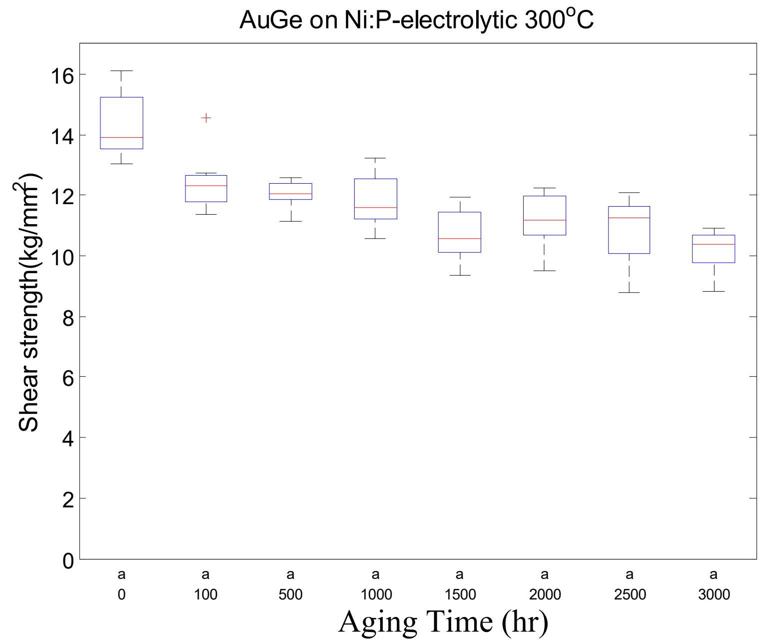


(b)

Figure 4.15 Die Shear Strength of AuGe as a Function of Storage Time at 300°C on (a) Electroless Ni:P (b) Electrolytic Ni:P

Based on the shear data of the 300°C aging test, a 325°C aging test was conducted. Figure 4.16 is the box plot of shear strength with aging at 325°C for 3000 hours. The shear strength of the electroless Ni:P had an obvious decrease until 500 hours aging. After 500 hours, the rate of decrease become slower. Like the 300°C aging, a sharp drop was observed after 100 hours aging with the electrolytic Ni:P samples. After 100 hours, the shear strength dropped to approximately 9kg/$mm^2$ and was relatively stable through 3000 hours.

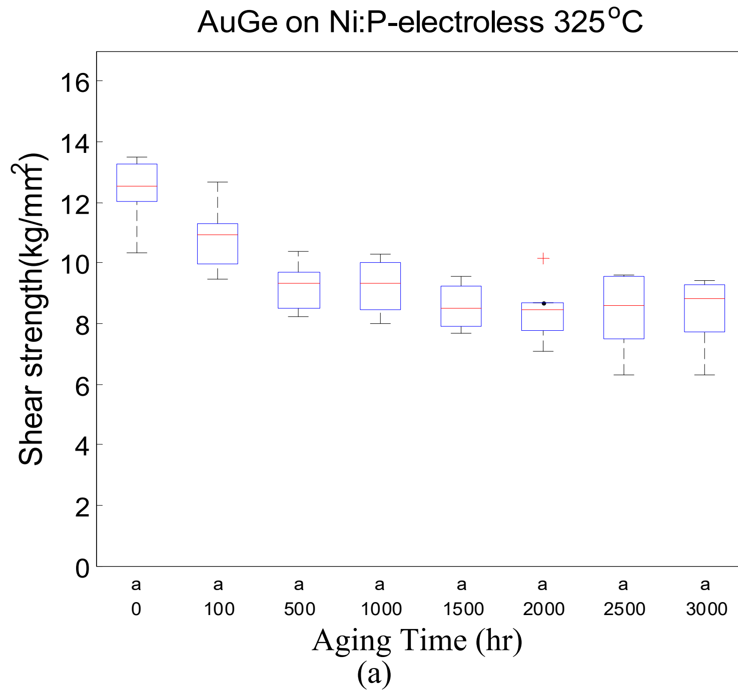


(a)

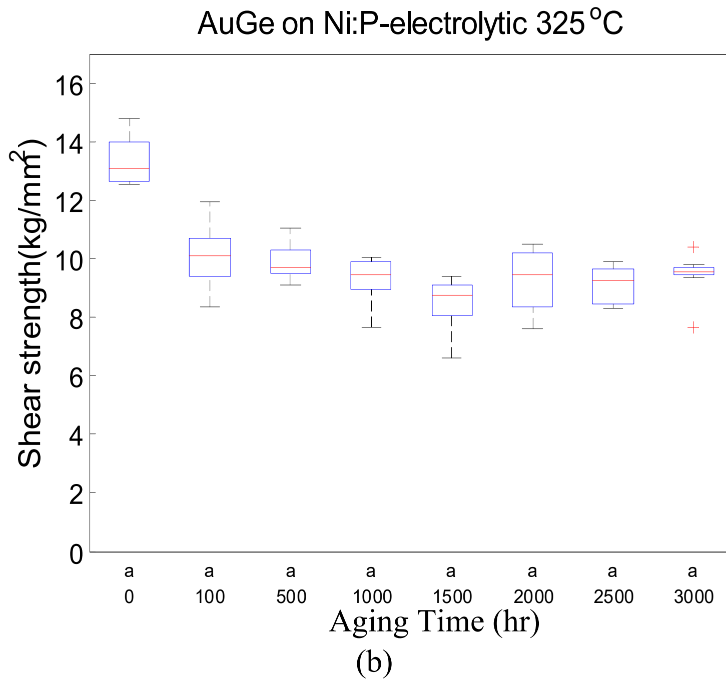


(b)

Figure 4.16 Die Shear Strength of AuGe as a Function of Storage Time at 325°C on

(a) Electroless Ni:P (b) Electrolytic Ni:P

4.6.1 Cross Section

Figure 4.17 is a cross section and elemental analysis of a AuGe on electroless Ni:P sample after 3000 hours at 300°C. The Ni-Ge intermetallic was consistent with $Ni_2Ge$ at location 3 and with $Ni_3Ge$ at locations 4 and 5. The cross section for the 1000 hours aged sample (Figure 4.18) indicated location 4 was consistent with $Ni_2Ge$, $Ni_3Ge$ was found close the to the Ni layer at location 5. Comparing the location 4 of the 3000 hours and 1000 hours aged samples, the $Ni_3Ge$ layer become thicker in the 3000 hours aged sample. The P content in the Ni increased due to the consumption of Ni, the ratio was close to $Ni_3P$. And there was 1-2% Ni diffused into the copper after aging at location 8. When doing elemental analysis close to the Au to IMC interface, ~5% Ni has diffused into the Au, but no Ni is detected in the bulk Au. Elemental analysis of the fracture surfaces (Figure 4.19) showed Au with Ni (~5%) on the die side and Au with Ni (30-36%) and Ge (7-8%) on the substrate side. This would indicate the fracture occurred in the Au near the Ni-Ge intermetallic.

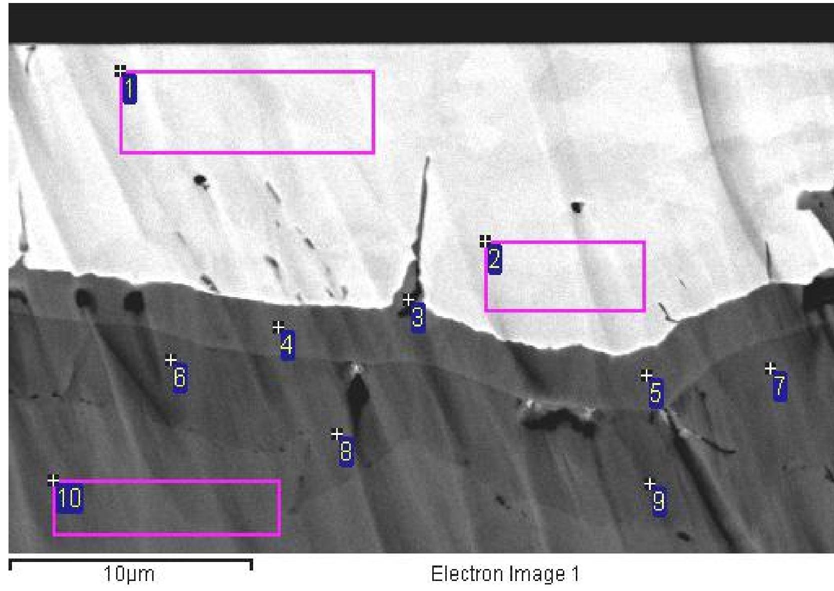


| Location | Au | Ni | Ge | P | Cu |
|---|---|---|---|---|---|
| 1 | 100.0 | | | | |
| 2 | 94.3 | 5.8 | | | |
| 3 | 5.4 | 63.0 | 31.6 | | |
| 4 | | 76.1 | 23.9 | | |
| 5 | | 75.6 | 24.4 | | |
| 6 | | 75.2 | | 24.8 | |
| 7 | | 74.8 | | 25.2 | |
| 8 | | 83.4 | | 16.6 | |
| 9 | | 82.5 | | 17.5 | |
| 10 | | 1.7 | | | 98.3 |

Figure 4.17 Electroless Ni:P 3000hr 300$^{o}$C Aging and Elemental Analysis (at.%)

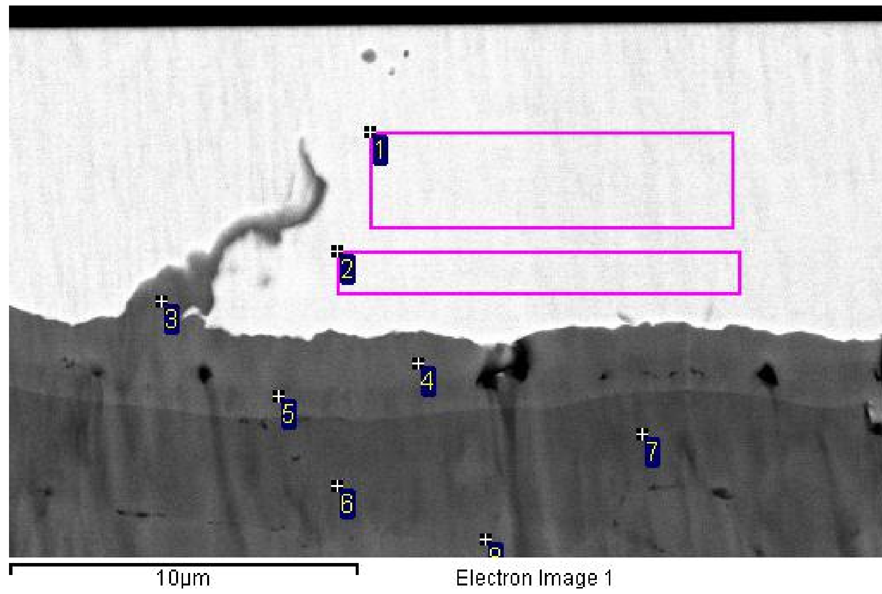


| Location | Ni | Ge | Au | P | Cu |
|---|---|---|---|---|---|
| 1 | 2.7 | 0.0 | 97.3 | 0.0 | |
| 2 | 5.4 | 0.0 | 94.6 | 0.0 | |
| 3 | 67.4 | 32.6 | 0.0 | 0.0 | |
| 4 | 67.6 | 32.4 | 0.0 | 0.0 | |
| 5 | 74.1 | 25.9 | 0.0 | 0.0 | |
| 6 | 82.9 | 0.0 | 0.0 | 17.1 | |
| 7 | 76.0 | 0.0 | 0.0 | 24.0 | |
| 8 | | | | | 100.00 |

Figure 4.18 Cross Section of the AuGe Die Attach on Electroless Ni:P after 1000 hours at 300$^{o}$C

(at.%)

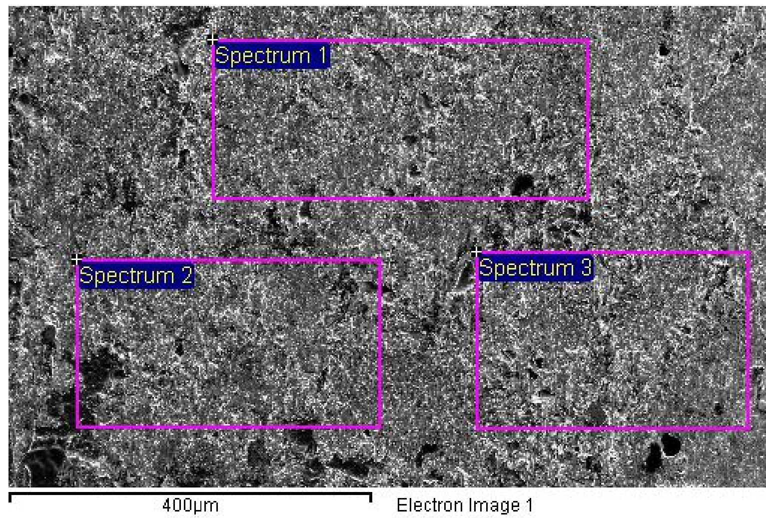


(a) Die Side

| Location | Au | Ni |
|---|---|---|
| 1 | 94.7 | 5.3 |
| 2 | 93.7 | 6.3 |
| 3 | 94.6 | 5.4 |

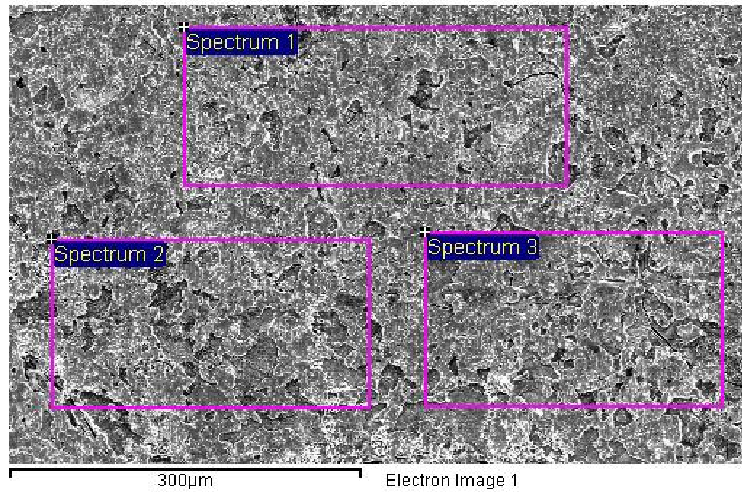


(b) Substrate Side

| Location | Ni | Ge | Au |
|---|---|---|---|
| 1 | 36.0 | 8.0 | 56.0 |
| 2 | 29.7 | 7.3 | 63.0 |
| 3 | 30.1 | 8.1 | 61.8 |

Figure 4.19 Die Shear Fracture Surfaces of AuGe on Electroless Ni:P Sample Aged for 3000 hours at 300°C (at.%)

Figure 4.20 is a cross section and elemental analysis of a AuGe on electrolytic Ni:P sample after 3000 hours at 300°C. It showed element analysis results similar to the electroless Ni:P sample. Element analysis of fracture surfaces in Figure 4.21 showed less Ni content on the substrate side when compare to the electroless Ni:P sample. This would indicate the fracture occurred more in the Au bulk than the electroless Ni:P sample.

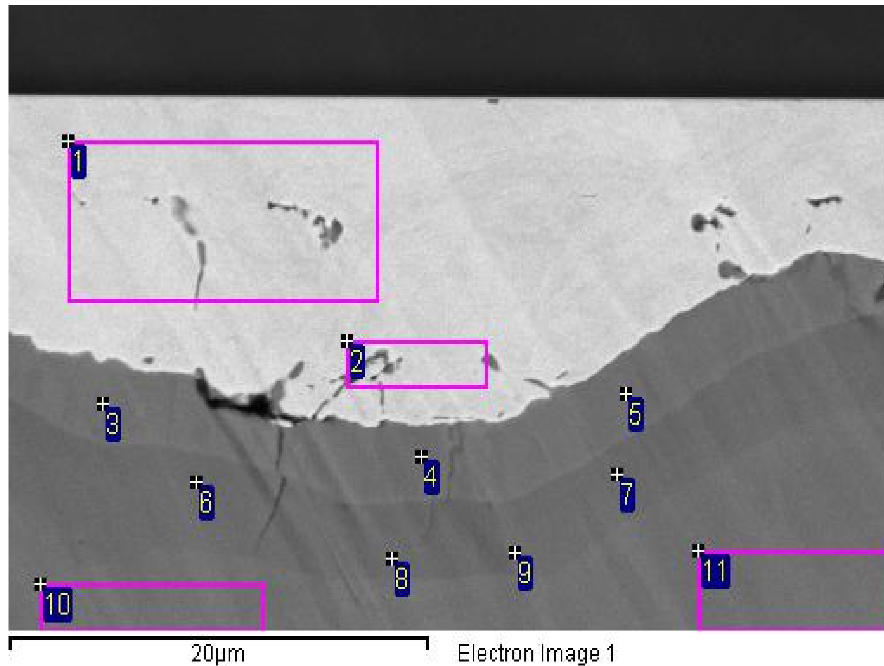


| Location | Au | Ni | Ge | P | Cu |
|---|---|---|---|---|---|
| 1 | 100.0 | | | | |
| 2 | 94.14 | 5.86 | | | |
| 3 | | 74.4 | 25.6 | | |
| 4 | | 74.6 | 25.4 | | |
| 5 | | 75.3 | 24.7 | | |
| 6 | | 75.0 | | 25.0 | |
| 7 | | 78.5 | | 21.5 | |
| 8 | | 84.4 | | 15.6 | |
| 9 | | 86.5 | | 13.5 | |
| 10 | | 1.7 | | | 98.3 |
| 11 | | | | | 100.0 |

Figure 4.20 Electrolytic Ni:P after 3000 hours of 300°C Aging and Elemental Analysis (at.%)

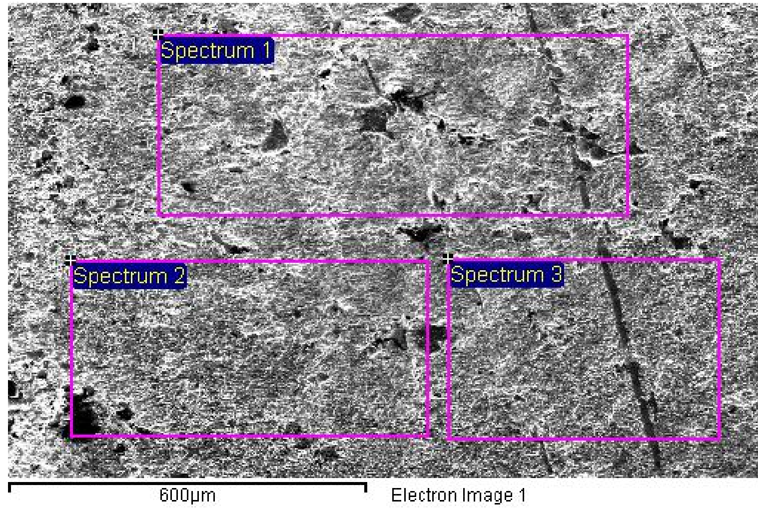


(a) Die Side

| Location | Ni | Au |
|---|---|---|
| 1 | 5.3 | 94.7 |
| 2 | 4.6 | 95.4 |
| 3 | 5.2 | 94.8 |

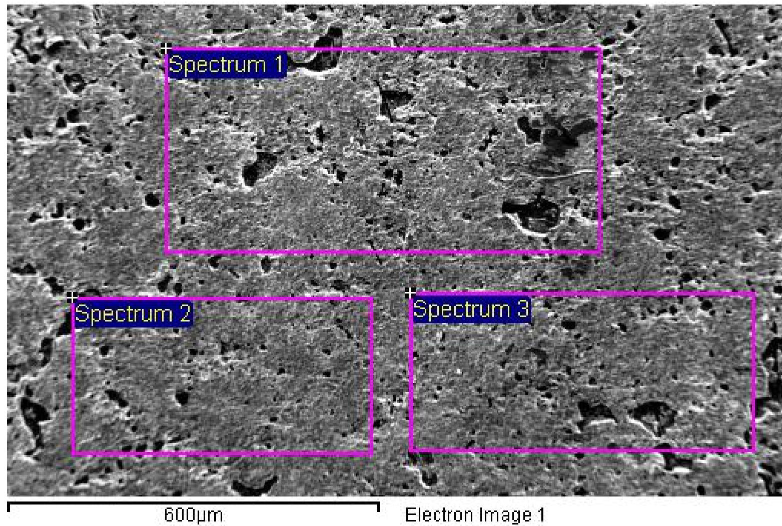


(b) Substrate Side

| Location | Ni | Ge | Au |
|---|---|---|---|
| 1 | 22.5 | 9.4 | 68.2 |
| 2 | 12.2 | 6.5 | 81.3 |
| 3 | 20.3 | 7.2 | 72.5 |

Figure 4.21 Die Shear Fracture Surfaces of AuGe on Electrolytic Ni:P Sample Aged for 3000 hours at 300$^{o}$C(at.%)

Figure 4.22 is a cross section and elemental analysis of a AuGe on electroless Ni:P sample after 3000 hours at 325°C. Location 3, 4 show that the entire intermetallic layer was uniform and consistent with $Ni_3Ge$. The Ni:P layer near the intermetallic had a higher P ratio which was close to $Ni_3P$. Element analysis of the fracture surfaces (Figure 4.23) showed ~5% Ni on the die side. The Ni(28~34%) and Ge(7~11%) content on the substrate side was very close to the 300°C aging results.

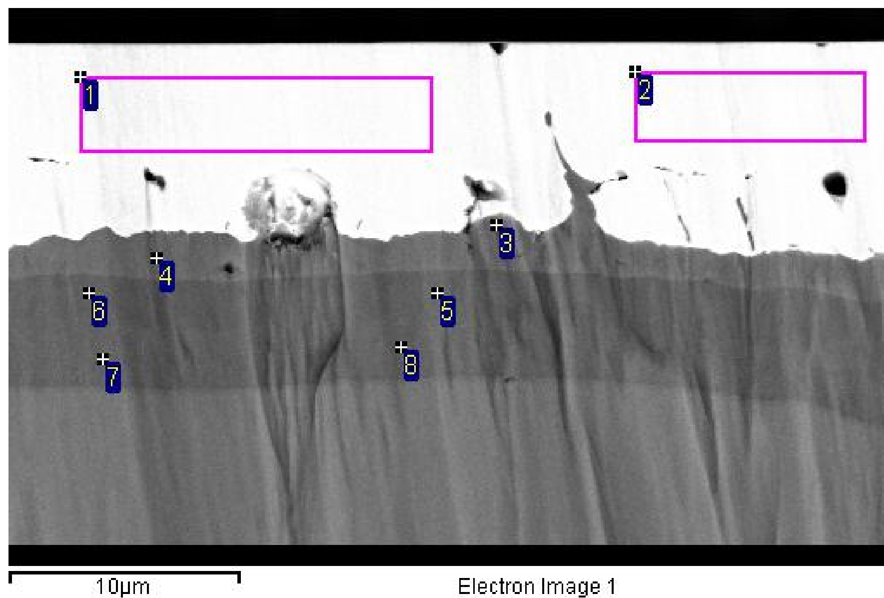


| Location | Au | Ni | Ge | P |
|---|---|---|---|---|
| 1 | 100.00 | | | |
| 2 | 100.00 | | | |
| 3 | | 74.19 | 25.81 | |
| 4 | | 75.45 | 24.55 | |
| 5 | | 77.31 | | 22.69 |
| 6 | | 76.20 | | 23.80 |
| 7 | | 84.73 | | 15.28 |
| 8 | | 84.90 | | 15.10 |

Figure 4.22 Electroless Ni:P after 3000 hours of 325°C Aging and Elemental Analysis (at.%)

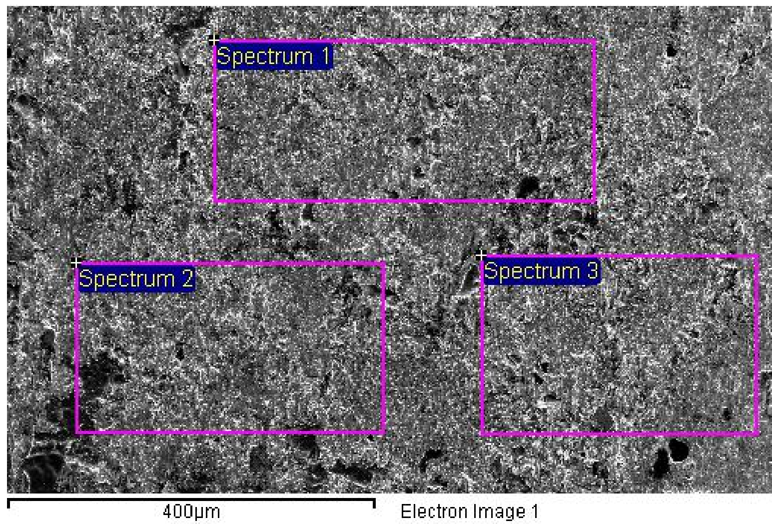


(a) Die Side

| Location | Ni | Au |
|---|---|---|
| 1 | 5.7 | 94.3 |
| 2 | 4.8 | 95.3 |
| 3 | 5.1 | 94.9 |

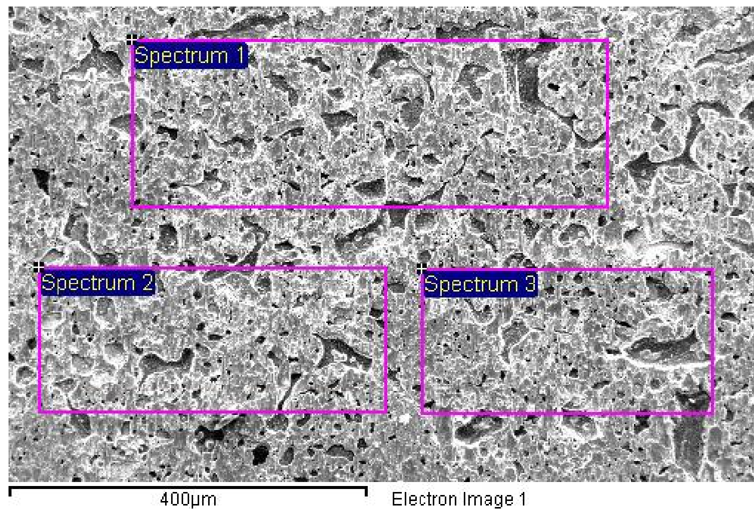


(b) Substrate Side

| Location | Ni | Ge | Au |
|---|---|---|---|
| 1 | 32.0 | 8.4 | 59.6 |
| 2 | 33.9 | 10.2 | 55.9 |
| 3 | 28.7 | 7.2 | 64.2 |

Figure 4.23 Die Shear Fracture Surfaces of AuGe on Electroless Ni:P Sample Aged for 3000 hours at 325$^{o}$C(at.%)

Figure 4.24 is a cross section and elemental analysis of a AuGe on electrolytic Ni:P sample after 3000 hours at 325°C. The cross section shows similar composition to the electroless Ni:P sample. Element analysis of the fracture surfaces (Figure 4.25) showed 3~5% Ni on the die side. The Ni (6~13%) and Ge (0~11%) content on the substrate side indicated the failure was in the Au near the Ni-Ge intermetallic.

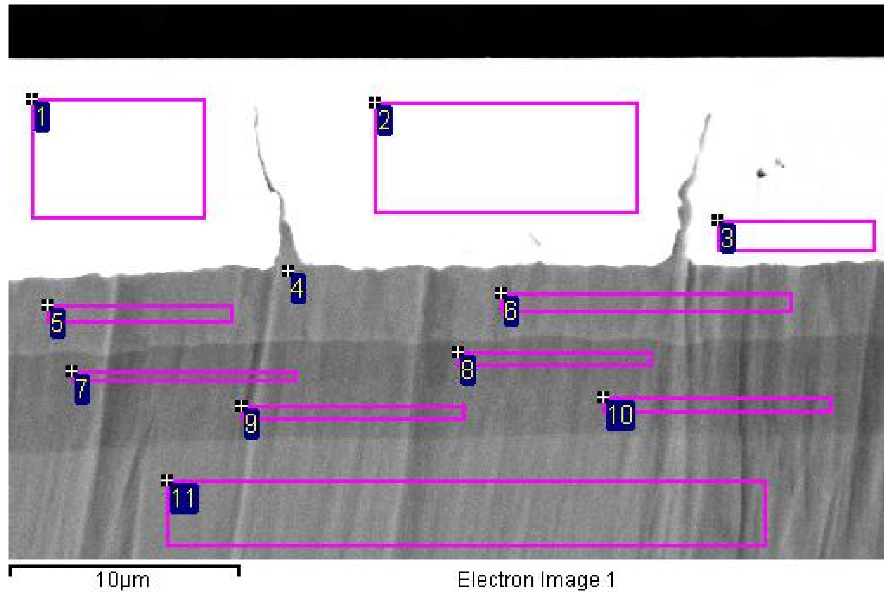


| Location | Au | Ni | Ge | P | Cu |
|---|---|---|---|---|---|
| 1 | 100.0 | | | | |
| 2 | 100.0 | | | | |
| 3 | 94.1 | 5.9 | | | |
| 4 | | 75.0 | 25.0 | | |
| 5 | | 76.0 | 24.0 | | |
| 6 | | 77.9 | 22.1 | | |
| 7 | | 75.8 | | 24.2 | |
| 8 | | 75.0 | | 25.0 | |
| 9 | | 89.4 | | 10.6 | |
| 10 | | 85.1 | | 14.9 | |
| 11 | | 1.8 | | | 98.2 |

Figure 4.24 Electrolytic Ni:P after 3000 hours of 325°C Aging and Elemental Analysis (at.%)

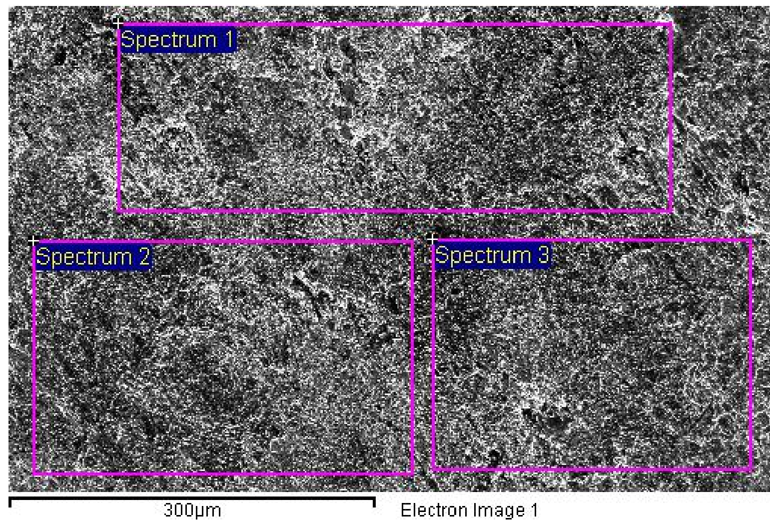


(a) Die Side

| Location | Ni | Au |
|---|---|---|
| 1 | 5.0 | 95.0 |
| 2 | 4.0 | 96.0 |
| 3 | 4.0 | 96.0 |

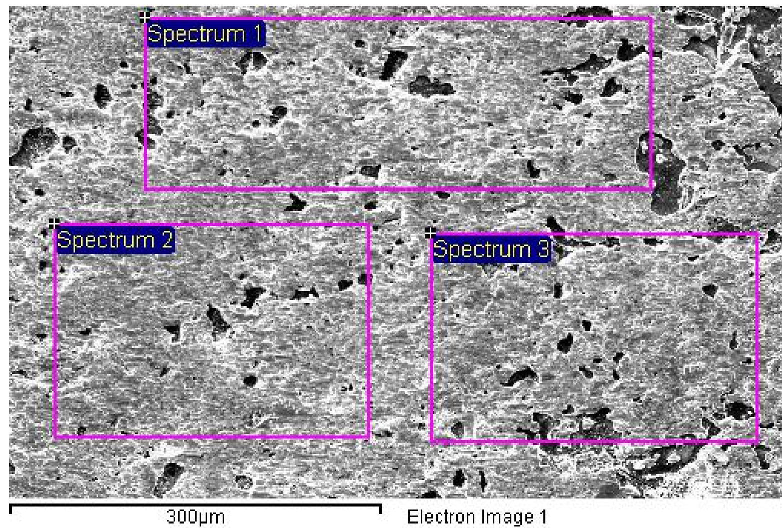


(b) Substrate Side

| Location | Ni | Ge | Au |
|---|---|---|---|
| 1 | 13.6 | 5.4 | 81.0 |
| 2 | 6.5 | | 93.5 |
| 3 | 13.7 | 7.7 | 78.6 |

Figure 4.25 Die Shear Fracture Surfaces of AuGe on Electrolytic Ni:P Sample Aged for 3000 hours at 325$^{o}$C(at.%)

## 4.7 Thermal Cycling

The experiment was conducted in a Delta 9023 oven. The temperature profile was from 300°C to -55°C. A LabView program on the computer controlled the temperature profile. Liquid nitrogen was used to cool down to -55°C. Figure 4.26 is the profile of the actual temperature in the oven measured with a thermocouple. The dwelling times at 300°C and -55°C were both 15 min. It took about 15 min to heat up to 300°C from -55°C.

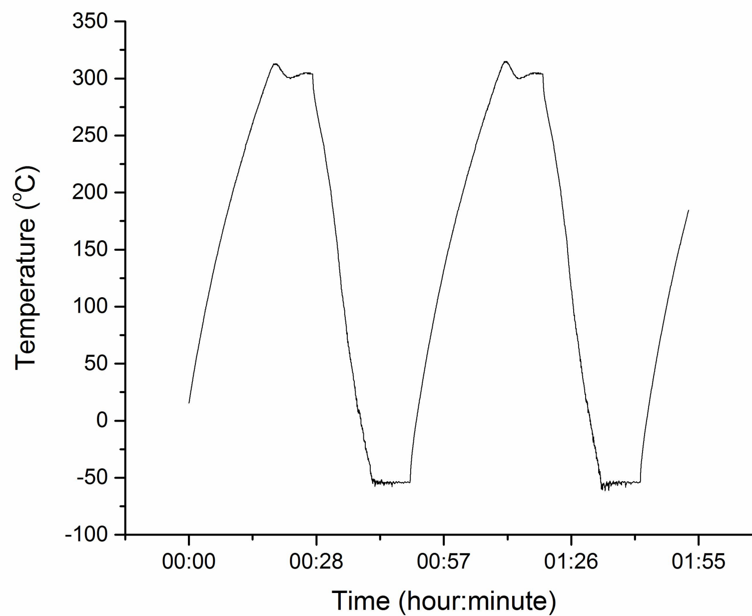


Figure 4.26 Thermal Cycling Profile

The samples were removed from the oven for shear test periodically: 100 cycles, 300 cycles, 500 cycles and 1000 cycles are evaluated. All of the samples had shear forces >100kg after 1000 cycles which means the shear strength was higher than 4kg/mm$^2$. After 1000 cycles, most of the copper was peeled off from the DBC because of the CTE mismatch (see Figure 4.27).

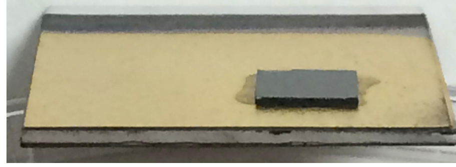

(a)

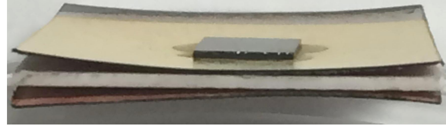

(b)

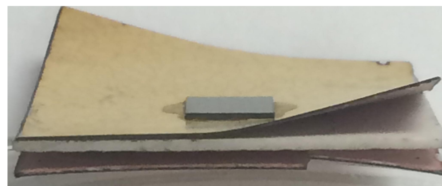

(c)

Figure 4.27 (a) DBC Substrate As-built, (b) after 500 Cycles, (c) after 1000 Cycles

4.7.1 Aging & Thermal Cycle Test

A limited number of electrolytic Ni:P samples after completing 3000 hours aging at 300$^{o}$C were thermal cycled for 500 cycles. Table 4.4 presents the shear strength. The average strength was about 1.66 kg/mm$^{2}$ lower than samples aged at 300$^{o}$C for 3000 hours but not cycled.

Table 4.4 Electrolytic Ni:P Shear Result of 3000 hours Aging at 300°C Plus 500 cycles 300°C to -55°C Compare with Electrolytic Ni:P Shear Result of 3000 hours at 300°C

| No. | Aging Plus Thermal cycle Shear Force (kg) | Aging Shear Force (kg) |
|---|---|---|
| 1 | 34.43 | 42.34 |
| 2 | 35.06 | 43.57 |
| 3 | 27.15 | 40.78 |
| 4 | 33.50 | 43.01 |
| 5 | 40.39 | 37.68 |
| 6 | 40.50 | 42.50 |
| 7 | 31.66 | 35.28 |
| 8 | 29.98 | 40.59 |
| Average shear force (kg) | 34.08 | 40.72 |
| Average shear strength ($kg/mm^2$) | 8.52 | 10.18 |

4.7.2 Cross Section and Fracture Analysis

Figure 4.28 is a cross section and element analysis of a AuGe on electrolytic Ni:P sample after 3000 hours aging at 300°C plus 500 thermal cycles from 300°C to -55°C. Location 2, 3 contain small amount of $Ni_2Ge$. Location 4, 5, 6 show that the most of the IMC layer was $Ni_3Ge$. The P ratio in the Ni layer is close to $Ni_3P$ near the IMC layer.

Figure 4.29 is the fracture surfaces and elemental analysis. On the die side, Location 1 and 2 shown ~5% Ni in Au, while at locations 3 and 4 no Ni was found. Correspondingly, on the substrate side, location 3, 4 contains more Au than location 1, 2. That may have been caused by the cracking in the die attach layer during thermal cycling.

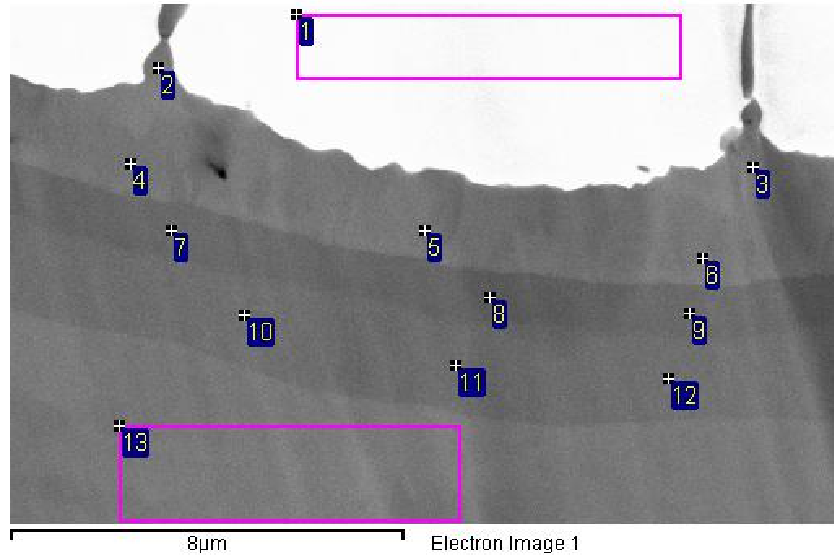


| Location | Au | Ni | Ge | P | Cu |
|---|---|---|---|---|---|
| 1 | 93.2 | 6.76 | | | |
| 2 | | 66.4 | 33.6 | | |
| 3 | | 66.9 | 33.1 | | |
| 4 | | 73.7 | 26.3 | | |
| 5 | | 75.6 | 24.4 | | |
| 6 | | 75.1 | 24.9 | | |
| 7 | | 72.1 | | 27.9 | |
| 8 | | 72.7 | | 27.3 | |
| 9 | | 72.2 | | 27.8 | |
| 10 | | 85.9 | | 14.1 | |
| 11 | | 85.5 | | 14.5 | |
| 12 | | 85.2 | | 14.8 | |
| 13 | | 1.6 | | | 98.4 |

Figure 4.28 Electrolytic Ni:P Cross Section after 3000 hours of 300°C Aging Plus 500 cycles from 300°C to -55°C and Elemental Analysis (at.%)

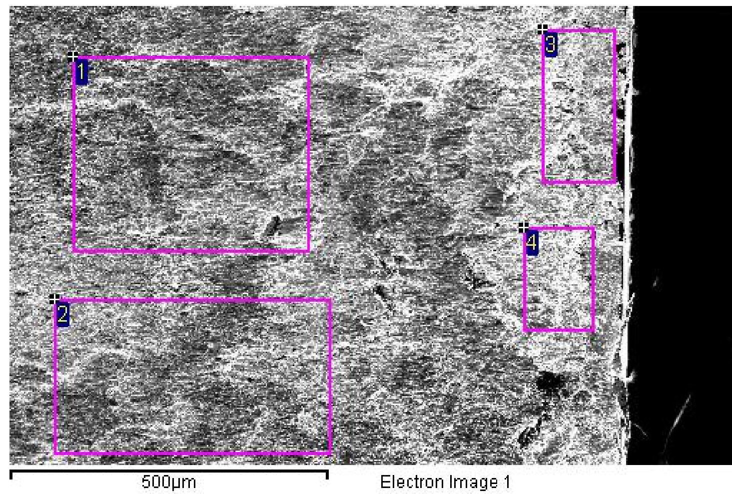


(a) Die Side

| Location | Au | Ni |
|---|---|---|
| 1 | 95.1 | 4.9 |
| 2 | 95.7 | 4.3 |
| 3 | 100.0 | |
| 4 | 100.0 | |

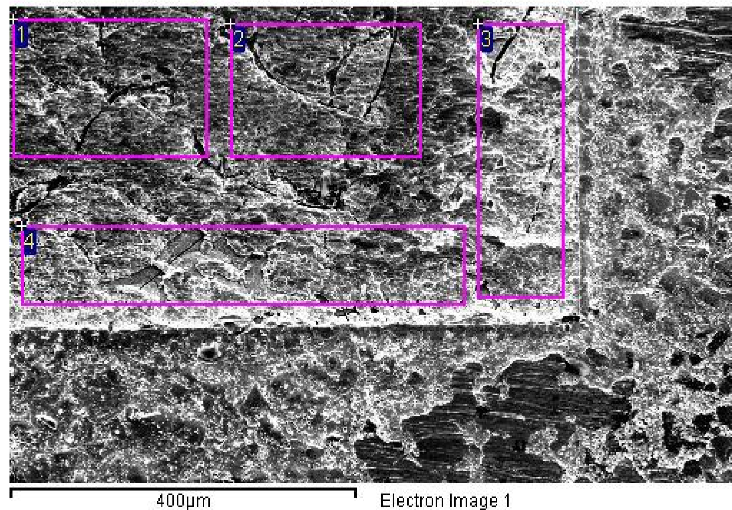


(b) Substrate Side

| Location | Au | Ni | Ge |
|---|---|---|---|
| 1 | 75.7 | 17.3 | 6.9 |
| 2 | 70.2 | 20.3 | 9.6 |
| 3 | 85.1 | 9.3 | 5.6 |
| 4 | 78.6 | 15.8 | 5.6 |

Figure 4.29 Die Shear Fracture Surfaces of AuGe on Electrolytic Ni:P Sample Aged for 3000 hours at 300$^oC$ Plus 500 cycles 300$^oC$ to -55$^oC$ (at.%)

### 4.8 Growth Kinetic of Ni-Ge IMC

The composition of the Ni-Ge IMC was determined from the cross section and elemental analysis. In order to understand the Ni-Ge IMC formation, the growth kinetics and activation energy have been studied.

The experiments were conducted at 225°C, 250°C, 275°C, 300°C for up to 900 hours. The total IMC thickness was obtained by SEM images of cross sections. 20 sampling points were collected on each sample.

From equation 4.1, the growth rate constant k, can be expressed as the slope of $W$ versus $t^{1/2}$. $W$ is the thickness of the IMC at time t.

$$W = kt^{0.5} (Eq.4.1)$$

The growth rate k can be calculated from Figure 4.30. The relationship between Ni-Ge IMC thickness and the square root of the aging time is linear when the thickness is lower than 2μm. After which the growth rate become much slower. This reduce in growth rate is likely caused by the consumption of all of the Ge in the solder. From the cross section results, the Ni-Ge intermetallic should be consistent with NiGe, $Ni_5Ge_3$, $Ni_2Ge$ and $Ni_3Ge$. The Ni ratio gradually increases by diffusion of Ni into the Ge. Since it is impossible to separate each of the Ni-Ge IMCs accurately, the kinetics and activation energy in this work were calculated for the whole Ni germanide system. The growth rate constant k in Table 4.5 was calculated from the slopes of Figure 4.30.

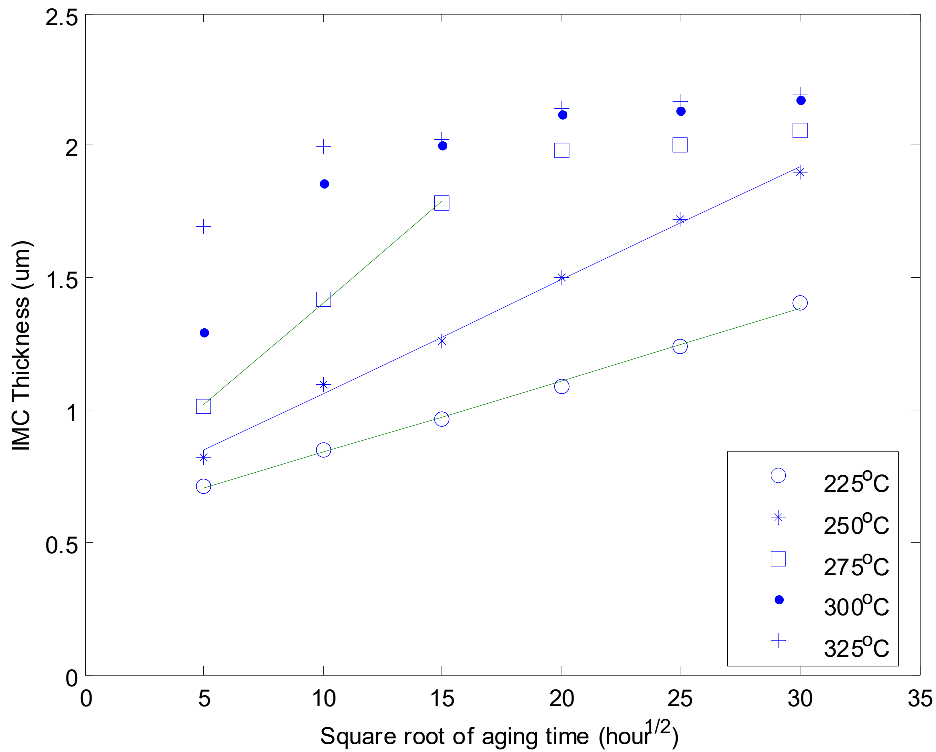


Figure 4.30 Thickness of the Ni-Ge IMC Layer Formed with Aging at 225°C, 250°C, 275°C, 300°C, and 325°C for up to 900 hours

Table 4.5 Ni-Ge IMC Growth Rate Constant

| Temperatures(°C) | k of Ni-Ge ($\times 10^{-8}$cm/s$^{1/2}$) |
|---|---|
| 225 | 4.55 |
| 250 | 7.15 |
| 275 | 12.88 |

In order to calculate the activation energy, the Arrhenius equation was used:

$$\mathrm{k}^2 = A\exp(-Q/RT)(Eq.4.2)$$

$$\ln k^2 = \ln A - (Q/RT)(Eq.4.3)$$

In the equation, $k^2$ represents the square of the growth rate, $A$ is a prefactor. T is the absolute temperature. $R$ is the universal gas constant (8.314 $\mathrm{J/K \cdot mol}$), and Q is the activation energy. The value Q can be obtained from the slope of $Ink^2$ versus $T$.

Figure 4.31 plots $Ink^2$ versus $1000/T$ for the Ni-Ge IMC. The activation energy for the Ni-Ge IMC was calculated to be 94.27 $kJ/mol$. Table 4.6 compared published activation energy results of Ni-Ge IMC. The activation energy of NiGe and $Ni_3Ge$ are relatively higher The result in this work is close to the result in [77] which also calculated the activation energy for the Ni-Ge system.

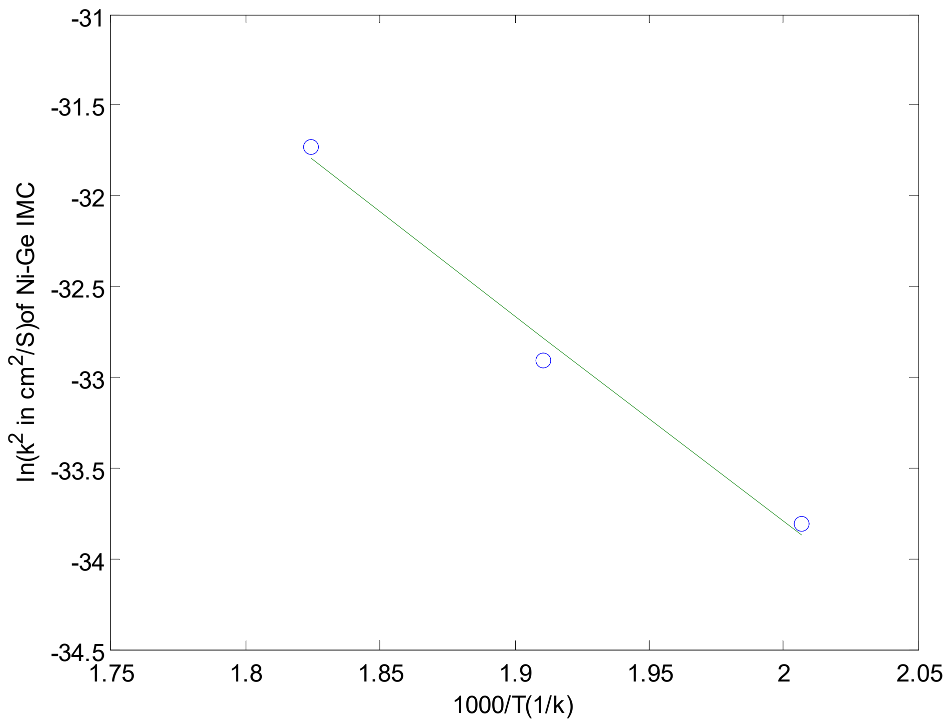


Figure 4.31 Arrhenius Plot of the Growth of Ni-Ge IMC Layers in AuGe Solder Joint on Electroless Ni:P Sample

Table 4.6 Ni Germanide Activation Energy Comparison

| IMC | Activation Energy (kJ/mol) | Reference |
|---|---|---|
| $Ni_3Ge$ | 140 | [75] |
| NiGe | 231.6~190 | [76] |
| Ni-Ge System | 107.1~70.34 | [77] |
| Ni-Ge System | 94.27 | In this work |

**4.9 Nanoindentation**

Nanoindentation is a technique used to extract elastic modulus and hardness of small volumes of material. The theory of indentation was recognized by mechanical researchers more than a century ago: the surface contact between two different materials is highly dependent on their mechanical properties [78]. Many different indentation tests and tips were invented to measure the mechanical properties of materials. The conventional indentation tests (macro or micro indentation) are limited by their large and varied tip shapes that can not measure small volume samples precisely [79].

The Berkovich tip is normally used in nanoindentation studies. Compare with other tips like Vickers, Spherical, and Rockwell, it is more readily fashioned to a sharper point than the four sided or spherical geometry thus it can control over the indentation process with more precision and accuracy [80]. Figure 4.32 is the geometry of the Berkovich tip. The face angle of the tip is $65.27^o$.

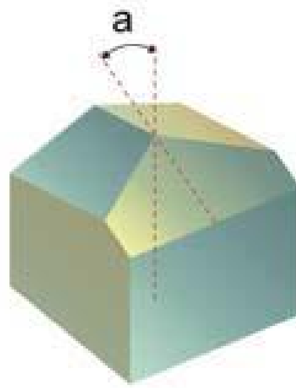


Figure 4.32 Berkovich Tip [81]

The definition of hardness can be described as a measure of how resistant a solid material is to various kinds of permanent shape change when an external force is applied to it [82]. Equation 4.4 is commonly used to describe hardness in which H is hardness, $P_{max}$ represents the maximum force applied, $A_r$ means the residual indentation area.

$$H = \frac{P_{\max}}{A_r} \quad (Eq.4.4)$$

In the traditional indentation process, the residual indentation area can be measured directly by using an optical microscope. However, in nanoindentation, the indentation area is normally a few micrometers or even nanometers which can be difficult to measured with a microscopy. As a result, in nanoindentation, the Oliver-Pharr method is normally used to calculate hardness and Young's modulus. Equation 4.4 can be written as Equation 4.5 where $A_P$ is the projected area, which can be estimated by the load-depth curve obtained from the indentation instrument (see Figure 4.33).

$$H = \frac{P_{\max}}{A_P} \quad (Eq.4.5)$$

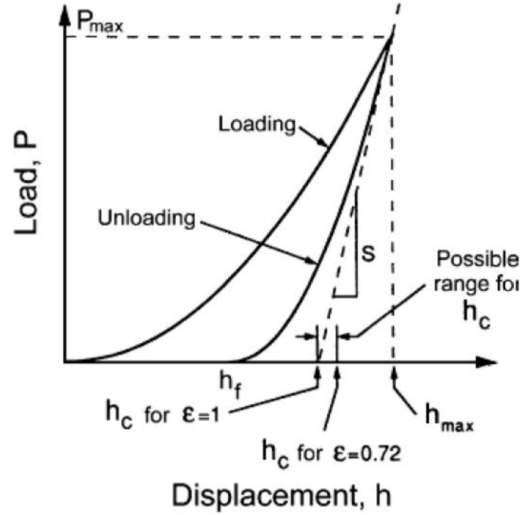


Figure 4.33 Load-displacement Curve [83]

$h_c$ is the contact depth which can be estimated by using Equation 4.6 where a constant ε is 0.75 for Berkovich tip [84]. And S is the contact stiffness which is used to describe the tendency of an object to deform along an axis when opposing forces are applied along that axis [85]. It can be calculated by Equation 4.7 . As the geometry of the tip is known, the projected area can be expressed as a function of the contact depth ($h_c$) in Equation 4.8. The value $E_r$ used in this work is reduced modulus calculated directly by the analysis software. It can be calculated using Equation 4.9 where β is a geometrical constant depending on the shape of the tip [79].

$$h_c = h_{\max} - \varepsilon \frac{P_{\max}}{S} (Eq.4.6)$$

$$S = \frac{dP}{dh} (Eq.4.7)$$

$$A_p = 3\sqrt{3} h_c \tan^2 65.3 = 24.5 h_c^2 (Eq.4.8)$$

$$E_r = \frac{1}{\beta} \frac{\sqrt{\pi}}{2} \frac{S}{\sqrt{A_p(h_c)}} (Eq.4.9)$$

The desired elastic modulus E of the material is related to the reduce modulus by Equation 4.10. ν is the Poisson's ratio of the indented material, which is usually assumed to be 0.3 if unknown; $\nu_i$ is the Poisson's ratio of the tip material which is 0.07 in this work, and $E_i$ is the elastic modulus of the tip which is 1140 GPa.

$$E = \frac{1-\nu^2}{[\frac{1}{E_r}]-[\frac{1-\nu_i^2}{E_i}]} \quad (Eq.4.10)$$

In this work, a Hysitron TI 950 nanoindenter (Minneapolis, MN, USA) with a Berkovich tip was used to acquire sample hardness and reduced Young's modulus before and after aging.

4.9.1 Results

Figure 4.34 and 4.35 are the hardness and reduced modulus for copper in electroless Ni:P sample before and after 3000 hours aging. The load force was set to 2000 μN. Six indent were proceeded for each sample surface. There was an increase in hardness after aging which corresponded to a ~5% Ni diffuse into copper in 3000 hours aged sample. However, the change of elastic modulus was not obvious. Table 4.7 presents the average hardness and elastic modulus before and after aging.

Table 4.7 Average Hardness and Elastic Modulus of Cu in the Electroless Ni:P Sample

| Cu | As-Built | 3000 Hours Aged |
|---|---|---|
| Hardness (GPa) | 1.58 | 2.07 |
| Elastic Modulus (GPa) | 133.65 | 134.89 |

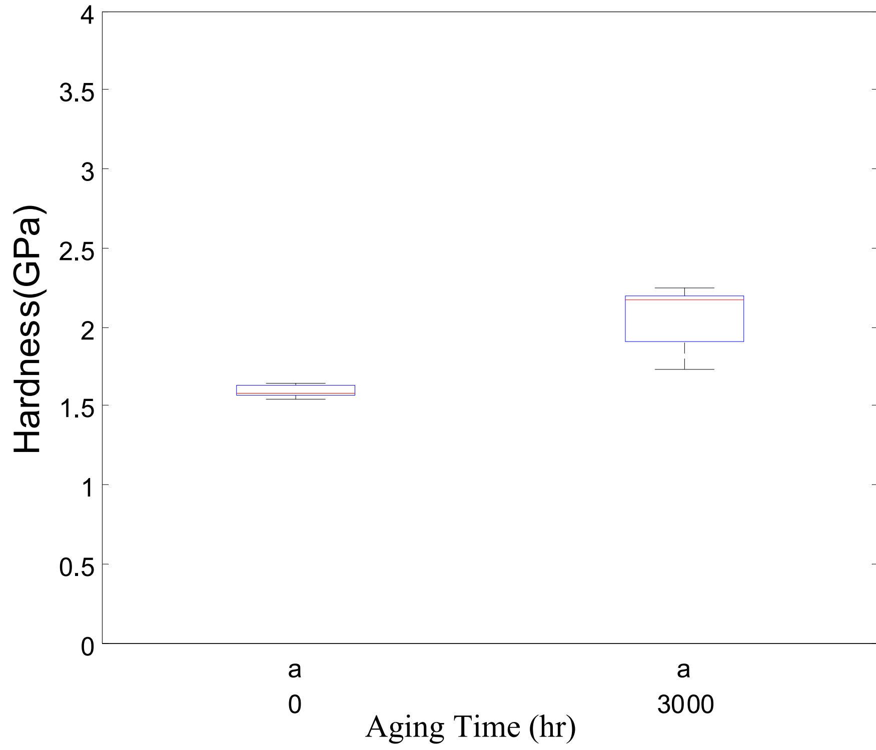


Figure 4.34 Hardness of Cu in the Electroless Ni:P Sample at Room Temperature

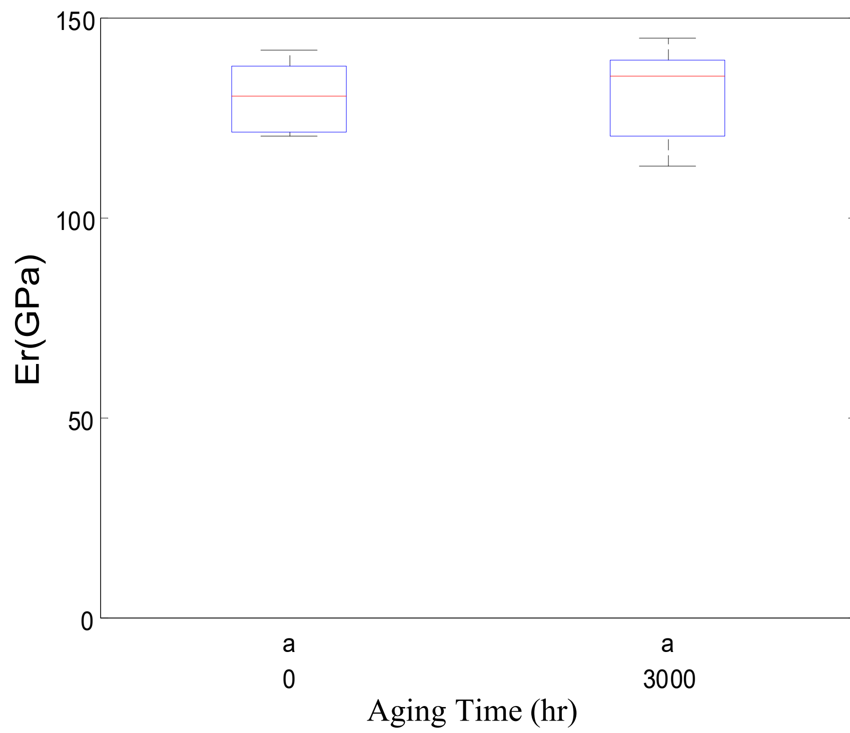


Figure 4.35 Reduced Modulus of Cu in the Electroless Ni:P Sample at Room Temperature

Figures 4.36 and 4.37 are the hardness and reduced modulus box plot of the electroless and electrolytic Ni:P layer before and after 3000 hours aging at 300$^{o}$C. The load force was set to 12000 μN during the test. The hardness of the electroless Ni:P was about 1 GPa higher than that of the electrolytic Ni:P. After aging, the hardness and the elastic modulus changes in the electroless Ni:P layer were not obvious. While the electrolytic Ni:P had about a 1 GPa decrease in hardness and 42 GPa decrease in the elastic modulus (see Table 4.8). Many researchers reported that long-term high temperature aging may decrease a material's hardness and modulus [86, 87, 88]. In this case, the electrolytic plated Ni:P was found more sensitive to high temperature aging than the electroless plated Ni:P.

Table 4.8 Average Hardness and Elastic Modulus of Ni:P Layer

| Electroless Ni:P | As-Built | 3000 Hours Aged |
|---|---|---|
| Hardness (GPa) | 12.42 | 12.43 |
| Elastic Modulus (GPa) | 189.41 | 182.26 |
| Electrolytic Ni:P | As-Built | 3000 Hours Aged |
| Hardness (GPa) | 11.61 | 10.56 |
| Elastic Modulus (GPa) | 195.00 | 152.90 |

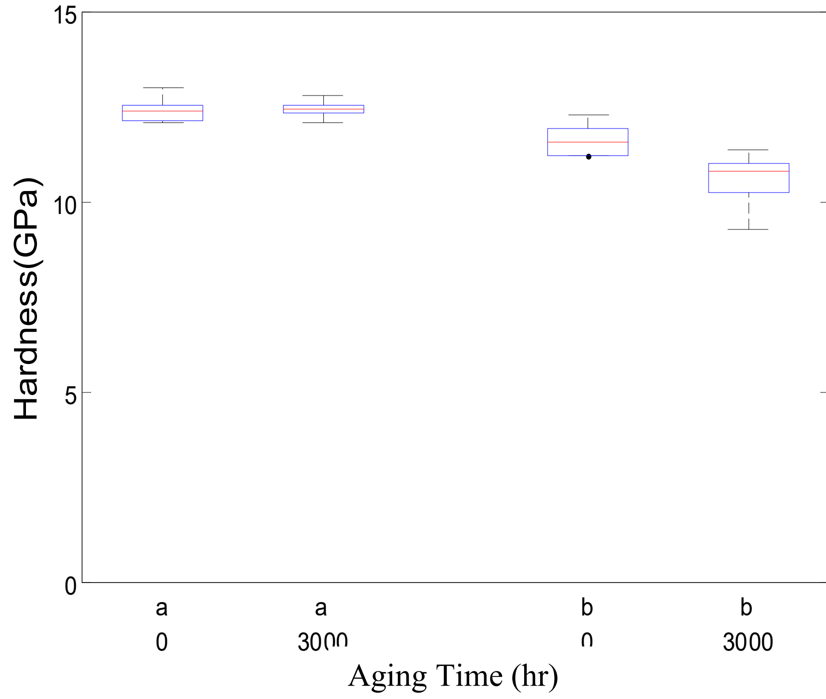


Figure 4.36 Hardness of Ni:P Layer at Room Temperature (a) AuGe on Electroless Ni:P (b) AuGe on Electrolytic Ni:P

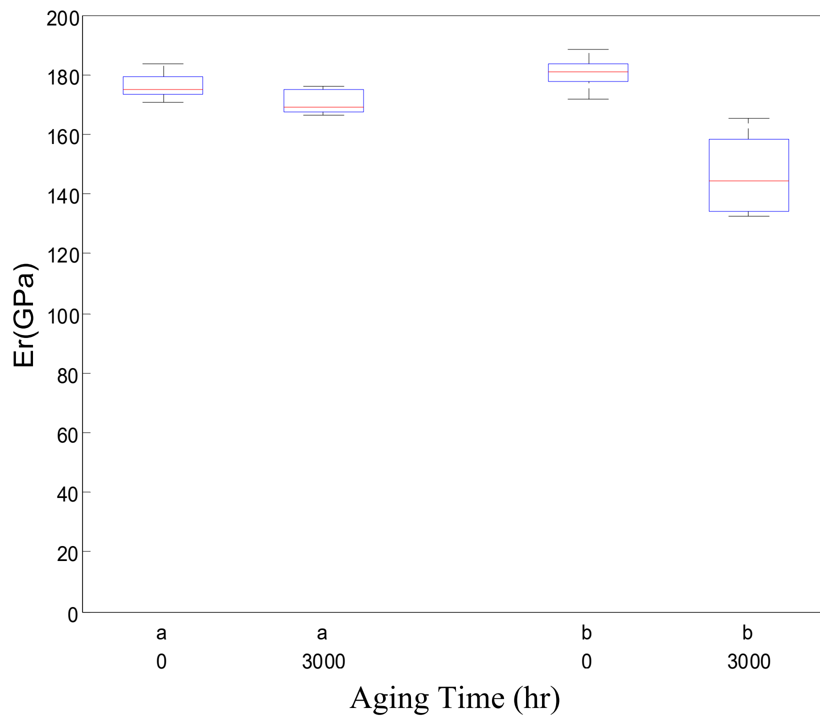


Figure 4.37 Reduced Modulus of Ni:P Layer at Room Temperature (a) AuGe on Electroless Ni:P (b) AuGe on Electrolytic Ni:P

Figures 4.38 and 4.39 are the hardness and reduced modulus box plots of Ni-Ge IMC on the electroless and electrolytic plated Ni:P sample. The nanoindentation tests were done on the 3000 hours aged samples, since the IMC had growth thick enough to get the consistent results. The load force used in this test was 3000 μN. The hardness of Ni-Ge IMC on the electroless sample was about 3 GPa higher than that on the electrolytic sample, which is questionable. It is highly suspected the result may have been influenced by the Ni:P layer under the IMC layer. To get more accurate nanoindentation result for the Ni-Ge IMC, lower load force such as 100 μN or 50 μN should be used in the future studying.

Table 4.9 Average Hardness and Elastic Modulus of Ni-Ge IMC Layer

| Ni-Ge IMC | Electroless Ni:P<br>3000 Hours Aged | Electrolytic Ni:P<br>3000 Hours Aged |
|---|---|---|
| Hardness (GPa) | 13.12 | 9.902 |
| Elastic Modulus (GPa) | 296.31 | 141.98 |

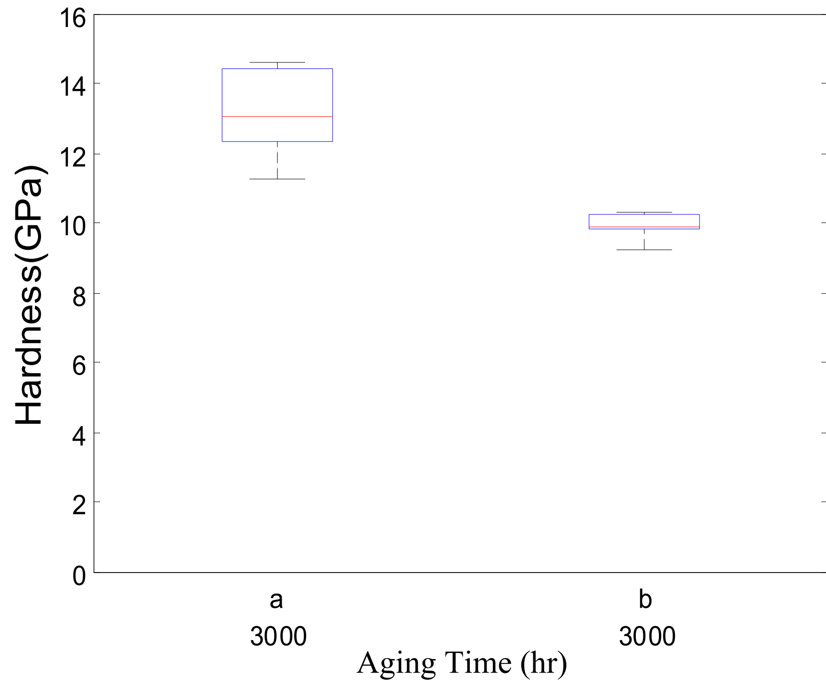


Figure 4.38 Hardness of Ni-Ge IMC at Room Temperature after 3000 hours Aging at 300°C (a) AuGe on Electroless Ni:P (b) AuGe on Electrolytic Ni:P

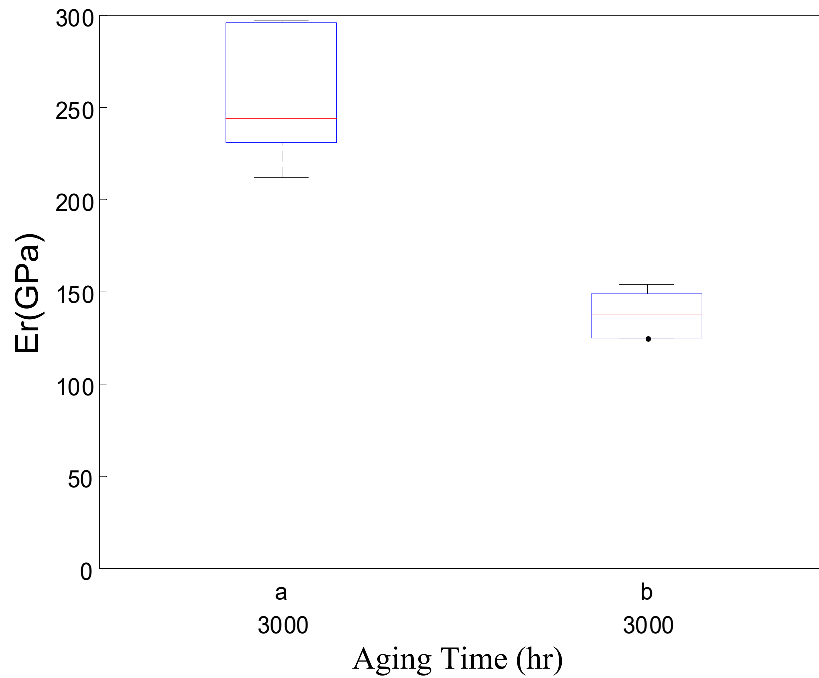


Figure 4.39 Reduced Modulus of Ni-Ge IMC at Room Temperature after 3000 hours Aging at 300°C (a) AuGe on Electroless Ni:P (b) AuGe on Electrolytic Ni:P

Table 4.10 compared the nanoindention results from other publications. The hardness and elastic modulus of copper are close to the results reported by other researchers. However, the results of the Ni:P layer are higher than that these reported value. It is suspected that the assembly process may cause this difference since the short term high temperature treatment (normally 1 hour at 350°C or higher) can increase the hardness of Ni:P layer dramatically [94]. Normally, at least sixteen well-spaced indents need to be performed for each position [95,96,97]. However, the number of indentation for each data point was six in this work which is not large enough to draw any firm conclusion. Additional data and further study are needed.

Table 4.10 Comparison of the Data Obtained in the Present Study

| Phase Indented | Hardness (GPa) | Elastic Modulus (GPa) | Reference |
|---|---|---|---|
| Cu | 1.58 | 133.65 | Current Study |
| Cu | 2.07 | 134.89 | Current Study |
| Cu | - | 116.5 ± 4.7 | [89] |
| Cu | 2.01 ± 0.42 | 108.72 ± 4.12 | [90] |
| Cu | 2.16 ± 0.19 | 110.8 ± 3.8 | [91] |
| Electroless Ni-P | 12.42 | 189.41 | Current Study |
| Electroless Ni-P | 6.1-8.2 | 146-168 | [92] |
| Electroless Ni-P | 6.5 | 130 | [93] |
| Electrolytic Ni-P | 11.61 | 195.00 | Current Study |
| Electrolytic N-P | 7.74–8.57 | - | [94] |

### 4.10 Summary

AuGe die attach on electroless and electrolytic Ni:P platings were evaluated by 300°C high temperature storage test and thermal cycling test ranging from -55°C to 300°C. The shear strength had a 30% decrease on both of them after 3000 hours aging, which was still higher than 9kg/mm$^2$. The decrease might be caused by the Ni diffusion into the Au. The formation of Ni-Ge IMC during the assemble and aging process was studied which should be consistent with NiGe,

$Ni_5Ge_3$, $Ni_2Ge$ and $Ni_3Ge$. The Ni ratio gradually increases by diffusion of Ni into the Ge. Meanwhile, voiding was observed in as-built electroless Ni:B and electrolytic Ni samples.

# CHAPTER 5 CONCLUSION AND FUTURE WORK RECOMMENDATION

## 5.1 High Temperature Electronic Coating

Parylene HT and Duraseal 1531 have been evaluated as potential candidates for electronic encapsulation at 300°C. Both Parylene HT and Duraseal 1531 on as-built samples passed 5000 V breakdown tests conducted at 300°C . However, after 2000 hours aging at 300°C, the Parylene HT was observed to peel off from the substrate surface. Adhesion tests were conducted for Parylene HT on both electroplated gold and one side polished AlN substrate surfaces. The result showed that Parylene HT adhesion strength on AlN was slightly higher than that on the electroplated gold surface, however, both of them failed after 2000 hours aging at 300°C. The FTIR and AFM results of Parylene HT revealed that there was no significant difference between the as-built and the aged sample. It is suspected the adhesion promoter used with Parylene HT decomposed at 300°C. Duraseal 1531 silicone material did not suffer any adhesion problems and still provided reliable insulation after 2000 hours aging.

In conclusion, Parylene HT cannot be used for 2000 hours application at 300°C, as it lost adhesion to the substrate. And Duraseal 1531 is a reliable silicone encapsulant material at 300°C.

## 5.2 BiAgX on Nickel Plating

The use of BiAgX solder on different nickel platings has been studied through high temperature storage (200°C) and thermal cycling experiments (-55°C-195°C). The alloy was used to assemble SiC die to the Ni/Au finished DBC substrates. The nickel platings included electroless Ni:P, electrolytic Ni:P, Ni and Ni:Co. The X in BiAgX is Sn which formed Ni-Sn and

(AgAu)-Sn IMCs in the electroless Ni:P, electrolytic Ni:P and Ni samples. Ni-Sn and Ag-Sn IMCs were observed in Ni:Co samples which did not have Au on Ni plating .

For the electrolytic Ni:P plating, no $NiBi_3$ IMC was formed during the aging and thermal cycling test. The shear results are relatively higher than other Ni platings in the aging test and similar to electroless Ni:P in the thermal cycling test. The fracture surfaces are in the solder near the Ni:P layer.

For the die attach on the electroless Ni:P plating, the Ni:P layer was observed to spall off from the copper after aging. $NiBi_3$ was formed on both sides of the Ni:P layer. The failure was near the spalled Ni:P-to-$NiBi_3$ and Ni-Sn intermetallic interface along the top side of the Ni:P layer. In thermal cycling test, the Ni:P spalling phenomenon was not observed in large areas and the failure was also in the solder near the Ni:P layer which corresponded to similar shear strength to the electrolytic Ni:P.

For the electrolytic pure Ni finish, the formation of $NiBi_3$ consumed all of the Ni layer during the aging and thermal cycling test which caused the decrease in shear strength. The aging sample failure was along the Bi to $NiBi_3$ interface. In the thermal cycling samples, the fracture surfaces were also found partially in the $NiBi_3$ near the copper.

For the electrolytic Ni:Co plating, the formation of $NiBi_3$ also consumed all of the Ni. However, the $NiBi_3$ was observed completely peel off from the copper surfaces during shear testing after aging, which resulted in the lowest shear strength among these Ni platings in both aging and thermal cycling tests.

To sum up, electrolytic Ni:P plating is more compatible with BiAgX solder die attach No IMC was formed during the assembly and aging process. Although the shear strengths decreased

in all of these Ni plating samples, they were still much higher than the requirements of MIL-STD-883, Method 2019.7 after high temperature storage and thermal cycling.

**5.3 AuGe on Nickel Plating**

The use of AuGe preform on different nickel platings has been evaluated. The shear strength of AuGe on the as-built electroless Ni:B and the electrolytic Ni samples are much lower than that on the electroless and the electrolytic Ni:P plating. The Ni-Ge IMCs were formed during the assembly process. Voids were formed along the Ni-Ge IMCs to the Ni layer, which caused the low shear strength of the electrolytic Ni samples.

High temperature storage tests at 300$^{o}$C, 325$^{o}$C and thermal cycling experiments ranging from -55$^{o}$C to 300$^{o}$C were performed on the electroless and electrolytic Ni:P samples. After 3000 hours aging, the shear strength of both electroless and electrolytic Ni:P decrease about 30% at both 300$^{o}$C and 325$^{o}$C The mechanical fractures of the aged samples were similar, and were in the gold bulk near to the Ni-Ge IMCs. From the EDS results, the Ni-Ge IMCs was consistent with NiGe, $Ni_5Ge_3$, $Ni_2Ge$, and $Ni_3Ge$. The Ni ratio gradually increased by diffusion of Ni into the Ge.The growth kinetics of Ni-Ge have also been calculated to be 94.27 kJ/mol. No thermal cycling sample (5 mm × 5 mm die) could be sheared after 1500 cycles.

In summary, the electroless and electrolytic Ni:P platings are good surface finishing for AuGe die attachment, which can provide high and stable shear strength at 300$^{o}$C.

**5.4 Future Work Recommendation**

Based on the results and analysis presented in this dissertation, there are some recommendations for future work as follows:

- For Parylene HT coating used as a conformal coating material, a high temperature stable adhesion promoter should be explored.

● Besides BiAgX paste and AuGe preform, other die attach materials can be explored. For example, AuSn liquid phase transient bonding, which can fulfill applications higher than 400$^{o}$C and would form Ni-Sn-Au IMC on Ni plating surface should be studied.

● There are some Ni platings other than those used in this work that should be evaluated. For example, Ni:P:W is a new ternary Ni plating which is claimed have better high temperature performance than traditional Ni platings [98].

## REFERENCE

[1] R. Mishra, M. Keimasi, and D. Das, “The Temperature Ratings Of Electronic Parts,” Electronics Cooling, Vol. 10, No.1, pp. 20-29, Feb.2004.

[2] F. P. McCluskey, R. Grzybowsky, and T. Podlesak, “High Temperature Electronics, ”CRC-Press, pp. 2-2 , Feb. 1997.

[3] “How Does Measurement-While-Drilling (MWD) Work?,” retrieved July 13th, 2016, http://www.rigzone.com/training/insight.asp?insight_id=296&c_id=1

[4] G. W. Hunter, R. S. Okojie , P. Neudeck, G. Beheim, G. Ponchak, G. Fralick, J. Wrbanek, L. Chen “ High Temperature Electronics, Communications & Supporting Technologies For Venus Mission,” Electrical and Electronic Engineering , pp. 27 – 30, 2006.

[5] J. Watson, G. Castro, “A Review of High-Temperature Electronics Technology and Applications,” J. Mater. Sci. Mater. Med, 26 , pp. 9226–9235, 2015.

[6] R. W. Johnson, P. Zheng, A. Wiggins, S. Rubin and L. Peltz, “High Temperature Electronics Packaging,” HITEN, College Oxford, England, September17-19, 2007.

[7] Phillip E. Henson, “Considerations and Options for High Temperature Die Attach,” M.S. thesis, Dept. Elect. Eng, Auburn Univ., Auburn, AL, 2010.

[8] R. Kirschman, “High Temperature Electronics,” Wiley-IEEE Press, August 18, 1998.

[9] P. L. Dreike, D. M. Fleetwood, D. B. King, D. C. Sprauer and T. E. Zipperian, “An Overview of High Temperature Electronic Device Technologies and Potential Applications,” IEEE Trans. Compon. Packag. Manuf. Technol. A, Volume:17, Issue: 4, Dec. 1994.

[10] “Electronic Packaging,” Retrieved July 22th, 2016,
http://www.dictionaryofengineering.com/definition/electronic-packaging.html

[11] L.A. N. Melchor, “Evaluation of Die Attach Materials for High Temperature Power Electronics Application and Analysis of the Ag Particles Sintering,” Ph.D. dissertation, UBA, Barcelona, Spain, pp14.

[12] B. Ozpineci and L. M. Tolbert, “Comparison of Wide-bandgap Semiconductors for Power Electronics Applications,” Oak Ridge Nat. Lab., U.S. Dept. Energy, Rep. 4/5, Dec. 2003.

[13] P. G. Neudeck, R. S. Okojie, L. Chen, “High-Temperature Electronics- A Role for Wide Bandgap Semiconductors?,” Proc. IEEE, Volume 90, Issue:6, 2002.

[14] “SiC Physical & Electronic Properties,” retrieved July 13th, 2016,
http://www.cree.com/products/sic_sub_prop.asp

[15] P .G. Neudeck, “Silicon Carbide Electronic Devices,” Encyclopedia of Materials:Science and Technology, Elsevier Ltd, pp. 8508-8519, 2001.

[16]V. R. Manikam and K. Y. Cheong, “Die Attach Materials for High Temperature Applications: A Review,” IEEE Trans. Compon. Packag. Manuf. Technol, Vol. 1, No. 4, Apr. 2011.

[17] H. Zhang and N. Lee, “High Reliability High Melting Lead-free Mixed BiAgX Solder Paste System,” International Symposium on Microelectronics, San Diego, CA, September 9-13, 2012.

[18] Z. Shen, Johnson, R.W., Hamilton, M.C., “SiC Power Device Die Attach for Extreme Environments,” IEEE Trans. Electron Devices, Vol. 62, No. 2, pp. 346 - 353, Feb. 2015.

[19] P. Zheng, A. Wiggins, R. W. Johnson, R. V. Frampton, S. J. Adam, and L. Peltz, “Die Attach for High Temperature Electronics Packaging,” Int. High Temperature Electron. Conf., Albuquerque, NM, pp. 1 – 6, May 2008.

[20] W. D. MacDonald and T. W. Eagar, “Transient Liquid Phase Bonding,” Anna. Review Material. Science, pp. 22:23-46, 1992.

[21] R. W. Johnson and J. Williams, “Power Device Packaging Technologies for Extreme Environments,” 2005 IEEE Aerospace Conference, Big Sky, MT, 2005, pp. 1-6.

[22] Göbl, C. and Faltenbacher, J., “Low Temperature Sinter Technology Die Attachment for Power Electronic Applications,” Int. Conf. on Integrated Power Electronics Systems (CIPS), March 16-18, 2010 pp. 1-5.

[23] F. Yu, R. W. Johnson and M. C. Hamilton, “Pressureless Sintering of Microscale Silver Paste for 300°C Applications,” IEEE Trans. Compon. Packag. Manuf. Technol, Vol. 5, No. 9, pp. 1258-1264, Sept. 2015.

[24] J. L. Hudgins, G.S. Simin, E. Santi, M. A. Khan, “An Assessment of Wide Bandgap Semiconductors for Power Devices,” IEEE Trans. Power Electron., Vol. 18, No. 3, pp. 907, May 2003.

[25] L. Dupont, Z. Khatir, S. Lefebvre, and S. Bontemps, “Effects of Metallization Thickness of Ceramic Substrates on the Reliability of Power Assemblies Under High Temperature Cycling,” Microelectron. Reliab., Vol. 46, No. 9 – 11, pp. 1766 – 1771, Sept.-Nov. 2006.

[26] “What is a Surface Finish,” retrieved July 13th, 2016,
http://frontiermaterials.net/teaching/surface_finish_new_2011.pdf

[27] “Menu Metal Properties,” retrieved July 13th, 2016,
http://www.tibtech.com/conductivity.php

[28] M. Myers, “Overview of the Use of Silver in Connector Applications,” TEC 503-1016. (http://www.te.com/documentation/whitepapers/pdf/Ag_use_conn ectors_503-1016.pdf)

[29] P.A. Konodos, “ENEPIG: the Universal Finish?,” AREA Consortium Meeting, Oct. 2009.

[30] M.N. Islam, Y.C. Chan, A. Sharif, M.O. Alam, "Comparative Study of the Dissolution Kinetics of Electrolytic Ni and Electroless Ni-P by the Molten Sn3.5Ag0.5Cu Solder Alloy," Microelectronics Reliability ,43:2031 – 2037, 2003.

[31] "Electroless Nickel", retrieved July 13th, 2016, https://en.wikipedia.org/wiki/Electroless_nickel

[32] Glenn O. Mallory, "Chapter 1 The Fundamental Aspects Of Electroless Nickel Plating," in Electroless Plating: Fundamentals and Applications, William Andrew Publishing, pp. 1-57, 1990.

[33] Y. Zou, Y. Chen, L. Cheng, W. Liu, "Effect of Tin Addition on the Properties of Electroless Ni-P-Sn Ternary Deposits," Materials Trans., Vol. 51, No. 2, pp. 277-281, 2010.

[34] "Electroless Nickel Plating," retrieved July 13th, 2016, http://www.chemprocessing.com/page.asp?pageid=61&

[35] "Electroless Nickel Plating as a Brazing Filler Metal," retrieved July 13th, 2016, http://vacaero.com/information-resources/vacuum-brazing-with-dan-kay/1493-electroless-nickel-plating-as-a-brazing-filler-metal.html

[36] K. G. Keong, W. Sha, S. Malinov, "Crystallization and Phase Transformation Behaviour of Electroless Nickel-phosphorus Deposits with Low and Medium Phosphorus Contents Under Continuous Heating," J. of Materials Science, . 37:4445- 4450, 2002.

[37] K.G Keong, W Sha, S Malinov, "Crystallisation Kinetics and Phase Transformation Behavior of Electroless Nickel-phosphorus Deposits with High Phosphorus Content," J. of Alloys and Compounds, Vol 334, Issue 1-2, pp. 192-199, Feb. 2002.

[38] E. Bredael, B. Blanpain, J. P. Celis and J. R. Roos, "On the Amorphous and Crystalline State of Electrodeposited Nickel-Phosphorus Coatings," J. of the Electrochemical Society, Vol. 141, Issue 1, pp. 294-299, 1994.

[39] J. Yoon, B. Noh, S. Jung, “Mechanical Reliability of Sn-Ag BGA Solder Joints With Various Electroless Ni-P and Ni-B Plating Layers,” IEEE Trans. Compon. Packag. Manuf. Technol, Vol. 33, No. 1, pp. 222-228, Mar. 2010.

[40] R. Wayne Johnson, et al., “Power Device Packaging Technologies for Extreme Environments,” IEEE Trans. Electron. Packag. Manuf., Vol. 30, No. 3, pp.182-193, July 2007

[41] “What is conformal coating?,” retrieved July 13th, 2016, http://www.humiseal.com/conformal-coating/

[42] “Parylene CVD Operating Instructions,” retrieved July 13th, 2016, https://www.bioinformatics.purdue.edu/discoverypark/nanotechnology/facilities/manuals/Parylene-manual.pdf

[43] “Parylene Deposition Process,” retrieved July 13th, 2016, http://scscoatings.com/what-is-parylene/parylene-deposition/

[44] “Techsil Increases its Conformal Coating Solutions with an Inventive Material from Momentive,” retrieved July 13th, 2016, http://www.techsil.co.uk/press/conformalcoating/

[45] “Potting & Encapsulation,” retrieved July 13th, 2016, http://www.electroniccoating.com/our-services/potting-encapsulation/

[46] “Encapsulation & Potting Resins,” retrieved July 13th, 2016, http://www.protavicamerica.com/products/encapsulation/

[47] “Parylenes,” retrieved July 13th 2016, http://www.google.com/patents/EP2729194A1?cl=en

[48] “Parylene Properties,” retrieved July 13th, 2016, http://www.physics.rutgers.edu/~podzorov/parylene%20properties.pdf

[49] B. Tung, et al., "Investigation of Low-temperature Deposition High-uniformity Coverage Parylene-HT as a Dielectric Layer for 3D Interconnection," Proc. IEEE Electronic Compon. and Technol. Conf. (ECTC), pp. 1926-1931, May 27-30, 2014.

[50] "Silicone," retrieved July 13th, 2016, https://en.wikipedia.org/wiki/Silicone

[51] "Data sheet of 1531," retrieved July 13th, 2016, http://www.cotronics.com/vo/cotr/pdf/1531.pdf

[52] "FTIR," retrieved July 13th, 2016, http://chem.libretexts.org/Core/Physical_and_Theoretical_Chemistry/Spectroscopy/Vibrational_Spectroscopy/Infrared_Spectroscopy/How_an_FTIR_Spectrometer_Operates

[53] "Chemical Bonds," retrieved July 13th, 2016, http://www2.ups.edu/faculty/hanson/Spectroscopy/IR/IRfrequencies.html

[54] "AFM," retrieved July 13th, 2016, https://en.wikipedia.org/wiki/Atomic-force_microscopy

[55] H. Zhang and N. Lee, "High Reliability High Melting Lead-Free Mixed BiAgX Solder Paste System," International Symposium on Microelectronics, San Diego, CA,Sept. 9-13, 2012.

[56] J. N. Lalena, N. F. Dean, and M. W. Weiser, "Experimental Investigation of Ge-Doped Bi-11Ag as a New Pb-Free Solder Alloy for Power Die Attachment," J. of Electronic Materials, Vol. 31, No. 11, 2002.

[57] "Ag-Bi Phase Diagram," retrieved July 13th, 2016, http://www.metallurgy.nist.gov/phase/solder/agbi.html

[58] Z. Shen, K. Fang, Johnson, R.W.; Hamilton, M.C., "Characterization of BiAgX Solder for High Temperature SiC Di7e Attach, Components," IEEE Trans.Packag. and Manuf. Technol., Vol. 4, No. 11, pp. 1778 - 1784, Nov. 2014.

[59] "Bi-Cu Phase Diagram," retrieved July 13th, 2016, http://www.metallurgy.nist.gov/phase/solder/bicu.html

[60] "Bi-Sn Phase Diagram," retrieved July 13th, 2016, http://www.metallurgy.nist.gov/phase/solder/bisn.html

[61] M.S. Lee, "Interfacial Reactions Between Ni Substrate and the Component Bi in Solders and the Component Bi in Solders," J. of Electronic Materials, Vol. 28, No. 1, 1999.

[62] Chachula, M. et al. "Interaction of BiAg11 Solder with Cu, Ag and Ni Substrate," Annals of DAAAM and Proceedings of DAAAM Symposium, Vol. 22, No. 1, Vienna, Austria, 2011, pp. 1009-1010.

[63] "Bi-Ni Phase Diagram," retrieved July 13th, 2016, https://sites.google.com/site/atdinsdale/bi-ni

[64] "Ni-Sn Phase Diagram," retrieved July 22 2016, http://www.himikatus.ru/art/phase-diagr1/Ni-Sn.php

[65] "Physical properties of AuGe12," retrived July 13th, 2016, http://www.indium.com/solders/gold/

[66] "Au-Ge Phase Diagram," retrived July 13th, 2016, http://www.himikatus.ru/art/phase-diagr1/Au-Ge.php

[67] V. Chidambaram et al. "High Reliability Gold Based Solder Alloys for Micro-electronics Packaging for High Temperature Applications," Proc. IEEE Int. Symp. Phys. Failure Anal. Integr. Circuits Conf., pp. 1-6, 2012.

[68] V. Chidambaram, "Reliability of Au-Ge and Au-Si Eutectic Solder Alloys for High-Temperature Electronics," J. of Electronic Materials, Vol. 41, No. 8, 2012.

[69] Lang, F. and Sato, H., “Package Reliability of the SiC Power Modules in harsh Environments,” Int. Conf. & Exhi. on High Temperature Electronics Network, Oxford, UK, pp. 139-144, July 18-20, 2011.

[70] Tanimoto, S. et al., “Assesment of Au-Ge Die Attachment for an extended Junction Temperature Range in Power Applications,” Int. Conf. & Exhi. on High Temperature Electronics Network, Albuquerque, NM, May 11-13, 2010. pp. 32-39.

[71] M. J. Palmer and R. W. Johnson, “Thick Film Modules for 300$^{o}$C Applications,” International High Temperature Electronics Conference, Santa Fe, NM, May 16-18, 2006, pp. 118-124.

[72] “Ni-Cu Phase Diagram,” retrived July 13th, 2016, http://www.slideshare.net/daphiny/diagramas-de-equilibrio-13971943

[73] “Ni-Au Phase Diagram,” retrived July 13th,” retrived July 13th, 2016, http://www.himikatus.ru/art/phase-diagr1/Au-Ni.php

[74] “Ni-Ge Phase Diagram,” retrived July 13th, 2016, http://www.himikatus.ru/art/phase-diagr1/Ge-Ni.php

[75]. K. Aoki et al., “Ordering of Chemically Disordered $Ni_3A1$ and $Ni_3Ge$ Prepared by Mechanical Alloying,” Materials Science and Engineering, A 179/A 180 (1994) 39(I-395).

[76] Q. Zhang et al., “Formation and Thermal Stability of Nickel Germanide on Germanium Substrate,” Japanese Journal of Applied Physics, Vol. 44, Part 2, pp. 42-45.

[77] J. Lee, J. Bae, T. Kim, H. Kim, S. Min, K. Shin, J. Lee, J. Song, and C. Yang, “Kinetics of the Ni/Ta-Interlayer/Ge Reactions Studied by In Situ Transmission Electron Microscopy,” Science of Advanced Materials, Vol. 7, pp. 1497-1501, 2015.

[78] C.A. Schuh, "Nanoindentation Studies of Materials," Materials Today, Vol. 9, Issue 5, pp. 32-40, May 2006.

[79] "Nanoindenation," retrived July 13th, 2016, https://en.wikipedia.org/wiki/Nanoindentation

[80] Fischer-Cripps, Anthony C, "Nanoindentation," Mechanical Engineering Series 1, Springer Science Business Media, LLC. 2011, pp. 21-24.

[81] "Berkovich Tip," retrived July 13th, 2016, http://www.microstartech.com/

[82] "Hardness," retrived July 13th, 2016, https://en.wikipedia.org/wiki/Hardness

[83] X. Li, B. Bhushan, "Mater. Charact.," 48, 11 (2002).

[84] C. P. LIN, "Fabrication and Interfacial Property Analysis of Electroless-Deposited Nanostructures for Imprinting Mold," Ph.D. dissertation, Waseda University, Shinjuku, Japan, July, 2013.

[85] "Elastic Modulus," retrived July 13th, 2016, https://en.wikipedia.org/wiki/Elastic_modulus

[86] L. Xu, John H.L. Pang, "Nano-indentation Characterization of Ni-Cu-Sn IMC Layer Subject to Isothermal Aging," Thin Solid Films, Vol 504, Issues 1-2, pp. 362-366, May 2006.

[87] M. Hasnine,et.al, "Characterization of Aging Effects in Lead Free Solder Joints Using Nanoindentation," IEEE Electronic Compo. & Technol. Conf., Las Vegas, NV, 2013, pp 166-178.

[88] F. Gao, H. Nishikawa and T. Takemoto, "Nano-Scale Mechanical Responses of Sn-Ag Based Lead-free Solders," IEEE Electronic Compo. & Technol. Conf., Reno, NV, 2007, pp. 205-210.

[89] X. Deng, M. Koopman, N. Chawla, K.K. Chawla, "Young's Modulus of (Cu, Ag)-Sn Intermetallics Measured by Nanoindentation," Materials Science and Engineering, A364 (2004), pp. 240-243.

[90] K. M. Kumar, V. Kripesh, Lu Shen, K. Zeng, A.O. Tay, “Nanoindentation Study of Zn-based Pb Free Solders Used in Fine Pitch Interconnect Applications,” Materials Science and Engineering, A 423 (2006), pp. 57-63.

[91] F. Gao, J. Qu, “Elastic Moduli of (Ni, Cu)$_3$Sn$_4$ Ternary Alloys from First-Principles Calculations,” J. of Electronic Materials, Vol. 39, No. 11, 2010, pp 2429-2434.

[92] S. Chang, Y. Lee, H. Hsiao, “Mechanical Properties and Deformation Behavior of Amorphous Nickel-Phosphorous Films Measured by Nanoindentation Test,” Metallurgical and Materials Trans A, Volume 37, Issue 10, pp 2939-2945, Oct. 2006,

[93] X. Lia, B. Bhushana, K.Takashimab, C. Baekc, Y. Kimc, “Mechanical Characterization of Micro/Nanoscale Structures for MEMS/NEMS Applications Using nanoindentation Techniques,” Ultramicroscopy, Volume 97, pp. 481-494, Oct.-Nov. 2003.

[94] A. M. Pillai, A. Rajendra, K. Sharma, “Electrodeposited Nickel-Phosphorous (Ni-P) Alloy Coating: an In-Depth Study of its Preparation, Properties, and Structural Transitions,” J. of Coatings Technology and Research, Volume 9, Issue 6, pp 78-797, Nov. 2012.

[95] T. Jun, D. E. J. Armstrong, T. B. Britton, “A Nanoindentation Investigation of Local Strain Rate Sensitivity in Dual-Phase Ti Alloys,” J. of Alloys and Compounds, Volume 672, pp. 282-291, July 2016.

[96] Ali H. Mohammed, M. I. Hasan, “Nano-Indentation Characterization of deformation of Impact Cylindical Surface of H13 Steel of H13,” Conf. for Engineering and Technological Sciences, Islamic Private University, Iraq, April 2015.

[97] R. Saha, W. D, Nix, “Effects of the Substrate on the Determination of Thin Film Mechanical Properties by Nanoindentation,” Acta Materialia, Volum 50, Issue 1, pp. 23-38, Jan. 2002.

[98] L. Liu, L. Zhou and C. Liu, "Electroless Ni-W-P Alloy as a Barrier Layer Between Zn-based High Temperature Solders and Cu Substrates," Electronic Compon. and Technol. Conf. (ECTC), Orlando, FL, 2014, pp. 1348-1353.